

Anionic redox behaviors of layered oxide based cathode
materials for Na-ion battery systems

September 2020

JIA MIN

Anionic redox behaviors of layered oxide based cathode
materials for Na-ion battery systems

Graduate School of Systems and Information Engineering
University of Tsukuba

September 2020

JIA MIN

ABSTRACT

Rechargeable sodium ion batteries (SIBs) have been considered as the ideal candidates for the next generation energy storage devices in the power supply of electronic products and large-scale energy application systems based on the low cost and rich raw material resources. Therefore, a lot of efforts has been made in searching for electrode materials with excellent electrochemical performance to improve the energy storage ability in SIBs. Layered oxides cathodes have become the most extensively studied topic of current research in view of their high capacities and simple synthesized structure among various electrode materials. However, the inherent defects such as the relatively low energy density greatly limit its practical application. Therefore, how to effectively improve the sodium storage ability and electrochemical performance is the key. Furthermore, the layered oxide cathodes with both cationic and anionic redox attract widespread attention as potential candidates benefit from their beyond-capacity and property of anionic redox mechanism. Herein, we have designed several Na_xTMO_2 layered oxide prototypes with O3, P3 and P2 structures and investigated the corresponding electrochemical performance and anionic redox chemistry. Details are as follows:

Firstly, O3 type $\text{NaMg}_{0.67}\text{Ru}_{0.33}\text{O}_2$ (NMRO) layered oxide is explored as a cathode material for SIBs. The initial charge capacity is nearly 90 mAh g^{-1} , fully attributed to the anionic redox process. To investigate the corresponding anionic redox process, systematical in situ techniques has been employed. Superoxo-related species have been observed from in situ Raman as key intermediates for further understanding the anionic redox mechanism. Additionally, the present O_2 evolution based on DEMS is confirmed the oxidation process of superoxo-related species. More interestingly, anionic redox activity has been sacrificed to obtain a more stable structure for the subsequent cationic

redox process. This discovery may stimulate us to enrich the understanding between the structure and oxygen activation.

Secondly, the anionic redox activity within the P3 type layered cathode $\text{Na}_{0.5}\text{Mg}_{0.15}\text{Al}_{0.2}\text{Mn}_{0.65}\text{O}_2$ (P3-NMAMO) has been confirmed not only by the surface (XPS) but also by the bulk information (XAS). According to the evidence collected from the in situ techniques, the superoxo-related species can only be observed during the first charging and formation of peroxo-related species can be detected reversible. Fortunately, a reversible state has been achieved after the first cycle and even greater stability into the structure is obtained within the cathode.

Thirdly, we develop a P2 type layered cathode $\text{Na}_{0.6}\text{Li}_{0.35}\text{Fe}_{0.1}\text{Ru}_{0.55}\text{O}_2$ (P2-NLFR) with reversible anionic redox behaviors. Conducted with lower charging cut-off voltage (4.0 V), P2-NLFR is easy to trigger the reversible oxygen behaviors and delivers a larger capacity, better rate performance as well as stability. With the unique feature, this work provides a promising strategic design for fabricating cathodes with reversible anionic and cationic redox chemistry, which could further promote the changes in layered structure and even achieve the ideal electrochemical performance.

Through systematically studying the related anionic redox chemistry invested three layered type cathodes, our finding provides specific evidence for anionic redox process in layered oxide cathodes for SIBs. Furthermore, it also highlights the new insight to designing layered oxides with high performance. This research paves a new way for designing the high capacity performance materials with layered structure to develop next generation of sodium ion batteries.

Table of contents

ABSTRACT.....	I
Table of contents.....	III
List of Figures.....	VI
List of Tables.....	XI
Chapter 1. General introduction	1
1.1 Rapid growth in energy demand and feasibility of Sodium ion batteries	1
1.1.1 Rapid growth in energy demand energy storage	1
1.1.2 Feasibility of Sodium ion batteries	2
1.2 Composition and typical working mechanism of Sodium ion batteries	4
1.2.1 Composition of Sodium ion batteries	4
1.2.2 Working mechanism of Sodium ion batteries	5
1.3 Layered oxide cathodes for Sodium ion batteries	6
1.3.1 Advantages of layered oxide cathodes for sodium ion batteries	6
1.3.2 Classification of layered oxides	6
1.3.3 Synthesis of Na_xTMO_2 and related influencing conditions	9
1.4 Anion activation process in layered oxide cathodes	9
1.4.1 Emergence of anionic redox in electrode materials	10
1.4.2 Development of the anionic redox process	10
1.5 Target and outline of this dissertation	12
1.5.1 Motivation of this research	12
1.5.2 Targets of this dissertation	13
1.5.3 Outline of this dissertation	14
Chapter 2. Unraveling the anionic oxygen redox process within O3-type Na layered oxide cathode	16
2.1 Introduction.....	16
2.2 Experiment and characterization.....	17
2.2.1 Preparation of O3 $\text{NaMg}_{0.67}\text{Ru}_{0.33}\text{O}_2$ materials	17
2.2.2 Characterization	17

2.2.3 Electrochemical measurements.....	20
2.3 Results and discussion	20
2.3.1 Morphology and structure characterization.....	20
2.3.2 Electrochemical performance and analysis	21
2.3.3 Oxygen behavior within $\text{NaMg}_{0.67}\text{Ru}_{0.33}\text{O}_2$ cathode.....	23
2.3.4 Phase transition during cycling.....	28
2.3.5 Schematic of the density of states (DOS).....	30
2.4 Summary.....	32
Chapter 3.Elucidating oxygen redox chemistry in P3-layered material for Na-ion batteries.....	33
3.1 Introduction.....	33
3.2 Experiment and characterization.....	34
3.2.1 Preparation of P3 $\text{Na}_{0.5}\text{Mg}_{0.15}\text{Al}_{0.2}\text{Mn}_{0.65}\text{O}_2$ material.....	34
3.2.2 Characterization	35
3.2.3 Electrochemical tests:	36
3.3 Results and discussion	36
3.3.1 Crystal structure of P3 type layered oxide NMAMO.....	36
3.3.2 Electrochemical performance of the P3 type layered oxide cathode NMAMO.....	38
3.3.3 Phase transition in P3 type layered oxide NMAMO during cycling	41
3.3.4 Oxygen related anionic redox chemistry within the P3 type NMAMO	43
3.4 Summary.....	52
Chapter 4. Identifying anionic redox activity within the related P2 type cathode	53
4.1 Introduction.....	53
4.2 Experiment and characterization.....	55
4.2.1 Preparation of P2 $\text{Na}_{0.6}\text{Li}_{0.35}\text{Fe}_{0.1}\text{Ru}_{0.55}\text{O}_2$ (P2-NLFR) material	55
4.2.2 Characterization	55
4.2.3 Electrochemical tests.....	56
4.3 Results and discussion	56

4.3.1 Crystal structure of P2 type layered oxide NLFR.....	56
4.3.2 Morphology of P2 type layered oxide NLFR	57
4.3.3 Electrochemical performance of P2 type layered oxide NLFR	59
4.3.4 Phase transition process within the P2 type layered oxide.....	61
4.3.5 Oxygen related anionic redox chemistry within the P2 type NLFR	63
4.4 Summary	66
Chapter 5. General Conclusion and perspective.....	67
5.1 General conclusion.....	67
5.2 Perspective	68
List of Publications	70
Acknowledgements	71
Reference	73

List of Figures

Figure 1.1 World's energy consumption for each fuel. (Picture is from www.google.com/imghp?hl=zh-cn).	2
Figure 1.2 A unified model for the grid and microgrid, showing the interplay between renewable energy generation. ²⁸ Copyright © 2015 WILEY-VCH Verlag GmbH & Co. KGaA, Weinheim.	3
Figure 1.3 Elemental abundance in the Earth's crust. ²⁹ Copyright © 2014 American Chemical Society.....	4
Figure 1.4 The working principle of room-temperature “rocking chair” sodium-ion batteries. ⁷⁴ Copyright © 2013 ROYAL SOCIETY OF CHEMISTRY.....	6
Figure 1.5 Evolution of publications related to Na layered oxides by years. ⁷⁹ Copyright © 2015 ROYAL SOCIETY OF CHEMISTRY.	7
Figure 1.6 Classification of Na_xTMO_2 layered materials with sheets of edge-sharing MeO_6 octahedral. ²⁹ Copyright © 2014 American Chemical Society.	8
Figure 1.7 Electrochemical performance of $\text{Na}_{2/3}[\text{Mg}_{0.28}\text{Mn}_{0.72}]\text{O}_2$. ⁹⁹ Copyright © 2018, Springer Nature.	12
Figure 2.1 (a) Rietveld refinement XRD pattern of $\text{NaMg}_{0.67}\text{Ru}_{0.33}\text{O}_2$. (b) SEM image of $\text{NaMg}_{0.67}\text{Ru}_{0.33}\text{O}_2$ pristine material.	21
Figure 2.2 (a) Galvanostatic charge/discharge curves collected at a specific current density of 10 mA g^{-1} within the voltage range from 1.5 to 4.0 V vs. Na/Na^+ of $\text{NaMg}_{0.67}\text{Ru}_{0.33}\text{O}_2$. (b) Discharge capacity hysteresis against cycle number of $\text{NaMg}_{0.67}\text{Ru}_{0.33}\text{O}_2$	22
Figure 2.3 Capacity-dependent In-situ Raman spectra recorded during 1st galvanostatic cycle collected on $\text{NaMg}_{0.67}\text{Ru}_{0.33}\text{O}_2$	24
Figure 2.4 In-situ DEMS results of gas evolution rates for O_2 (red circles) and CO_2 (purple circles) collected during 1st and 2nd charging processes on $\text{NaMg}_{0.67}\text{Ru}_{0.33}\text{O}_2$	24
Figure 2.5 Ru 3d and O 1s XPS spectra collected from different cathodes at varying charge/discharge states of $\text{NaMg}_{0.67}\text{Ru}_{0.33}\text{O}_2$ cathode: at pristine, middle of 1st charged	

(at 3.25 V), end of 1st charged (at 4.0 V); 1st discharged and 2nd charged states, respectively.....	27
Figure 2.6 The Ru 3p spectra collected from different compound powder at pristine state., NaMg _{0.67} Ru _{0.33} O ₂ (blue lines), RuO ₂ (red lines), Na ₃ RuO ₄ (black line).....	27
Figure 2.7 (a) GITT voltage profiles (4 h. C/20 pulse, 20 hr. rest) over the 2nd cycle process for NaMg _{0.67} Ru _{0.33} O ₂ materials. (b)Variation of D/R ² vs. potential measured with GITT, showing its correlation with the dQ/dV profiles for NaMg _{0.67} Ru _{0.33} O ₂ cathode.	28
Figure 2.8 Crystal structural analysis via in-situ XRD. Capacity-dependent in-situ XRD results collected over the first two cycles at a current rate of 10 mA g ⁻¹ on NaMg _{0.67} Ru _{0.33} O ₂	29
Figure 2.9 The Rietveld XRD refinement of NaMg _{0.67} Ru _{0.33} O ₂ cathodes after 50 cycles.....	30
Figure 2.10 Schematic of the density of states (DOS) are illustrated in NaMg _{0.67} Ru _{0.33} O ₂	31
Figure 3.1 Rietveld refinement XRD pattern of prepared P3-type NMAMO material.	36
Figure 3.2 Morphology TEM images with the enlarge figure of prepared P3-type NMAMO material.	37
Figure 3.3 Morphology TEM images with the corresponding elemental mapping of Na, O, Mg, Al and Mn of prepared P3-type NMAMO material.	38
Figure 3.4 (a) Charge/discharge curves for the initial two cycle with collected within the voltage range from 2 to 4.5 V vs. Na/Na ⁺ with the current density of 10 mA g ⁻¹ . Cycling performance of the electrode (b) at the different current density and (c) at a high current density of 200 mA g ⁻¹	39
Figure 3.5 The cycling performance of the NMAMO electrode at current density of 10 mA g ⁻¹	39
Figure 3.6 GITT results of P3-NMAMO cathode for the first cycle with the variation of quasi-equilibrium potentials and the calculated Na ⁺ diffusion coefficient.	40

Figure 3.7 The potential profile for a single titration at 3.15 V during charge process with labelling the different parameters (left). The potential profile for a single titration at 3.18 V during discharge process with labelling the different parameters (right). The simplifying equation of Fick's second law to calculate diffusion coefficient (D/R^2), where τ is the limited time period, n is the mole number of the electrode, V_m is the molar volume of the NMAMO, S is the area of electrode, ΔE_s and ΔE_t are the change in the steady state potential and the total change during the current flux by deducting the IR drop, respectively.....	40
Figure 3.8 Capacity-dependent in-situ XRD curves of NMAMO cathode collected during the initial two cycles with the corresponding contour graph.	41
Figure 3.9 The Rietveld XRD refinement of the NMAMO cathode after 100 cycles.	42
Figure 3.10 The Rietveld XRD refinement of the NMAMO pristine powder aging in ambient air for 3 months.	42
Figure 3.11 Mn 2p and O 1s XPS spectra collected from NMAMO cathode at various states with: pristine, 1st charged, 1st discharged and 2nd charged states.	44
Figure 3.12 Mg 1s and Al 2p spectrum collected from NMAMO cathode at various states with: pristine, 1st charged, 1st discharged and 2nd charged states.	45
Figure 3.13 O K-edge XAS spectra for NMAMO cathode using TFY mode at pristine, 1st charged, 1st discharged state respectively.	46
Figure 3.14 Ex situ O K-edge XAS spectra of NMAMO electrode at different states: pristine, 1st charged, 1st discharged state respectively.	47
Figure 3.15 Ex situ Mn L-edge XAS spectra of NMAMO electrode at different states of charge. For L2-edge, the peak position remained constant upon charge and shifted to lower energy in the subsequent discharge, suggesting the preservation of Mn ⁴⁺ upon charge and the reduction of Mn upon discharge.	48
Figure 3.16 The difference spectra of O K-edge XAS results (c) between that of 1st charged state and that of pristine state; between that of 1st discharged state and that of 1st charged state.	48

Figure 3.17 Ex situ O K-edge XAS spectra of NMAMO electrode after fully discharged to 2 V.	49
Figure 3.18 Ex situ O K-edge XAS spectra of NMAMO electrode after fully discharged to 2 V. (a) Capacity-dependent In-situ Raman spectra collected on NMAMO cathode recorded during initial cycle. (b) Raman peak intensities are demonstrated within the corresponding voltage profiles: peroxy-species (green blocks), superoxy-species (red blocks) and carbonate species (yellow blocks)	50
Figure 3.19 In-situ DEMS results of gas evolution rates for O ₂ and CO ₂ collected during the first and second charging process.	50
Figure 3.20 Unified picture of cationic and anionic redox in related P3-NMAMO during the first two galvanostatic cycles.	51
Figure 4.1 Rietveld refinement XRD patterns of P2-NLFR cathode.	56
Figure 4.2 Morphology characterization of prepared P2-NLFR a, b) TEM images, and c) HRTEM images.....	58
Figure 4.3 TEM image of P2-NLFR material with the corresponding elemental maps of Na, Fe, Ru and O.....	58
Figure 4.4 (a) The voltage profiles collected between 1.5 to 4.0 V vs. Na/Na ⁺ at a rate of 10 mA g ⁻¹ of P2-NLFR. (b) Cycling performance of P2 type NLFR as a function of cycle number at 100 mA g ⁻¹	59
Figure 4.5 Cycling performance of P2 type NLFR as a function of cycle number at 20 mA g ⁻¹	60
Figure 4.6 GITT results of P2-NLFR for the first cycle with the variation of quasi-equilibrium potentials and the calculated Na ⁺ diffusion coefficient.	60
Figure 4.7 Rate performance of P2-NLFR electrode with the current density of 10, 20, 30, 50, 100 and 200 mA g ⁻¹ , respectively.	60
Figure 4.8 Crystal structural evolution analysis by in-situ XRD. The collected XRD patterns of P2-NLFR cathodes over the initial two cycles at a rate of C/10.	61
Figure 4.9 The structure evolution of P2-NLFR and related color graph for (002) (004) and (104) reflections during first two cycles.....	62

Figure 4.10 The recorded capacity-dependent operando Raman patterns of P2-NLFR during first two galvanostatic cycles at 0.1 C.	63
Figure 4.11 XPS spectra of Fe 2p, Ru 3d and O 1s for P2-NLFR with the pristine state, the samples charged to 4 V, discharged to 1.5 V and 2nd charged to 4 V from bottom to top.....	64
Figure 4.12 Analysis on oxygen behaviors. In-situ DEMS results of gas evolution rates for CO ₂ and O ₂ on P2-NLFR cathode over the initial cycle at a rate of 0.1 C.....	66
Figure 5.1 Oxygen activation within sodium rich material due to Na-O-Na configuration: (a) Na ₃ RuO ₄ . ¹¹¹ (b) Na ₂ RuO ₃ . ¹⁰⁹ Copyright © 2018 ROYAL SOCIETY OF CHEMISTRY. Copyright © 2016, Springer Nature.	69

List of Tables

Table 1.1 Comparison of Physical Properties for “Lithium” and “Sodium” as Charge Carriers for Rechargeable Batteries. ²⁹ Copyright © 2014 American Chemical Society	3
Table 2.1 Stoichiometry from Inductively coupled plasma spectroscopy with the Na/Mg/Ru ratios for the NaMg _{0.67} Ru _{0.33} O ₂ pristine material.	20
Table 2.2 Refinement results of NaMg _{0.67} Ru _{0.33} O ₂	21
Table 2.3 Refinement results of NaMg _{0.67} Ru _{0.33} O ₂ after 50 cycles.	30
Table 3.1 Refinement crystallographic parameters by Rietveld analysis for NMAMO. S.G. R 3m a = b = 2.86, c = 16.87, $\alpha = \beta = 90^\circ$ $\gamma = 120^\circ$, Rwp = 6.38%, $\chi^2 = 3.145$	37
Table 3.2 Stoichiometry from ICP analysis of the Na _{0.5} Mg _{0.15} Al _{0.2} Mn _{0.65} O ₂ material.	37
Table 3.3 Refinement crystallographic parameters by Rietveld analysis for NMAMO cathode after 100 cycles.	43
Table 3.4 Refinement crystallographic parameters by Rietveld analysis for NMAMO aging for 3 months.....	43
Table 4.1 Refinement results of P2-NLFR sample.	57
Table 4.2 Stoichiometry from ICP analysis of the P2-NLFR pristine material.....	57

Chapter 1. General introduction

1.1 Rapid growth in energy demand and feasibility of Sodium ion batteries

1.1.1 Rapid growth in energy demand energy storage

Energy is the important cornerstone for human activities and the national economy, any human activity needs energy support. With the rapid growth of economy, the dependence of human society on energy is also accelerating.¹⁻⁵ The existing main energy sources can be roughly divided into primary energy sources, secondary energy sources, and other new and renewable energy sources. Among them, primary energy includes coal, natural gas, nuclear energy, solar energy, wind energy and so on. Secondary energy include heat, electricity and refined oil.⁶⁻⁸ At present, most of the world's energy consumption is dominated by fossil fuels. According to statistics, fossil energy accounted for nearly 80% of the energy used by humans, which played a pillar role in the energy structure of human society as shown in **Figure 1.1**.⁹ However, there are many problems in the use of fossil energy, such as the greenhouse effect, acid rain, and uneven energy distribution. The most serious is that the fossil energy is about to be exhausted. Based on current energy consumption calculations, oil and natural gas in fossil fuels will be exhausted after 50 years, and coal resources with the most reserves can only support 132 years¹⁰. So, when the fossil energy consumption is exhausted, what kind of energy can replace its pillar role in the human energy structure?

Therefore, adjusting the current energy structure, looking for advanced methods to improve energy utilization, and developing renewable energy and new energy are the proper meaning and the only way for sustainable energy development.¹¹⁻¹³

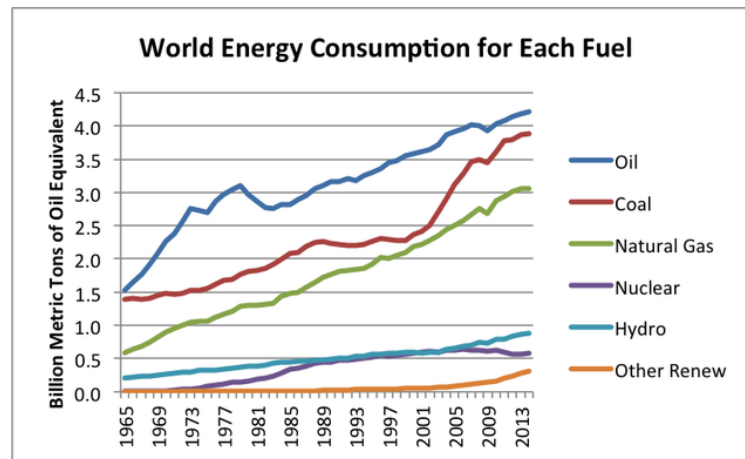


Figure 1.1 World's energy consumption for each fuel. (Picture is from www.google.com/imghp?hl=zh-cn).

Under the guidance of this concept, the development of convenient and efficient energy storage technology to meet the energy needs of human society and economic development has become the focus. Current energy storage technologies can be divided into four types according to specific methods: electromagnetic, phase transition, physical and electrochemical energy storage.¹⁴⁻¹⁵ Among them, electrochemical energy storage has the advantages of low investment, high efficiency, flexible application and safe use. It is the most suitable energy storage method for the current energy development direction, and it is also the most familiar among all energy storage technologies as shown in **Figure 1.2**.¹⁶⁻¹⁹

1.1.2 Feasibility of Sodium ion batteries

As one kind of electrochemical energy storage technology, lithium-ion batteries are considered to be the most promising power supply due to their advantages of large energy density, long cycle life and high operating voltage.^{3, 6, 20-22} They are widely used as the power source for various electronic products.^{4, 23-24} Unfortunately, the lack of lithium resources and the high cost of batteries have greatly hindered the sustainability process of large-scale application for lithium-ion batteries.^{20, 25-27}

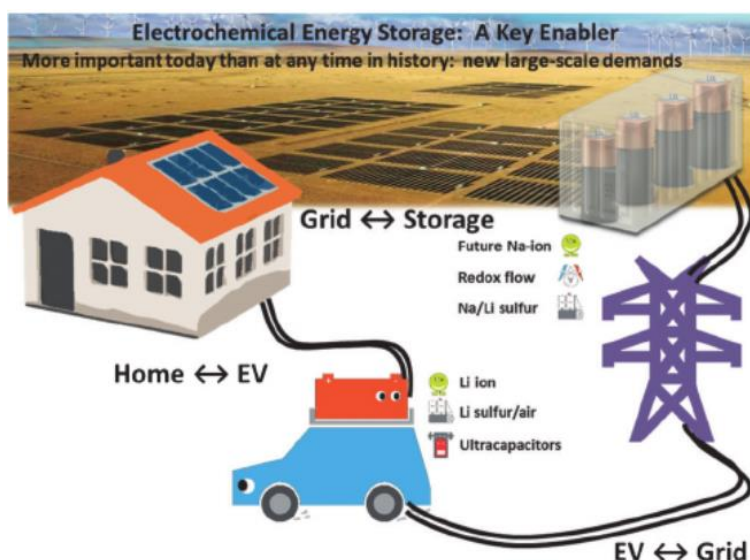


Figure 1.2 A unified model for the grid and microgrid, showing the interplay between renewable energy generation.²⁸ Copyright © 2015 WILEY-VCH Verlag GmbH & Co. KGaA, Weinheim.

Therefore, in recent years, sodium ion batteries have attracted the attention of scientists due to the sodium's similar properties to lithium based on the same main group, as shown in **Table 1.1**.²⁹ Sodium is more active than lithium, and its standard electrode potential is about -2.71 V (Na / Na⁺), which is slightly more positive than lithium (Li / Li⁺). The mass specific capacity is 1166 mAh g⁻¹.³⁰⁻³²

Table 1.1 Comparison of Physical Properties for “Lithium” and “Sodium” as Charge Carriers for Rechargeable Batteries.²⁹ Copyright © 2014 American Chemical Society.

	Li ⁺	Na ⁺
relative atomic mass	6.94	23.00
mass-to-electron ratio	6.94	23.00
Shannon's ionic radii/Å	0.76	1.02
E° (vs SHE)/V	-3.04	-2.71
melting point/°C	180.5	97.7
theoretical capacity of metal electrodes/mAh g ⁻¹	3861	1166
theoretical capacity of metal electrodes/mAh cm ⁻³	2062	1131
theoretical capacity of ACoO ₂ /mAh g ⁻¹	274	235
theoretical capacity of ACoO ₂ /mAh cm ⁻³	1378	1193
molar conductivity in AClO ₄ /PC/S cm ² mol ⁻¹	6.54	7.16
desolvation energy in PC/kJ mol ⁻¹	218.0	157.3
coordination preference	octahedral and tetrahedral	octahedral and prismatic

Compared with lithium resources, sodium resources are abundant, accounting for

about 2.64% of the crust element reserves, which are widely distributed in **Figure 1.3**.³³⁻

³⁵ In addition, in terms of current collectors, for lithium-ion batteries, aluminum is not suitable as a negative electrode current collector because it easily forms the alloy with lithium.³⁶

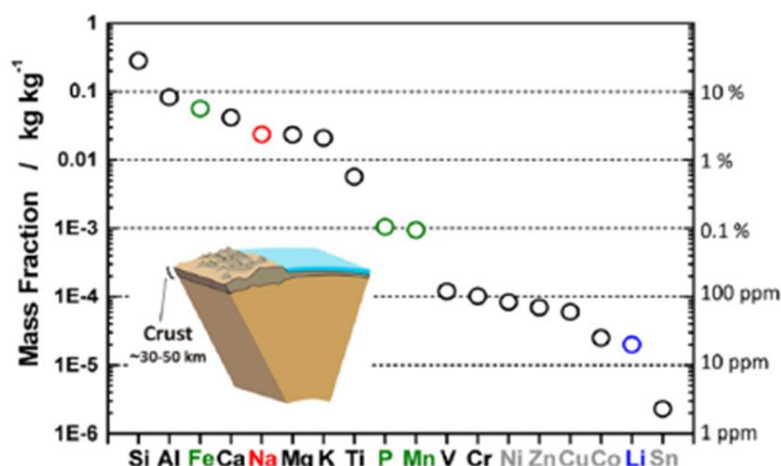


Figure 1.3 Elemental abundance in the Earth's crust.²⁹ Copyright © 2014 American Chemical Society.

Fortunately, in sodium ion batteries, aluminum can not only be used as a positive electrode current collector, but also suitable as a negative electrode current collector. As the price of aluminum is only 1/4 of copper, which greatly reduces the cost for the sodium ion batteries.³⁷ In summary, if sodium ion batteries with excellent electrochemical performance can be developed, they will have better feasibility than the development prospect of lithium ion batteries.^{26, 38-41}

1.2 Composition and typical working mechanism of Sodium ion batteries

1.2.1 Composition of Sodium ion batteries

The sodium ion batteries are also mainly composed of four parts, which is similar to Li-ion batteries: cathode electrode material, anode electrode material, electrolyte and separator. Within the four parts, the cathodes and anodes parts are the core components.

Cathodes electrode materials are generally sodium embedded compounds, such as the layered oxide NaTMO_2 ,⁴²⁻⁴⁶ polyanionic compounds $\text{Na}_3\text{M}_2(\text{PO}_4)_3$ and so on.⁴⁷⁻⁵¹ The types of the anode electrode materials focus on the interlayer compounds with lower potential or carbon based anode,^{26, 38, 52-56} such as $\text{Na}_2\text{Ti}_3\text{O}_7$ ⁵⁶⁻⁵⁹ and hard carbon materials.^{25, 60-63} Separator is necessary to be used separating the cathodes from the anodes and it generally has the electrical insulation to prevent short circuit inside the batteries. Common separators can be made of glass fiber or porous material, such as polyethylene (PE) and polypropylene (PP).⁶⁴⁻⁶⁹ The electrolyte for sodium ion batteries is similar to the electrolyte of the commercial Li-ion batteries, both of which are consist of the sodium salt and electrolyte solvents. Sodium salts include NaClO_4 , NaFP_6 and NaTFSI and propylene carbonate (PC), ethylene carbonate (EC), dimethyl carbonate (DMC) are all the general organic solvents for sodium ion batteries.⁷⁰⁻⁷³

1.2.2 Working mechanism of Sodium ion batteries

In terms of the working mechanism of the sodium ion batteries, it reveals similarities with the Li-ion batteries. For the process of charging and discharging, it is corresponding to extraction and insertion of sodium ions process respectively. Its specific working mechanism and related reaction process is shown in **Figure 1.4**.^{37, 74} In terms of charging, the cathode material undergoes an oxidation reaction, accompanied by sodium ions extracted from its crystal structure and then inserted into the crystal structure of the anode material through the separator. At the same time, electron provided by the external circuit is transferred to the anode electrode through an external circuit to cause a reduction reaction to ensure the charge balance of the entire electrochemical system.

Charge process: $\text{NaTMO}_2 \rightarrow \text{Na}_{1-x}\text{TMO}_2 + x\text{Na}^+ + xe^-$, Oxidation of TM

For the discharge process, sodium ions firstly extract from the crystal structure of the

anode and re-insert into the crystal structure of the cathode through the separator again. At the same time, electron supplied from the external circuit transfer to the cathode to ensure the charge balance of the system.

Discharge process: $\text{Na}_{1-x}\text{TMO}_2 + x\text{Na}^+ + xe^- \rightarrow \text{NaTMO}_2$, Reduction of TM

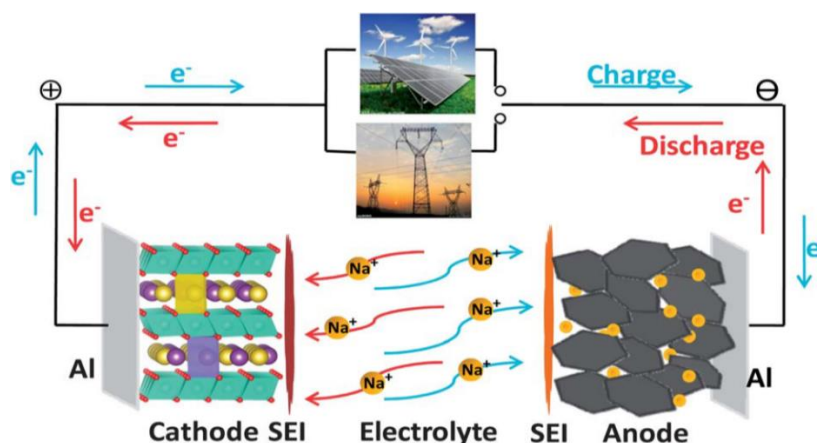


Figure 1.4 The working principle of room-temperature “rocking chair” sodium-ion batteries.⁷⁴

Copyright © 2013 ROYAL SOCIETY OF CHEMISTRY.

1.3 Layered oxide cathodes for Sodium ion batteries

1.3.1 Advantages of layered oxide cathodes for sodium ion batteries

Among various cathodes candidates for sodium ion batteries, layered oxide cathodes attract lot of attention due to many advantages of their own. For example, the advantages of the ease of synthesis, simple structures and high capacities are all reflected within the layered oxide cathodes.⁷⁵⁻⁷⁸ As shown in the **Figure 1.5**, the number of literature studies on the layered oxide in sodium ion batteries published in scientific journals has increased dramatically, reflecting the special interest of the scientific community.⁷⁹

1.3.2 Classification of layered oxides

In general, Na_xTMO_2 is considered as the formula for the sodium containing layered

oxides from the previous reports. The most common layered structure is composed of a sheet of edge sharing TMO_6 octahedral layer with sodium ions located between the oxide layers.

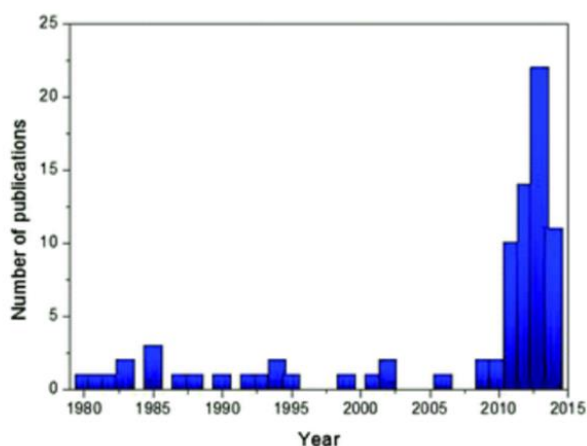


Figure 1.5 Evolution of publications related to Na layered oxides by years.⁷⁹ Copyright © 2015

ROYAL SOCIETY OF CHEMISTRY.

When the TMO_6 octahedral sheets with a common edge are stacked in different orientations along the c-axis direction, then the polymorphisms appear. Typical layered oxide materials for sodium ion batteries can be divided into two categories based on the classification proposed by Delmas and his co-workers: O type or P type. “O” or “P” represents the coordination form of sodium ions between TMO_2 layers and the surrounding six oxygen atoms. “O” means the sodium ions are located at octahedral sites and “P” corresponds to the prismatic sites respectively, as shown in the **Figure 1.6**.²⁹ The symbols of “2” or “3” suggests the numbers of different TMO_2 layers in the repeating cell unit. As for general layered structure O3 type, the sodium ions are accommodated at the O (octahedral) sites. The number “three” represents the numbers of different transition metal layers that are surrounded by different oxide layers: AB, CA, and BC layers. Different layered structures corresponds to the different arrangements of oxygen atoms: oxygen packing of P2 and P3 type is ABBA and

ABBCCA respectively.

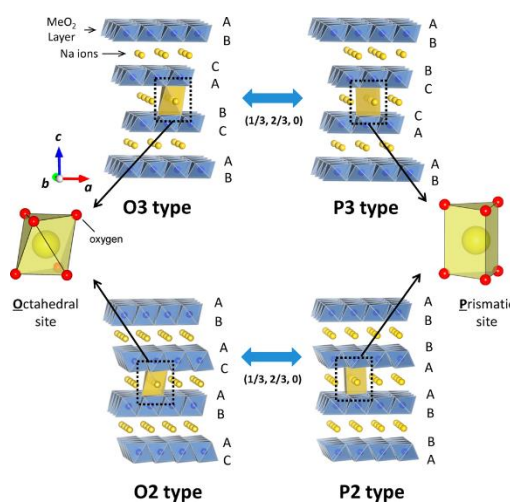


Figure 1.6 Classification of Na_xTMO_2 layered materials with sheets of edge-sharing MeO_6 octahedral.²⁹ Copyright © 2014 American Chemical Society.

For the O3 layered oxide materials, there exists two possible pathways: 1) sodium ions hopping from one octahedral site to the related adjacent octahedral site through O-O bond. 2) sodium ions hopping from the one tetrahedral site to the octahedral site. In this case, the higher activation energy is required to overcome the barriers based on the direct hopping from octahedral site to adjacent octahedral site than the migrating through interstitial tetrahedral sites. Thus, the diffusion pathway of sodium ions is migrating through interstitial tetrahedral sites, which are face-shared sites with octahedral TMO_6 in TMO_2 layers.⁸⁰⁻⁸¹ In the light of the first-principles calculations, the diffusion barrier of sodium ions within the O3-type Na_xCoO_2 material is 180 meV,⁸² which is relatively small.

For the P2 type layered systems, it reveals the open path for sodium ions compared to the O3 type layered material, which probably present a lower diffusion barrier as expected that that of O3 type layered material. The diffusion pathway of sodium ions is migrating one prismatic site to the related adjacent sites through open square bottlenecks surrounded by four oxide ions. It is different from the O3 type layered

material due to it presents no interstitial tetrahedral sites within the P2 type layered material. Actually, the ionic conductivity of P2 type layered material is higher than that of the O3 type layered material based on the similar chemical composition of the both.⁸³ In general, the phase transition process O3-P3 within O3 type layered material and P2-O2 within P2 type layered material could change the mechanism of the sodium ion diffusion for the in-plane direction.⁸³ For example, the activation energy of sodium ion diffusion increases when the P2-O2 phase transition occurs within the P2-type $\text{Na}_x[\text{Ni}_{1/3}\text{Mn}_{2/3}]\text{O}_2$ ($1/3 < x < 2/3$).⁸¹ For the O3 type $\text{Na}_x[\text{Fe}_{0.5}\text{Co}_{0.5}]\text{O}_2$, it presents the excellent rate performance, which can be ascribed to faster ion conduction in the P3 phase formed by the O3-P3 phase transition during the charging process.⁸⁴ Also, it should be noted that the local environment, diffusion pathways and even the mobility of sodium ions in different phases could be different.

1.3.3 Synthesis of Na_xTMO_2 and related influencing conditions

The synthesis of layered oxide materials Na_xTMO_2 based on the different structure has a great relationship with the reaction conditions of the synthesis process. Therefore, it is necessary to strictly control the reaction condition in order to obtain the target phase. Among various conditions, the stoichiometric ration of Na/TM and reaction temperature are the most important factors which need to be considered carefully. For instance, the stable range of the corresponding stoichiometric ration of Na/TM in Na_xCoO_2 is: $0.8 < x < 1$ (O3), $x = 0.75$ (O'3), $0.64 < x < 0.74$ (P2 or P3), $0.5 < x < 0.6$ (P3).⁸⁵ In addition, the reaction temperature is also the control factors which cannot be ignored: P2 type structure is stable at higher temperature and P3 type structure corresponds to the lower temperature. As for the O3 type layered structure, the stable temperature is between the P2 and P3 type structure.

1.4 Anion activation process in layered oxide cathodes

1.4.1 Emergence of anionic redox in electrode materials

For traditional layered oxide cathodes in lithium ion batteries, charge can only be stored on the transition metal (TM) ions. For instance, the charge compensation would be satisfied by the oxidation process from transition metal ion Mn^{3+} to Mn^{4+} of the LiMn_2O_4 layered cathode during the delithiation process.⁸⁶ It is now recognized that the charge compensation process can also be satisfied by the anionic redox chemistry since a series sulfides on ligand-hole chemistry were proposed by Rouxel et al,⁸⁷ for instance, TiS_3 and FeS_2 . These materials indicate that the sulfur ligands is more likely to exist in an oxidized state than S^{2-} due to the relative position of transition-metal(TM) d band and ligand sp bands. Except for the chalcogenides, the extra capacity is also presented in highly covalent TM pnictide cathode electrodes based on the anionic redox activity, such as $(\text{Li}_x\text{MPn}_4, \text{M} = \text{Ti, V, Mn})$ and so on.⁸⁸ Since the less covalent is revealed of oxide than that of sulfides, anionic redox in the oxide related cathode materials was not initially investigated. The oxygen related anionic redox was proposed until the successful preparation of fully delithiated Li_0CoO_2 .⁸⁹ According to the magnetic measurements results, it can be confirmed that transition metal Co has not been fully oxidized to 4+. In addition, the participation of oxygen related anionic redox reaction is further confirmed by the shortening O-O interplanar distance based on the synchrotron diffraction data within Li_xCoO_2 in 1999.⁹⁰

1.4.2 Development of the anionic redox process

Based on all mentioned above, the feasibility of anionic redox activity was proposed and supported by $\text{LiAl}_{1-y}\text{Co}_y\text{O}_2$, which performed the higher potential during the delithiated process and oxygen related oxidation satisfy the charge compensation process rather than TM ions.⁹¹⁻⁹² Moreover, the extracted electrons can only come from the oxygen 2p orbitals because Al^{3+} cannot be further oxidized any more. The related

anionic redox activity was detected within the familiar prototype Li_2MnO_3 a few years later, with which the Mn^{4+} cannot be further oxidized as a precondition.⁹³ The identification of the electrochemical performance mechanism of Li_2MnO_3 is complicated in consideration of the need to reach the higher potential, which could trigger the electrochemical activity more easily, especially for the anionic related redox activity.⁹⁴ In view of the above, it is easier to lead to the electrolyte decomposition under higher potential and some irreversible oxygen release may occur in parallel with this. As for Li_2MnO_3 , it can also be expressed as $\text{Li}[\text{Li}_{1/3}\text{Mn}_{2/3}]\text{O}_2$, which means that in the TM layers one-third of Mn is replaced by Li within an ordered honeycomb-like arrangement.⁹⁵ From then on, reports based on anionic redox triggered by the additional Li ions located in the TM layers have been investigated more frequently. In addition, a series of Li-rich materials have been synthesized and elucidated the corresponding anionic redox activity of them, such as Li_2RuO_3 , Li_2IrO_3 and related partial substitution derived.⁹⁶⁻⁹⁷ Though lots of electrode materials have been employed to explore anionic redox mechanism, there still remains several problems under debate. The way to trigger anionic redox activity, detail contribution of anionic redox process for charge compensation and further structural evolution are all needed to be further clarified. In consideration of the similarity between sodium-ion batteries and Li-ion batteries, the corresponding strategy to trigger anionic redox activity can also be predictable for sodium ion batteries. As shown in the **Figure 1.7**, for the $\text{Na}_{2/3}\text{Mg}_{0.28}\text{Mn}_{0.72}\text{O}_2$ layered cathode, the contribution of charge capacity can be divided into two parts: the charge capacity of first stage is contributed to the transition metal ion oxidation process and the charge capacity of the second stage can be contributed to the oxygen oxidation process.⁹⁸ The phenomenon of oxygen redox is extremely important due to the increased capacity and higher potential provided by storing charge not only on the TM ions but also on the oxide ions.

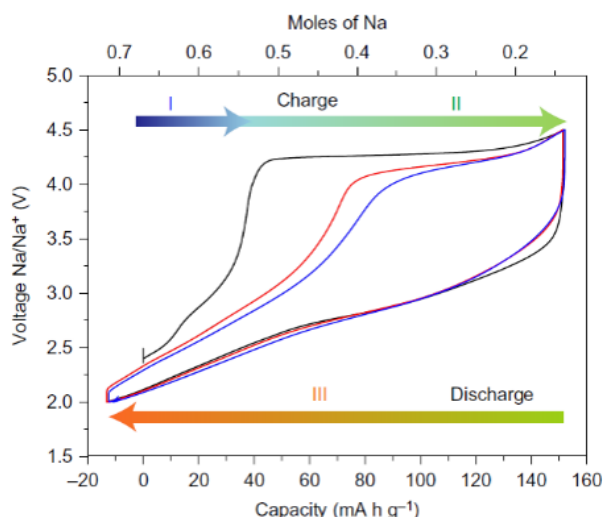


Figure 1.7 Electrochemical performance of $\text{Na}_{2/3}[\text{Mg}_{0.28}\text{Mn}_{0.72}]\text{O}_2$.⁹⁹ Copyright © 2018, Springer

Nature.

The phenomenon of oxygen related anionic redox is extremely important due to the increased capacity and higher potential provided by storing charge not only on the TM ions but also on the oxide ions. Furthermore, it would shed light on materials design to the application of sodium ion batteries and even for large scale energy storage device.

1.5 Target and outline of this dissertation

1.5.1 Motivation of this research

With increasing attention to the energy shortage and environmental issues caused by fossil energy, it is expected that the sustainable and renewable energy could be the major resource of energy. Unfortunately, how to effectively utilize the related sustainable energy resources is strongly depends on the energy storage systems with high efficiency. The rechargeable batteries have attracted a lot of attention among the numerous technology candidates compared to other energy storage technologies, which is attributed to their high efficiency of energy storage, and scale flexibility. Moreover, sodium ion batteries have drawn great attention as a promising rechargeable battery system. On one hand, sodium shares the similar properties with lithium based on the

presentation of same main group and is the second lightest alkali metal next to lithium. On the other hand, sodium resources are abundant in nature. On the basis of standard electrode potential and abundance of sodium resource, the sodium ion batteries have been considered as the promising candidates for energy storage.

As the pivotal part of the sodium ion batteries, tremendous efforts have been made in developments of advanced cathodes materials in sodium ion batteries. In case of the cathode materials, the layered oxide Na_xTMO_2 (TM is transition metal) have attracted intense interest from the researchers in recent years due to their simple structure and easy of synthesis. A further improvement of the specific energy of the layered oxide cathodes is still the central goal for SIBs, which requires the increase of either specific capacity or potential of the electrode material.

In view of the cumulative cationic and anionic redox activity introduced in the lithium-rich compounds, the transformational anionic redox is considered as a new paradigm in designing layered oxide cathodes with high specific energy density for SIBs. Meanwhile, the oxygen related anionic redox activity is easier to be triggered due to the Na-O-Li (Na, Mg) configuration, which could make the oxygen with higher energy more easily be oxidized. Thus, the corresponding anionic redox chemistry of several Na_xTMO_2 layered oxide compounds with O3, P2 and P3 structures is the focus of this dissertation.

1.5.2 Targets of this dissertation

The targets of this dissertation are on the anionic redox chemistry of novel layered oxide cathodes for sodium ion batteries. Details are as follows:

- (1) To investigate the electrochemical performance within O3 type layered oxide cathode and unravel the related anion redox chemistry.
- (2) Elucidating oxygen redox chemistry in a novel P3-layered material for sodium ion

batteries.

- (3) Introducing a newly P2 type layered oxide cathode to systematically clarify the corresponding reversible anionic redox activity process.

1.5.3 Outline of this dissertation

This dissertation consists the following five chapters:

Chapter 1 is the general introduction for this thesis. In this chapter, the urgent demand of high efficiency of energy storage is introduced and the sodium ion batteries have been considered as the promising candidates. Meanwhile, it includes the brief introduction of the layered oxide Na_xTMO_2 , which is regarded as the principal component. And anionic redox activity considered as a new paradigm in designing layered oxide cathodes with high specific energy density for SIBs also is discussed. Moreover, we present the research motivation and targets.

In chapter 2, O3 type layered oxide $\text{NaMg}_{0.67}\text{Ru}_{0.33}\text{O}_2$ has been developed as the novel cathode for sodium ion batteries and related anionic redox activity has been investigated. Systematical in situ techniques has been employed: superoxo-related species have been observed as key intermediates from in situ Raman technology. In addition, it has been proved that the present O_2 release is confirmed by DEMS based on the oxidation process of superoxo-related species. The results reveal the good consistent with our experimental observations.

In chapter 3, P3 type layered oxide $\text{Na}_{0.5}\text{Mg}_{0.15}\text{Al}_{0.2}\text{Mn}_{0.65}\text{O}_2$ has been explored for the newly cathode. The corresponding anionic redox chemistry has been confirmed not only by the surface (XPS) but also by the bulk information (XAS). Formation of peroxo-related species can be detected reversible during the whole electrochemical cycle according to evidence collected from the in-situ data. It is worth noting that a reversible state has been achieved after the first cycle and even greater stability into the

structure is obtained within the cathode.

In chapter 4, a P2 type layered cathode $\text{Na}_{0.6}\text{Li}_{0.35}\text{Fe}_{0.1}\text{Ru}_{0.55}\text{O}_2$ (P2-NLFR) with reversible anionic redox behaviors has been introduced. Of course, the oxygen related anionic redox activity was observed within this cathode as the type of reversible peroxo-related species. P2-NLFR is easy to trigger the reversible oxygen behaviors when the charging cut-off voltage is conducted at 4 V. Moreover, it presents good electrochemical performance not only at rate performance but also for the cycling stability.

Chapter 5 is the conclusion and perspective for the future work in this field.

Chapter 2. Unraveling the anionic oxygen redox process within O3-type Na layered oxide cathode

2.1 Introduction

Up to now, sodium ion batteries have attracted more and more concerns due to the remarkable developments for renewable energy, which are regarded as the promising candidates for energy storage device with high efficiency.^{96, 100-101} In order to achieve the better overall performance of sodium ion batteries, lots of efforts have been made not only for energy density section but also for cycling stability section. Specifically, the cathode materials should be the focus to develop and modify since they are acted as the particularly curial part for the sodium ion batteries.¹⁰²⁻¹⁰³

The layered oxide compounds $A_x\text{TMO}_2$ (TM = transition metal) have been considered as powerful competitors among numerous cathodes candidates.^{102, 104} Because the layered oxides have great potential to obtain higher energy density and the related crystal structure are ease of synthesis. Not limited by the traditional cationic redox activity (TM based redox behavior), the anionic redox activity could also be triggered within the Li/Na rich layered cathodes and additional capacity could be achieved.¹⁰⁵ Similar oxygen related anionic redox activity has been reported for the layered oxide for sodium ion batteries, and the production of peroxo related species can be achieved during the reversible oxygen related anionic redox process.¹⁰⁶ However, the O-O bond length would further be compressed upon the desodiation process at higher charging potential, which will further lead to the irreversible oxygen release process.¹⁰⁷

Anionic redox activity has been arose from the O2p nonbonding orbitals within the layered material proved by the previous reports, which can be achieved by substituting part of transition metal ions with Li or Na.¹⁰⁸⁻¹⁰⁹ In addition, the presentation of O(2p)

non-bonding orbitals depends on Li-O and Na-O bonds are strong ionic ions, thus the electrons are completely localized on the oxygen ions within these bonds.

Herein, the ruthenium based O3 type layered oxide $\text{NaMg}_{0.67}\text{Ru}_{0.33}\text{O}_2$ (Ru^{5+}) was introduced and explored the related anionic redox activity by substituting of TM element with Mg^{2+} . The corresponding oxygen related anionic redox process has been studied by the employment of in-situ spectroscopic characterizations. The superoxo-related species has been originally observed as an important intermediate during the desodiation process. It should be noted that more stable cycle stability can be achieved after the structural rearrangement during the initial charging induced by the oxygen release with the O3 type cathode. It provides a new assessment with the lattice oxygen release with the layered cathode and also presents tentative idea in structural modification for development of Na-ion battery systems.

2.2 Experiment and characterization

2.2.1 Preparation of O3 $\text{NaMg}_{0.67}\text{Ru}_{0.33}\text{O}_2$ materials

$\text{NaMg}_{0.67}\text{Ru}_{0.33}\text{O}_2$ layered oxide material was synthesized by solid state reaction from stoichiometric amounts of Na_2CO_3 , MgO and RuO_2 , and amount of Na_2CO_3 was added with 5 wt% excess. The starting stoichiometric mixture was initially ground together and then held at 600 °C for 10 h under air atmosphere. After re-grinding, the powder was heated to 900 °C for another 15 h, again under air atmosphere. The resulting dark black powder was reground and carefully checked for impurity phases using x-ray diffraction.

2.2.2 Characterization

The structure of $\text{NaMg}_{0.67}\text{Ru}_{0.33}\text{O}_2$ materials was identified by powder XRD (Ultima III, Rigaku Corporation) radiation from Cu $K\alpha$ ($\lambda = 1.5406 \text{ \AA}$). The data were collected

between diffraction angles (2θ) from 10° to 80° at a scan rate of 2° per min. Rietveld refinements of the XRD pattern obtained by GSAS + EXPGUI suite. The morphologies of the materials were procured by SEM (JSM-7000F). In-situ Raman spectra of the materials were obtained using a homemade mould and JASCO microscope spectrometer (NRS-1000DT). In-situ DEMS measurements were carried out using a homemade cell connected to the equipment from Perkin-Elmer (Clarus 680 and SQ 8S). XPS was characterized by a Thermo Fisher Scientific Model K α spectrometer equipped with Al K α radiation (1486.6 eV). The composition of the material was confirmed by inductively coupled plasma (ICP), (M90, Bruker).

In-situ Raman measurements: A detailed description of the modified in-situ Raman cell (Hohsen Corp., Osaka, Japan) for the Na-ion battery was employed. In detail, a thin quartz window (thickness, 0.5 mm) has been fixed on the top of the cell as a sight window. In order to collect shell-isolated nanoparticle-enhanced Raman (SHINER) signal, gold nanoparticles (NPs) approximately 40 nm in diameter with a SiO₂ coating shell (~5 nm) were synthesized. The washed and dried Au@SiO₂ NPs were dripped onto the specific cathode surface and vacuum dried before assembly. The cathode was assembled at the bottom of the cell with the active material-face upward. On the top of the cathode, 50 μ L of electrolyte (1 M NaClO₄ in propylene carbonate (PC)) was homogeneously dropped onto the glassy fiber filter separator (GF/A, Whatman). As a standard two-electrode configuration cell, sodium foil (thickness, 0.4 mm) was assembled at the top as the reference and counter electrode. Note that, a small hole was punched on the center of both the separator and Na metal, through which the laser and Raman signals can fluidly cross. The cell was assembled in an argon-filled glovebox. Besides, bulk-sensitive Raman measurements use the same in-situ Raman cell (Hohsen Corp., Osaka, Japan) with same cell assembling conditions.

The Raman spectra were recorded using a JASCO microscope spectrometer (NRS-

1000DT). The excitation light of an air-cooled He–Ne laser at 632.8 nm wavelength was focused on the electrode surface through a 50×long working distance lens (Olympus America Inc.). The confocal slit was adjusted to be 4.0 μm to minimize the band broadening effect due to the contribution of non-confocal signal. The scattered light was collected in a backscattering geometry along the same optical path as the pumping laser. The power of laser beam delivered to the electrode surface was roughly 10% of the maximum 30 mW laser intensity, unless specified, to avoid degradation to the products and/or cathode in SHINER while the estimated power on the sample was 0.43 mW in bulk-sensitive Raman. The Raman spectrum acquisition time varied from 600~800 s with 2 accumulations. At least 3 different places on the electrode surface at each cathode plate were checked to ensure the Raman spectra were credible and reproducible. The spectral resolution of the Raman spectra in the study was ca. 1.0 cm^{-1} . For the in-situ Raman test, the electrochemical experiments were carried out under the control of a potentiostat (Potentiostat/Galvanostat PGSTAT30, Autolab Co. Ltd., Netherlands) at room temperature. The current and potential outputs from the potentiostat were recorded by a multifunction data acquisition module/amplifier (PGSTAT30 Differential Electrometer, Autolab), which was controlled by General Purpose Electrochemical Software (GPES). Typically, the galvanostatic control was carried out at a current density of 20 mA g^{-1} . Before characterization, the cell was kept on an open circuit for 10 h. The OCV was approximately 2.8 V in most cases in the study. All the potentials in this study were referenced to Na/Na^+ .

In-situ Differential Electrochemical Mass Spectrometry (DEMS) measurements: In situ Differential Electrochemical Mass Spectrometry (DEMS) measurements were carried out using a homemade cell connected to the equipment from Perkin-Elmer (Clarus 680 and SQ 8S). The mass spectrometer absolute sensitivity is calibrated for CO_2 and O_2 , therefore, the evolution rate of these gases can be obtained.

2.2.3 Electrochemical measurements

2032 coin-type cells were used for electrochemical measurements. The electrodes consisted of active material, acetylene black, and polytetrafluoroethene (PTFE, 12 wt.%) binder with the weight ratio of 80:10:10. 1 M NaClO₄ in propylene carbonate (PC) was prepared as the electrolyte. Battery tester system HJ1001 SD8 (Hokuto Denko) were employed for galvanostatic testing.

2.3 Results and discussion

2.3.1 Morphology and structure characterization

The O3-type NaMg_{0.67}Ru_{0.33}O₂ material was synthesized using conventional solid-state method and the obtained material is confirmed by the inductively coupled plasma spectroscopy with the Na/Mg/Ru ratios. The related ICP data is shown in the **Table 2.1** and it fits well with the corresponding targeted compositions. The major Bragg reflections of the X-ray diffraction pattern for obtained NaMg_{0.67}Ru_{0.33}O₂ material is presented in the **Figure 2.1a**, which can be well ascribed to the O3-type layered structure belongs to the R $\bar{3}$ m space group. Within the NaMg_{0.67}Ru_{0.33}O₂ cathode, the transition layer consists of Mg²⁺ and Ru⁵⁺. As shown in the figure, the stacking sequence of oxygen ions is following the ABCABC sequence. Based on the Rietveld refinement results of XRD (**Table 2.2**), the reasonable χ^2 value is 5.287 according to the GSAS + EXPGUI suite.

Table 2. 1 Stoichiometry from Inductively coupled plasma spectroscopy with the Na/Mg/Ru ratios for the NaMg_{0.67}Ru_{0.33}O₂ pristine material.

		<i>Na</i>	<i>Mg</i>	<i>Ru</i>
NaMg _{0.67} Ru _{0.33} O ₂	Conc.	13.2943	9.6582	19.0645
	Stoichiometric	0.578	0.397	0.189

Table 2. 2 Refinement results of $\text{NaMg}_{0.67}\text{Ru}_{0.33}\text{O}_2$.

Refinement results of NMRO		
Phase	$\text{NaMg}_{0.67}\text{Ru}_{0.33}\text{O}_2$	
	$R-3m$	
Space group	a (Å)	3.04316(5)
	b (Å)	A
	c (Å)	16.1166(4)
Cell parameters	α (°)	90
	β (°)	90
	γ (°)	120
	Cell volume (Å ³)	129.256(4)
Agreement factors	Rwp(%)	9.72
	Rp(%)	6.47
	χ^2	5.287

Moreover, the refinement result is based on the O3 type layered structure NaRuO_2 model. The corresponding refinement results suggest that the dominant phase within the obtained material is O3 type layered phase. Several small peaks are also observed in the figure, which can be attributed to the MgO impurity. In consideration of the inactive electrochemical activity of MgO, the contribution of MgO during charge compensation process can be negligible. In addition, SEM image of the $\text{NaMg}_{0.67}\text{Ru}_{0.33}\text{O}_2$ is shown in the **Figure 2.1b** with the micro-sized particles.

2.3.2 Electrochemical performance and analysis

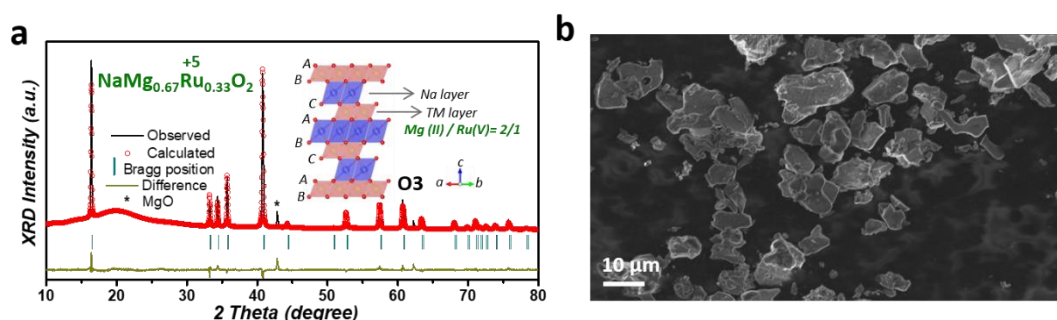


Figure 2. 1 (a) Rietveld refinement XRD pattern of $\text{NaMg}_{0.67}\text{Ru}_{0.33}\text{O}_2$. (b) SEM image of $\text{NaMg}_{0.67}\text{Ru}_{0.33}\text{O}_2$ pristine material.

The electrochemical performance of as-prepared $\text{NaMg}_{0.67}\text{Ru}_{0.33}\text{O}_2$ cathode were shown in **Figure 2.2a** within the potential window (vs Na/Na^+) of 1.5-4 V under the current density of 10 mA g^{-1} . During the initial charge process, a specific charge capacity of 87 mAh g^{-1} is delivered, which is correspond to amount 0.38 Na^+ for deintercalation.

For $\text{NaMg}_{0.67}\text{Ru}_{0.33}\text{O}_2$ cathode, the valence of Ru is +5 for its pristine state, which means that a higher valence state within Ru cannot be obtain as expected for the layered material. Thus, there is no potential for Ru-related cationic redox activity to satisfy the charge compensation during the sodium de-intercalation process and only the oxygen related anionic redox can be considered as the achievement of the charge compensation process.¹¹⁰ Therefore, the O3 type layered oxide $\text{NaMg}_{0.67}\text{Ru}_{0.33}\text{O}_2$ cathode is introduced as a prototype to further investigate the corresponding anionic redox process. Upon the subsequent discharge process during initial cycle, the discharge capacity of 81 mAh g^{-1} can be reversibly obtained. **Figure 2.2b** presents the cycling performance within this O3 type layered cathode. The capacity retention is 88% at the current density of 10 mAh g^{-1} after 50 cycles.

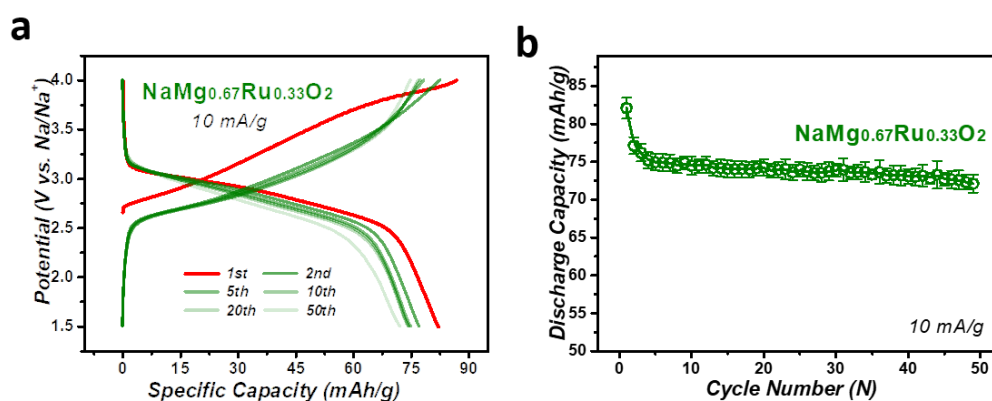


Figure 2. 2 (a) Galvanostatic charge/discharge curves collected at a specific current density of 10 mA g^{-1} within the voltage range from 1.5 to 4.0 V vs. Na/Na^+ of $\text{NaMg}_{0.67}\text{Ru}_{0.33}\text{O}_2$. (b) Discharge capacity hysteresis against cycle number of $\text{NaMg}_{0.67}\text{Ru}_{0.33}\text{O}_2$.

2.3.3 Oxygen behavior within $\text{NaMg}_{0.67}\text{Ru}_{0.33}\text{O}_2$ cathode

Firstly, in-situ Raman spectroscopy is employed to investigate the oxygen related anionic redox chemistry within the O3 type layered cathode $\text{NaMg}_{0.67}\text{Ru}_{0.33}\text{O}_2$ in **Figure 2.3**. Moreover, the in-situ Raman technology has been widely used as powerful measurement to trace the signals of both peroxo-related and superoxo-related species including SERS and SHINERS. For $\text{NaMg}_{0.67}\text{Ru}_{0.33}\text{O}_2$ cathode, upon the initial charging, several novel Raman peaks can be observed, which is corresponding to various oxygen redox behaviors. During the initial stage of charging, a distinct peak can be clearly observed around 825 cm^{-1} , which can be rationally attributed to the peroxo-related stretching mode.¹¹¹ The formation of peroxo-related species suggests that the oxygen state has been activated from O^{2-} to O^- . In addition, the peroxo-related peak disappeared at medium stage of the first charge process, which is different from the typical reversible peroxo-related anionic redox reaction process. Because the peroxo-related peak is formed during the charging process and decomposed during the subsequent discharging process within the reversible peroxo-related anionic redox reaction. It is worth noting that the specific peak shifts to the higher wavenumber upon the sodium ion deintercalation process which indicates that the O-O bond length becomes shorter upon the charging.

Another newly-formed peak can be observed at 1103 cm^{-1} after charging to 3.4V and it is rationally ascribed to the superoxo-related species. The corresponding superoxo-related stretching mode gradually increased along with the further oxidation process from O^- to O_2^- . Also, when the superoxo-related species increased, the related peroxo-related species presented the reducing tendency. Moreover, a series of novel peaks located at 982 cm^{-1} and 1013 cm^{-1} accompanied with the production of superoxo-related species.

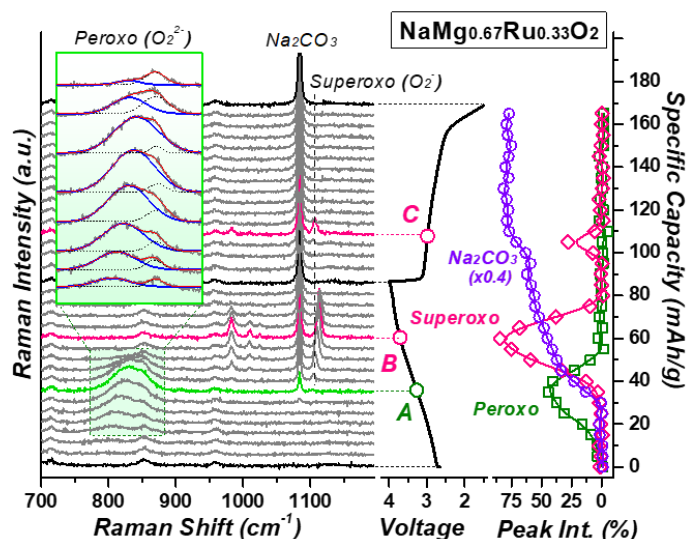


Figure 2. 3 Capacity-dependent In-situ Raman spectra recorded during 1st galvanostatic cycle collected on $\text{NaMg}_{0.67}\text{Ru}_{0.33}\text{O}_2$.

These novel peaks can be attributed to the parasitic products derived from the degradation process within which the propylene carbonate (PC) solvent attack from the superoxide radical (O_2^-) by nucleophilic reaction process.¹¹²

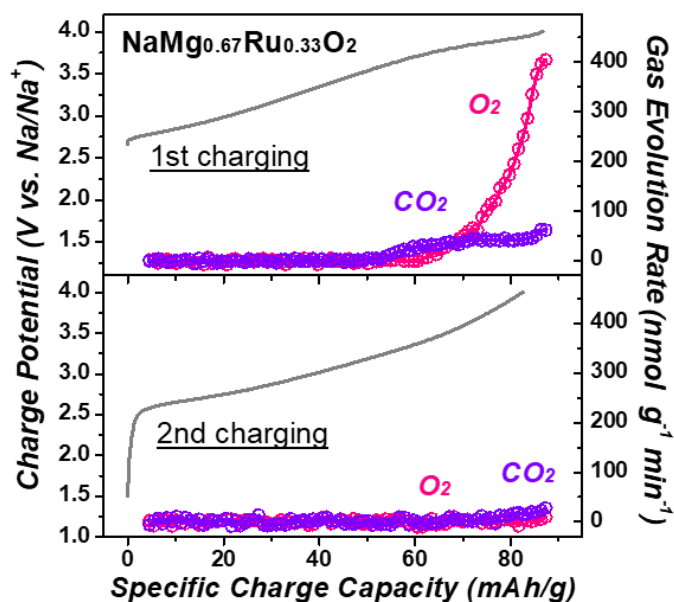


Figure 2. 4 In-situ DEMS results of gas evolution rates for O_2 (red circles) and CO_2 (purple circles) collected during 1st and 2nd charging processes on $\text{NaMg}_{0.67}\text{Ru}_{0.33}\text{O}_2$.

Then, the superoxo-related O-O stretching mode began to decrease around 3.6 V and further disappeared at 3.8 V, which suggests that the superoxo-related species underwent the further oxidation process. DEMS technique also is employed to directly collect the gas evolution information and further to elucidate the related oxygen behavior mechanism during the anionic redox reaction in **Figure 2.4**. The DEMS results present well consistent with the Raman data. The oxygen evolution rate performs the rapid growth upon the latter stage of initial charging process at around 3.7 V.

In addition, the released oxygen would be reduced during the subsequent discharging for the first cycle due to the sealed cell architecture. In another word, the released O₂ during the first charging is trapped inside the coin cell and further reduced by the oxygen reduction reaction.¹¹³ The re-observation of the superoxo-related Raman signal at about 2.8 V also can further confirm the oxygen reduction reaction process during the initial discharging. However, neither peroxo-related species nor oxygen can be detected during the second charge process, which is indicating that on more oxygen related anionic redox activity is performed upon the subsequent cycles.

As for NaMg_{0.67}Ru_{0.33}O₂ cathode, the oxygen related anionic redox can be activated in the initial cycle. Unfortunately, the oxygen related redox activity cannot be stored within this cathode due to serious oxygen release and disappearance of peroxo-related species upon the latter stage of initial charge process. Thus, during the subsequent galvanostatic charge and discharge process, oxygen becomes totally deactivated and cation based redox reaction would participates.

In addition, the proposed charge compensation mechanism during the charge discharge process is further proved by the XPS data in the **Figure 2.5** below. XPS is employed to clarify the valence state variation of Ru and O during the sodium de-intercalation process, which is essentially necessary for the whole charge compensation process (cationic and anionic redox process). The Ru 3d spectra obtained within the

NaMg_{0.67}Ru_{0.33}O₂ cathode at the pristine state presents a major peak located at around 282.9 eV, which indicates the sole existence of Ru⁵⁺. Furthermore, we use pure original Ru⁴⁺ model, RuO₂ and pure original Ru⁵⁺ prototype model, Na₃RuO₄ as the corresponding reference in the **Figure 2.6**.

Actually, the binding energy of Ru 3d_{5/2} for Na₃RuO₄ collects at pristine state reveals the core peak at 283.04 eV, and it presents 282.89 eV for NaMg_{0.67}Ru_{0.33}O₂. There is almost no difference between the both and it confirms that the valence of Ru within the NaMg_{0.67}Ru_{0.33}O₂ material is +5.

After charged to 3.25 V, the major peak position shifts positively to 282.6 eV and it is different from the typical position of Ru⁴⁺ at 282.2 eV. And the neighbor chemical environment and the strong electronic redistribution along the Ru-O bonds has been changed due to the variation of the electronic states after the stimulation of anionic redox process.¹⁰⁹

It is worth noting that the valence of Ru turns back to +5 after oxygen release at the end of charge process at 4 V, which suggests that Ru based cationic redox makes no contribution to the charge compensation process during the initial charging. The corresponding O 1s spectra is simultaneously shown in the **Figure 2.5**. Production of additional peroxo-related peak is observed at 530.7 eV, indicating the appearance of oxygen related anionic redox activity.

Upon the initial discharge process, Ru-based cationic redox participates the charge compensation process with the negative shift of the Ru 3d peak to 282.4 eV. In addition, during the second charge process, Ru related cationic redox dominates the charge compensation process while oxygen related anionic redox has not been activated. Within NaMg_{0.67}Ru_{0.33}O₂ cathode, the charge compensation mechanism of first charging process is totally different from the second charging based on the Raman and XPS results. Also, the valence state shown by the XPS reveals the good consistent with

the interpretation of oxygen activity presented by in-situ Raman and DEMS.

Furthermore, the evaluated GITT profiles and corresponding D/R^2 calculation are revealed to investigate the kinetic process and reversibility with the $\text{NaMg}_{0.67}\text{Ru}_{0.33}\text{O}_2$ cathode in **Figure 2.7**.

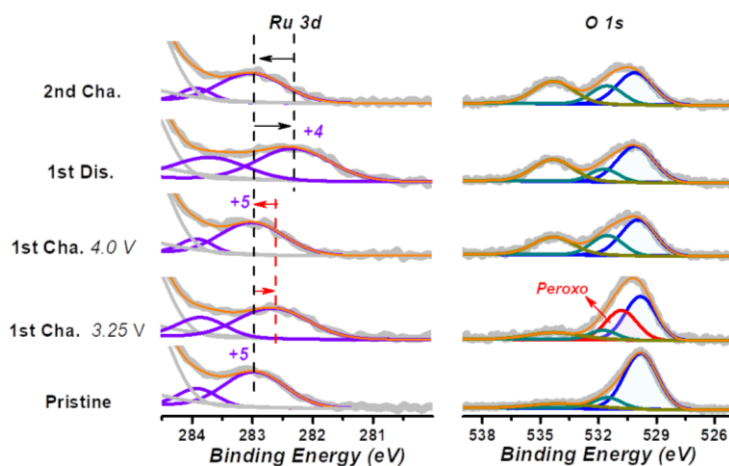


Figure 2. 5 Ru 3d and O 1s XPS spectra collected from different cathodes at varying charge/discharge states of $\text{NaMg}_{0.67}\text{Ru}_{0.33}\text{O}_2$ cathode: at pristine, middle of 1st charged (at 3.25 V), end of 1st charged (at 4.0 V); 1st discharged and 2nd charged states, respectively.

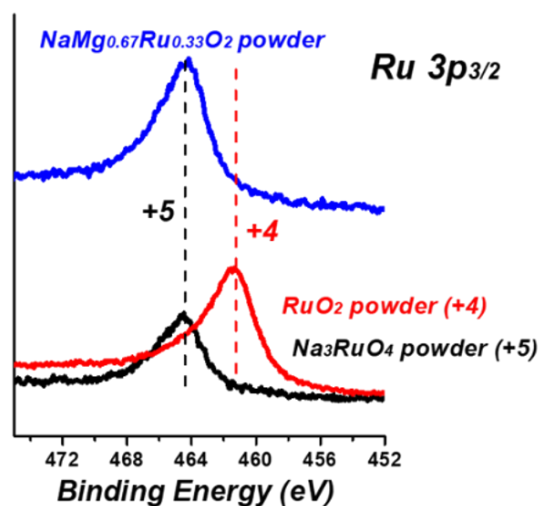


Figure 2. 6 The Ru 3p spectra collected from different compound powder at pristine state., $\text{NaMg}_{0.67}\text{Ru}_{0.33}\text{O}_2$ (blue lines), RuO_2 (red lines), Na_3RuO_4 (black line).

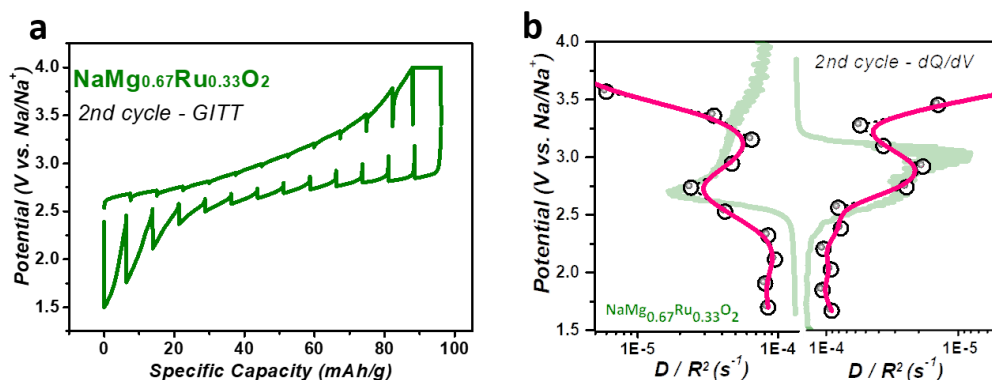


Figure 2. 7 (a) GITT voltage profiles (4 h. C/20 pulse, 20 hr. rest) over the 2nd cycle process for NaMg_{0.67}Ru_{0.33}O₂ materials. (b) Variation of D/R^2 vs. potential measured with GITT, showing its correlation with the dQ/dV profiles for NaMg_{0.67}Ru_{0.33}O₂ cathode.

It shows only one pair of minima corresponding to the peak of dQ/dV profiles. And it is suggesting that the redox reaction performs a moderate dynamics process based on the less energy barrier change within NaMg_{0.67}Ru_{0.33}O₂.¹¹⁴

2.3.4 Phase transition during cycling

Crystal structural evolution of NaMg_{0.67}Ru_{0.33}O₂ cathode is analyzed by the in-situ XRD for the initial two galvanostatic charge discharge process in **Figure 2.8**. During the first sodium de-intercalation process, the O3 phase is well maintained. Along with the desodiation process, the O3 phase gradually transforms to the O3+P3 two phases accompanied by the activation of anionic redox reaction. The crystal structure gradually turns back to the O3 phase along with the oxygen release process. And at the end of the first charging another O'3 phase appears. Then, at the end of the subsequent discharge process, the structure restores back to O3 single phase. It is worth noting that during the second galvanostatic charge discharge process, it reveals the simple phase transition process reversible between O3 and O3+O'3 within the NaMg_{0.67}Ru_{0.33}O₂ cathode. In addition, the specific distorted structure has been formed upon the first sodium

deintercalation process accompanying with the oxygen release.

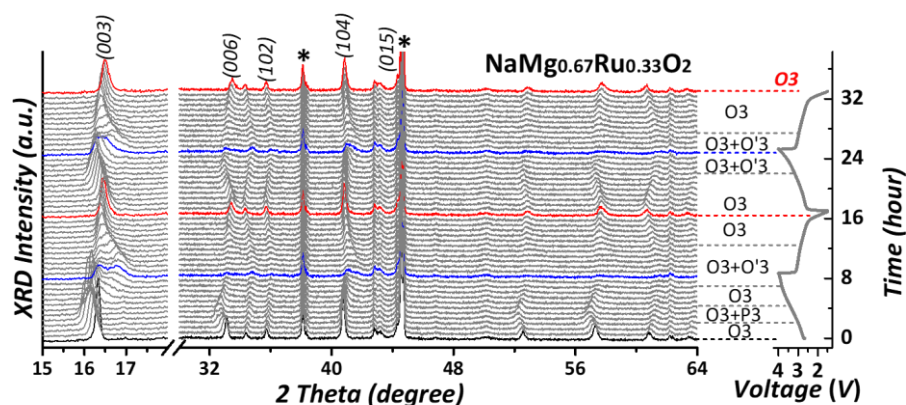


Figure 2. 8 Crystal structural analysis via in-situ XRD. Capacity-dependent in-situ XRD results collected over the first two cycles at a current rate of 10 mA g^{-1} on $\text{NaMg}_{0.67}\text{Ru}_{0.33}\text{O}_2$.

After the first cycle, the phase transition process performs the reversible and symmetric feature during the subsequent cycles with single O3 phase presented at the discharged state. More importantly, the simple phase transition process during the second cycle between the O3 and O'3 phase, which suggests the moderate dynamic process corresponding to the GITT results. It is obvious that subsequent transition process is simple and reversible after structural rearrangement of initial cycle within the $\text{NaMg}_{0.67}\text{Ru}_{0.33}\text{O}_2$.

Furthermore, related ex-situ XRD pattern of $\text{NaMg}_{0.67}\text{Ru}_{0.33}\text{O}_2$ is collected after 50 cycles in order to further investigate the relationship between the cycling stability and structural evolution during the long-term cycling. The Rietveld refinement curve of the $\text{NaMg}_{0.67}\text{Ru}_{0.33}\text{O}_2$ is shown in the **Figure 2.9**. The XRD pattern after 50 cycles reveals good consistent with the pristine pure O3 type layered structure and no splitting peak can be observed. It indicates that it performs the relative structural stability for cycling within this O3 layered oxide material. The corresponding parameters of XRD refinement results also are revealed in the **Table 2.3** and the O3 layered structure after 50 cycles is further confirmed within the $\text{NaMg}_{0.67}\text{Ru}_{0.33}\text{O}_2$.

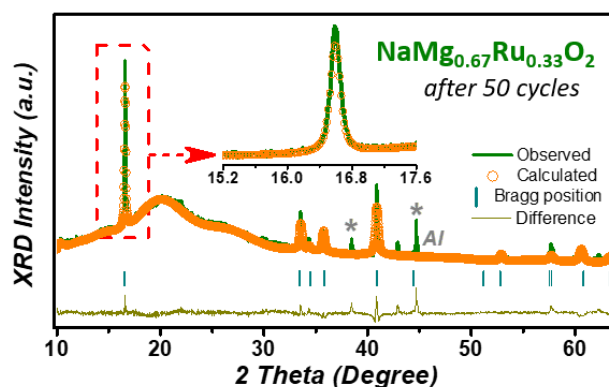


Figure 2. 9 The Rietveld XRD refinement of $\text{NaMg}_{0.67}\text{Ru}_{0.33}\text{O}_2$ cathodes after 50 cycles.

2.3.5 Schematic of the density of states (DOS)

The specific redox process within the O3 type layered oxide material is schematically described the density of states illustrations in **Figure 2.10**. At the pristine state $\text{Ru}^{5+}(\text{t}2\text{g})$ band being half filled merges on the top portion of the $\text{O}(2\text{p})$ -band within the $\text{NaMg}_{0.67}\text{Ru}_{0.33}\text{O}_2$ cathode. Ru still presents +5 state with the reduction of EF accompanied by the activation process of oxygen related anionic redox reaction process due to the virtual Ru^{6+} cannot stably exist within the octahedral coordinate structure.

Table 2.3 Refinement results of $\text{NaMg}_{0.67}\text{Ru}_{0.33}\text{O}_2$ after 50 cycles.

Refinement results of NMRO after 50 cycles		
Phase	$\text{NaMg}_{0.67}\text{Ru}_{0.33}\text{O}_2$ after 50 cycles	
Space group	$R\text{-}\bar{3}m$	
	a (Å)	3.059(4)
	b (Å)	A
	c (Å)	16.048(22)
Cell parameters	α (°)	90
	β (°)	90
	γ (°)	120
	Cell volume (Å ³)	130.05(31)
Agreement factors	Rwp(%)	19.51
	Rp(%)	10.83
	χ^2	16.86

Unfortunately, since the lattice oxygen within the O3 type layered oxide material has been oxidized into superoxo-related species and even oxygen, no reversible oxygen related anionic redox activity can be utilized during the subsequent sodium intercalation process. Electrons fill into Ru-based orbital during initial discharge process and reduction process is occurred from Ru^{5+} to Ru^{4+} . It is noteworthy that the oxygen release is considered as the negative effect as described within the Li-rich NCM cathode for lithium ion batteries due to the chemomechanical break within the layered cathode material resulted from the oxygen loss.¹¹⁵ And the above mentioned violates the original intention of taking advantage of oxygen related anionic redox activity.

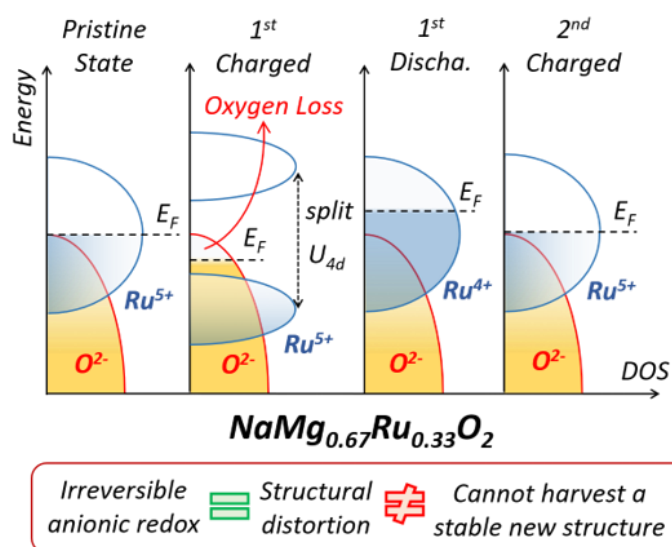


Figure 2. 10 Schematic of the density of states (DOS) are illustrated in $\text{NaMg}_{0.67}\text{Ru}_{0.33}\text{O}_2$.

However, it is unfair to conclude the structural distortion (induced by lattice oxygen loss) as negative structural deterioration within entire layered oxide cathodes family. Herein, stable crystal structure and more reversible phase transition process can be obtained during the subsequent cation redox-related electrochemical cycles within the O3 type layered oxide material by sacrificing the additional oxygen related anionic redox reaction. In other words, irreversible lattice oxygen loss does not necessarily correspond to negative structural breakdown, while the distortion may induce a positive

structural transformation, which is beneficial for structural stability during subsequent cycling.

2.4 Summary

In general, the lattice oxygen release within the anionic redox process should be restrained because the extra capacity provided by oxygen related anionic redox reaction cannot be utilized. It is also believed that related structural transformation will negatively affect the structural stability in subsequent cycles, which will lead to structural degradation. In this work, oxygen related anionic redox is investigated within the O3 type layered oxide $\text{NaMg}_{0.67}\text{Ru}_{0.33}\text{O}_2$ and oxygen release is confirmed by in-situ DEMS technique. More interestingly, the initial oxygen release during the initial charging induces a relatively positive structural transformation process. Specifically, after the first sodium deintercalation process, the simple and reversible phase transition process between O3 and O'3 within the O3 type layered oxide cathode would facilitate cycle stability during long-term cycling. In other words, oxygen related anionic redox activity during the first cycle has been sacrificed to obtain a more stable structure for the subsequent cationic redox based charging and discharging process. This discovery may stimulate us to reconsider the relative stable structure caused by the loss of lattice oxygen. Next, as an effective method to increase energy density, the reversible anion redox process related to peroxo-related species should be stabilized. At the same time, as a structural modification strategy, appropriate oxygen loss can be introduced into a specific layered oxidation cathode to optimize phase transition and structural stability.

Chapter 3. Elucidating oxygen redox chemistry in P3-layered material for Na-ion batteries

3.1 Introduction

Rechargeable Li-ion batteries (LIBs) have become more powerful and promising candidates for today's sustainable energy storage systems due to their increasingly energy storage capabilities.¹¹⁶⁻¹¹⁸ Unfortunately, there are still several serious shortages that are needed to be considered for further practical application in LIBs within large scale electric device section, such as the high production cost and uneven geographic distribution. Up to date, sodium ion batteries have been regarded as the promising candidates for electrochemical energy storage ascribed to the wide distribution and abundant resources of sodium.¹¹⁹ The further increase in the specific energy density of the electrode material is the central goal for SIBs, which requires an increase either in potential or the capacity of the electrode material. Taking into account the cumulative cationic and anionic redox activity introduced within the Li-rich compounds, the transformational anionic redox activity is considered to be a new paradigm for designing electrode material with high specific energy density for SIBs.¹²⁰⁻¹²²

As with every discovery, The fundamental source of anionic redox was investigated through extensive research activities within SIBs.¹²³ In addition, great efforts have been made and many papers have been reported up to now. Generally, the anionic redox activity would be arose from two categories in layered oxide cathodes: one approach is to replace part of the TM in the NaTMO₂ (TM: transition metal) compounds by Li, Na, Mg or even Zn, to achieve the occurrence of O (2p) nonbonding orbitals.¹²⁴⁻¹²⁷ The other approach is to introduce the TM vacancies, to generate the nonbonding O(2p) orbitals along with the Na-O-□ or □-O-□ axes.

Although the origin of the anionic redox activity may be arose from oxygen lone-

pair states, the practical applications of such anionic redox still faces huge technical challenges due to the release of the O₂ and resulting performance decay.¹²⁸⁻¹²⁹ Therefore, these considerations prompted a further investigation of the possible mechanism of the entire anionic redox process especially for the irreversible oxygen release process.¹³⁰

In this study, we obtained the direct evidence of anionic redox process, especially for the involvement of lattice oxygen redox in the process of O₂ release. The typical layered material P3-type Na_{0.5}Mg_{0.15}Al_{0.2}Mn_{0.65}O₂ (NMAMO) is introduced as a prototype. Highly reversible structural evolution and excellent stability upon cycling has been observed by the operando XRD. In addition, we have clarified the mechanism of oxygen redox chemistry during the reaction through the combined use of the surface-sensitive spectroscopy (XPS and Raman) and bulk-sensitive spectroscopy (XAS and DEMS). In particular, the origin of irreversible O₂ evolution during the first charge can be reasonably attributed to the activity of unstable superoxo-related species. Further, the continuous redox activity of O₂ in the sealed cell will lead to the accumulation of carbonate species during the subsequent discharge process. These findings are generally applicable to the design of materials with capability for high storage of specific energy where the participation of anions participation plays a crucial role.

3.2 Experiment and characterization

3.2.1 Preparation of P3 Na_{0.5}Mg_{0.15}Al_{0.2}Mn_{0.65}O₂ material

Na_{0.5}Mg_{0.15}Al_{0.2}Mn_{0.65}O₂ sample was synthesized by solid state reaction from stoichiometric amounts of Na₂CO₃, MgO, Al₂O₃ and MnO₂, and amount of Na₂CO₃ was added with 5 wt% excess. The starting stoichiometric mixture was ground together and then held at 700 °C for 24 h under air atmosphere. The resulting black powder was reground and carefully checked for impurity phases using x-ray diffraction.

3.2.2 Characterization

The structure of $\text{Na}_{0.5}\text{Mg}_{0.15}\text{Al}_{0.2}\text{Mn}_{0.65}\text{O}_2$ material was identified by powder XRD (Ultima III, Rigaku Corporation) radiation from Cu $K\alpha$ ($\lambda = 1.5406 \text{ \AA}$). The data were collected between diffraction angles (2θ) from 10° to 80° at a scan rate of 2° per min. Rietveld refinements of the XRD pattern obtained by GSAS + EXPGUI suite. In-situ Raman spectra of the materials were obtained using a homemade mould and JASCO microscope spectrometer (NRS-1000DT). In-situ DEMS measurements were carried out using a homemade cell connected to the equipment from Perkin-Elmer (Clarus 680 and SQ 8S). XPS was characterized by a Thermo Fisher Scientific Model $K\alpha$ spectrometer equipped with Al $K\alpha$ radiation (1486.6 eV). The composition of the material was confirmed by inductively coupled plasma (ICP), (M90, Bruker), HRTEM image were taken with a JEM-200c transmission electron microscope operated at 200 kV.

X-ray Absorption Spectroscopy measurements: Ex situ O K-edge X-ray absorption spectroscopy (XAS) measurements were performed at 4-ID-C beamline of APS at Argonne National Laboratory. Samples were attached to a copper sample holder using conductive carbon tape in an argon-filled glovebox and then transferred from the glovebox into a transport container and then into an X-ray absorption antechamber through an argon environment to minimize the potential exposure to air. Data were measured simultaneously under both the total electron yield (TEY) mode from the sample photocurrent at $\sim 10^{-9}$ Torr and total fluorescence yield (TFY) mode using a silicon drift diode detector. The angle of X-ray incidence in TFY mode was adjusted to minimize the self-absorption while still being bulk sensitive. Data was obtained at a spectral resolution of ~ 0.2 eV, with a 2 s dwell time. During the measurement, three scans were performed at each absorption edge for each sample, and scans were then averaged to maximize the signal-to-noise ratio. The energy scale of the spectra was

calibrated with a Sr_2RuO_4 reference measured simultaneously.

3.2.3 Electrochemical tests:

2032 coin-type cells were used for electrochemical measurements. The electrodes consisted of active material, acetylene black, and polytetrafluoroethene (PTFE, 12 wt.%) binder with the weight ratio of 80:10:10. 1 M NaClO_4 in propylene carbonate (PC) was prepared as the electrolyte. Battery tester system HJ1001 SD8 (Hokuto Denko) were employed for galvanostatic testing.

3.3 Results and discussion

3.3.1 Crystal structure of P3 type layered oxide NMAMO

P3-type NMAMO cathode was successfully synthesized via a simple one-step solid state method. The crystallographic structure of the NMAMO sample was analyzed by X-ray diffraction (XRD) with the corresponding Rietveld refinement in **Figure 3.1**. It confirmed that the compound possesses a layered P3 structure belonging to the space group $R\bar{3}m$ symmetry without any impurities. The calculated curve is in good consistent with the experimental one with good reliability ($R_{wp} = 6.38\%$ and $\chi^2 = 3.145$). The lattice parameter is calculated to be $a = b = 2.86$, $c = 16.87$, $\alpha = \beta = 90^\circ$, $\gamma = 120^\circ$, respectively, and detailed refinement data is shown in **Table 3.1**.

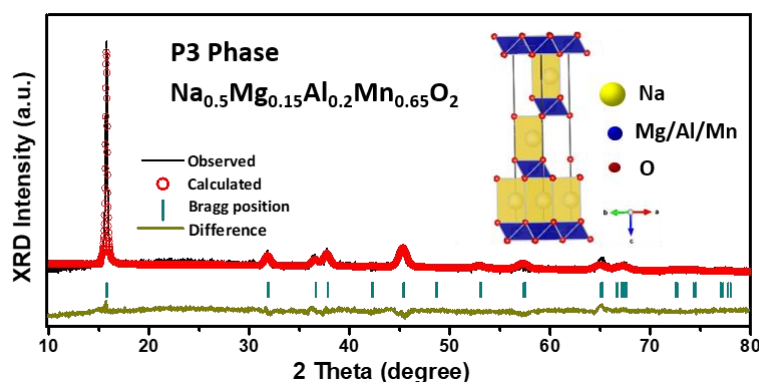


Figure 3. 1 Rietveld refinement XRD pattern of prepared P3-type NMAMO material.

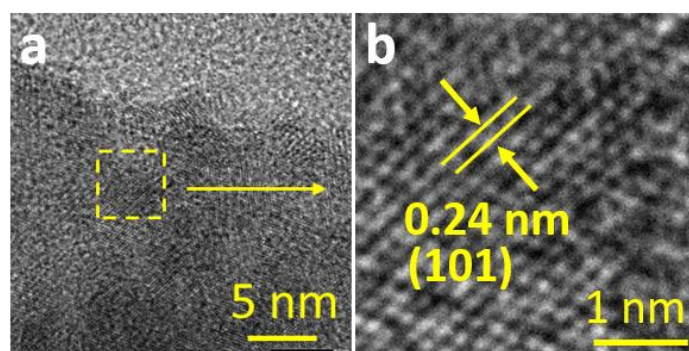
Table 3. 1 Refinement crystallographic parameters by Rietveld analysis for NMAMO. S.G. R 3m a =

b = 2.86, c = 16.87, $\alpha = \beta = 90^\circ$ $\gamma = 120^\circ$, Rwp = 6.38%, $\chi^2 = 3.145$.

Atom	site	x	y	z	Occ.
Na1	3a	0	0	0.836	0.5
Mg1	3a	0	0	0	0.15
Al1	3a	0	0	0	0.2
Mn1	3a	0	0	0	0.65
O1	3a	0	0	0.382	1
O2	3a	0	0	0.618	1

Table 3. 2 Stoichiometry from ICP analysis of the $\text{Na}_{0.5}\text{Mg}_{0.15}\text{Al}_{0.2}\text{Mn}_{0.65}\text{O}_2$ material.

		Na	Mg	Al	Mn
$\text{Na}_{0.5}\text{Mg}_{0.15}\text{Al}_{0.2}\text{Mn}_{0.65}\text{O}_2$	Conc.(mg/L)	1.141	0.367	0.553	3.687
	Stoichiometric ratio	0.4961	0.1529	0.2048	0.6703

**Figure 3. 2** Morphology TEM images with the enlarge figure of prepared P3-type NMAMO material.

The chemical composition of the obtained P3-NMAMO was confirmed by inductively coupled plasma (ICP), and the result is revealed in **Table 3.2**. The lattice fringes with 0.24 nm within NMAMO in extra transmission electron microscopy (TEM) is rationally ascribed to the (101) plane of P3 layered structure as shown in the **Figure**

3.2. Related energy dispersive X-ray spectroscopy (EDX) elementary mapping of the sample indicates the Na, O, Mg, Al and Mn elements are distributed uniformly in the sample, which is presented in the **Figure 3.3**.

3.3.2 Electrochemical performance of the P3 type layered oxide cathode NMAMO

As shown in the **Figure 3.4**, the galvanostatic electrochemical performance of P3-NMAMO is evaluated in a coin cell between 2 and 4.5 V at 10 mA g⁻¹. The initial charge capacity is 130 mAh g⁻¹, which is equivalent to removing of all Na⁺ from the lattice structure, with an almost flat plateau at approximately 4.3V. Since Mn⁴⁺ is difficult to further oxidize and Mg²⁺, Al³⁺ are inactive anodically, such a large charge capacity is most likely attributed to an unconventional redox mechanism with heavy involvement of oxide ligands. The subsequent discharge curve reveals a slope-like tendency, with a capacity of 177 mAh g⁻¹, corresponding to 0.65 Na⁺ inserted into the structure. It is worth noting that during the second charging process, the Na⁺ can be reversibly extracted from the crystal lattice with the flat plateau partially recovered.

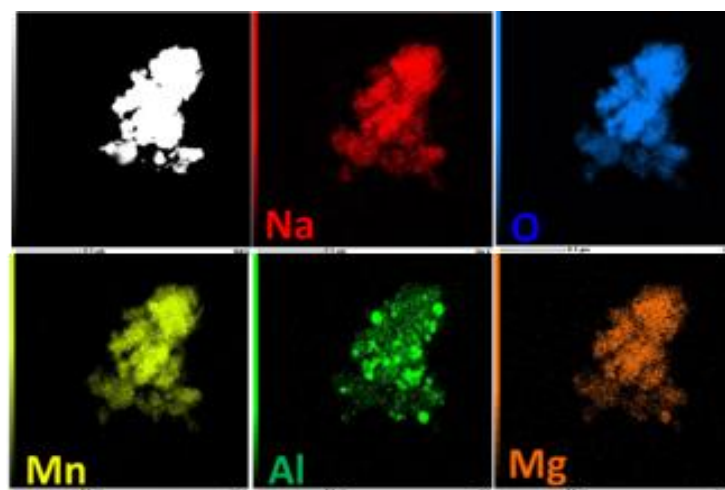


Figure 3. 3 Morphology TEM images with the corresponding elemental mapping of Na, O, Mg, Al and Mn of prepared P3-type NMAMO material.

The rate performance in **Figure 3.4b** shows that the capacity decreases stepwise as the current gradually increases, and it recovers to a high level when the current density returns to 10 mA g⁻¹, which indicates a strong capability of capacity recovery. The cycling capability for this compound at 200 mA g⁻¹ is shown in **Figure 3.4c**. The initial capacity reaches 122 mAh g⁻¹, and nearly 100 mAh g⁻¹ can be maintained after 100 cycles. Moreover, the coulombic efficiency remained around 99% throughout, including the first cycle. The corresponding cycling performance at 10 mA g⁻¹ within the P3 type NMAMO cathode is revealed in **Figure 3.5** and capacity can maintain nearly 150 mAh g⁻¹ after 20 cycles.

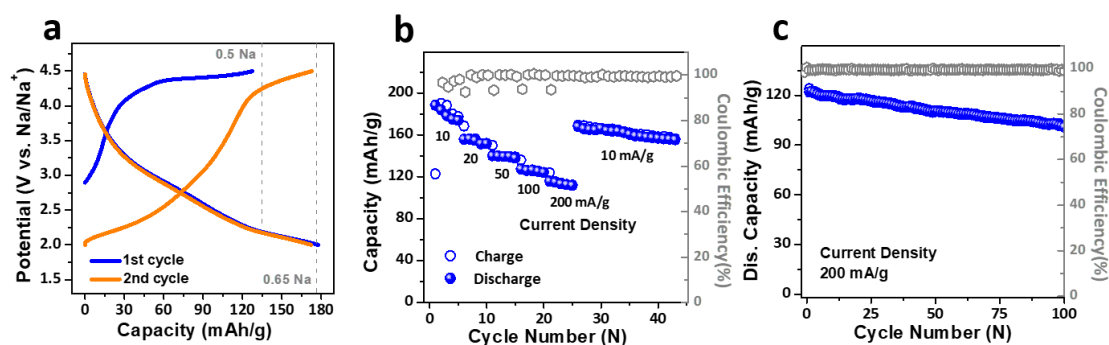


Figure 3. 4 (a) Charge/discharge curves for the initial two cycle with collected within the voltage range from 2 to 4.5 V vs. Na/Na⁺ with the current density of 10 mA g⁻¹. Cycling performance of the electrode (b) at the different current density and (c) at a high current density of 200 mA g⁻¹.

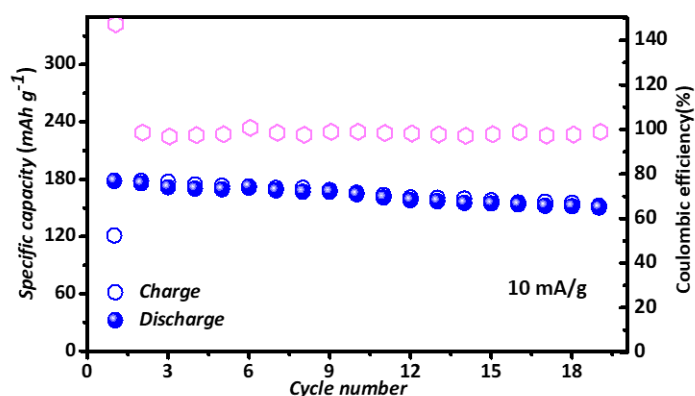


Figure 3. 5 The cycling performance of the NMAMO electrode at current density of 10 mA g⁻¹.

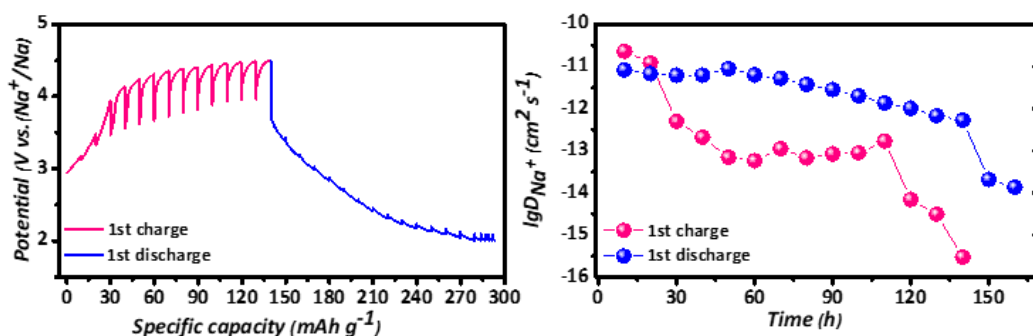


Figure 3. 6 GITT results of P3-NMAMO cathode for the first cycle with the variation of quasi-equilibrium potentials and the calculated Na^+ diffusion coefficient.

Additionally, GITT measurements were conducted to estimate the Na^+ diffusion coefficient as shown in the **Figure 3.6**, which underpins the kinetics of P3-NMAMO upon cycling. The detailed parameters, labeled in **Figure 3.7** for charge and discharge, suggest the prospective performance at high current density.

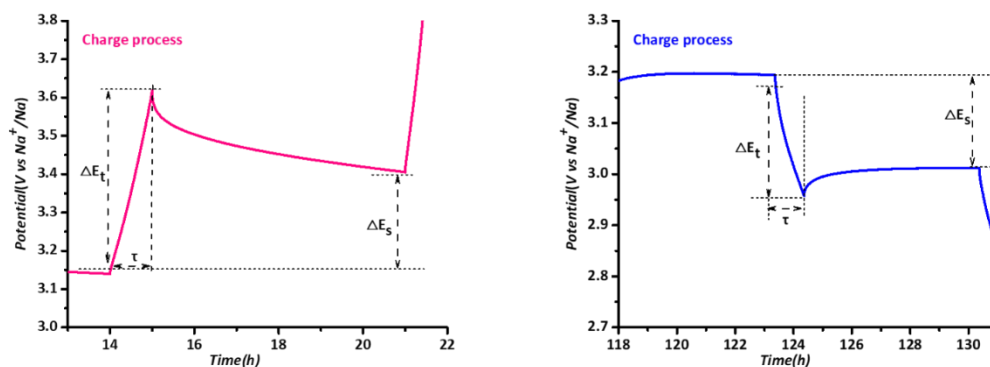


Figure 3. 7 The potential profile for a single titration at 3.15 V during charge process with labelling the different parameters (left). The potential profile for a single titration at 3.18 V during discharge process with labelling the different parameters (right). The simplifying equation of Fick's second law to calculate diffusion coefficient (D/R^2), where τ is the limited time period, n is the mole number of the electrode, V_m is the molar volume of the NMAMO, S is the area of electrode, ΔE_s and ΔE_t are the change in the steady state potential and the total change during the current flux by deducting the IR drop, respectively.

3.3.3 Phase transition in P3 type layered oxide NMAMO during cycling

Operando XRD was employed to record the crystal structural evolution of P3-NMAMO cathode material induced by extraction and insertion of Na^+ during the initial two cycles between 2 and 4.5 V. P3 layered structure is preserved during the desodiation/sodiation process in **Figure 3.8** and the position of the major peak reversibly shift as a function of sodium content. In addition, the peak intensities decrease and no distinct new peaks can be observed compared to the initial structure. The (003) peak shifted to lower angle during the initial stage of the first charge process, which is corresponding to the increase of the c parameter. It can be rationally attributed to the increased repulsive interaction of oxygen ions between the adjacent layers within Na^+ de-intercalation process. During the latter stage of the first charge process, the peak position of the (003) peak kept constant and even without any obvious shift. The decrease of the interlayer distance may be ascribed to the increase in the concentration of local stacking faults based on the previous reports of $\text{Na}_{0.8-x}[\text{Li}_{0.12}\text{Ni}_{0.22}\text{Mn}_{0.66}]\text{O}_2$.¹³¹⁻¹³² The intensity of the peaks decreases and peaks become broad in the following initial charging process.

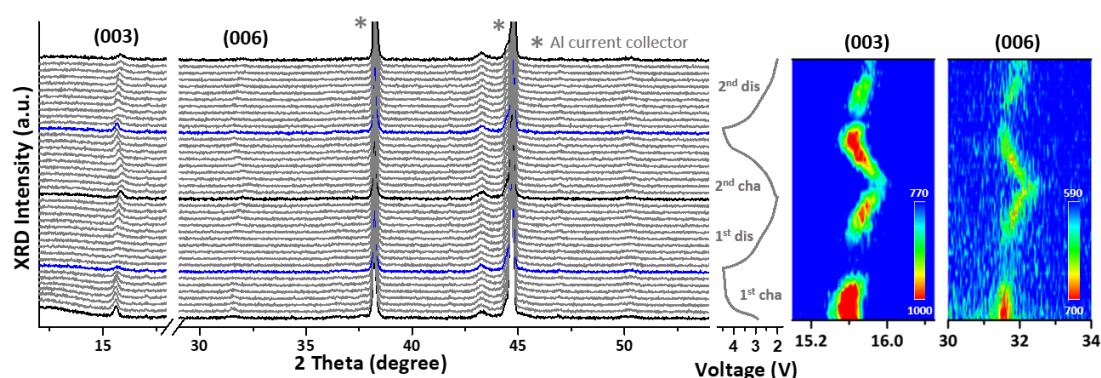


Figure 3. 8 Capacity-dependent in-situ XRD curves of NMAMO cathode collected during the initial two cycles with the corresponding contour graph.

This phenomenon indicates an irreversible reaction on the initial charging, probably

attributed to some evolution species from the electrode material, such as in Li_2MnO_3 -based oxides.¹³³ Moreover, the reversible shift with the regular change of the lattice parameter was revealed in the second galvanostatic cycle. The corresponding contour graph is also presented with the evolution of (003) and (006) reflection to show the clear information.

In **Figure 3.9**, refinements of ex-situ XRD patterns were employed to further investigate the structural stability of P3-NMAMO cathode after cycling. We note that the layered structure can be well maintained even after 100 galvanostatic cycles as presented. Furthermore, the the XRD pattern was obtained after exposure for 3 months in order to further investigate the relative stability in air of P3-NMAMO cathode.

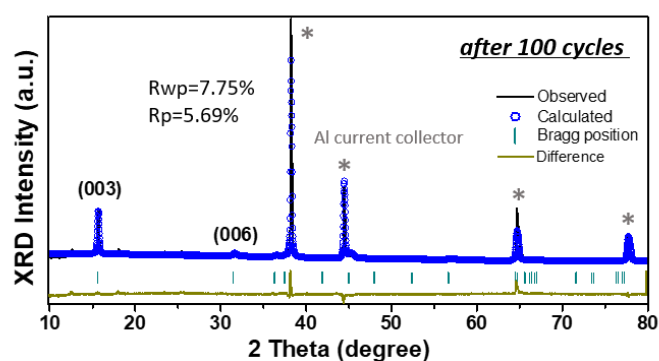


Figure 3. 9 The Rietveld XRD refinement of the NMAMO cathode after 100 cycles.

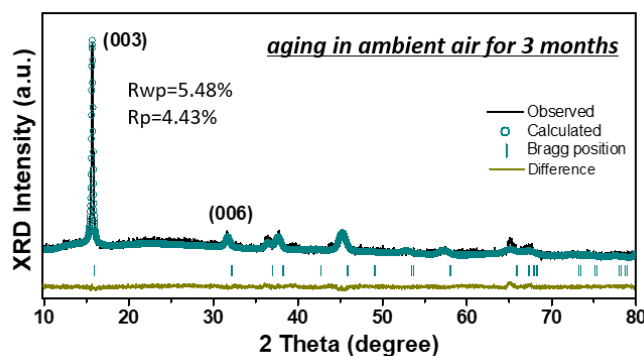


Figure 3. 10 The Rietveld XRD refinement of the NMAMO pristine powder aging in ambient air for 3 months.

Table 3.3 Refinement crystallographic parameters by Rietveld analysis for NMAMO cathode after 100 cycles.

<i>Space group</i>	R 3m	
	<i>a</i>	2.88
	<i>b</i>	2.88
	<i>c</i>	17.07
<i>Cell parameters</i>	<i>a</i>	90 °
	β	90 °
	γ	120 °
<i>Agreement factors</i>	<i>Rwp%</i>	7.75
	<i>Rp%</i>	5.69
	χ^2	5.065

As shown in **Figure 3.10**, the XRD pattern after aging in ambient air for 3 months reveals a good consistency with a standard P3-type structure without any change. It suggests an excellent structural stability within the P3-NMAMO material exposure in air. Extra detailed refinement parameters are revealed in **Table 3.3-3.4**.

Table 3.4 Refinement crystallographic parameters by Rietveld analysis for NMAMO aging for 3 months.

<i>Space group</i>	R 3m	
	<i>a</i>	2.83
	<i>b</i>	2.83
	<i>c</i>	16.70
<i>Cell parameters</i>	<i>a</i>	90 °
	β	90 °
	γ	120 °
<i>Agreement factors</i>	<i>Rwp%</i>	5.48
	<i>Rp%</i>	4.43
	χ^2	2.183

3.3.4 Oxygen related anionic redox chemistry within the P3 type NMAMO

X-ray photoelectron spectroscopy (XPS) is further employed to investigate the

related charge compensation mechanism within the P3-NAAMO cathode during the electrochemical performance process. As displayed in **Figure 3.11**, Mn begins with the +4 state and no obvious shift or broadening for the peaks has been observed at the 1st charged state, which suggests that Mn does not contribute to the charge compensation during the initial charging process. During the subsequent discharge process, a negative shift can be observed within the Mn 2p_{3/2} and Mn 2p_{1/2} peaks, which indicates the emergence of Mn³⁺. However, the reduction of Mn⁴⁺ was not complete at the end of the first discharge state, due to the coexistence of Mn³⁺ and Mn⁴⁺.

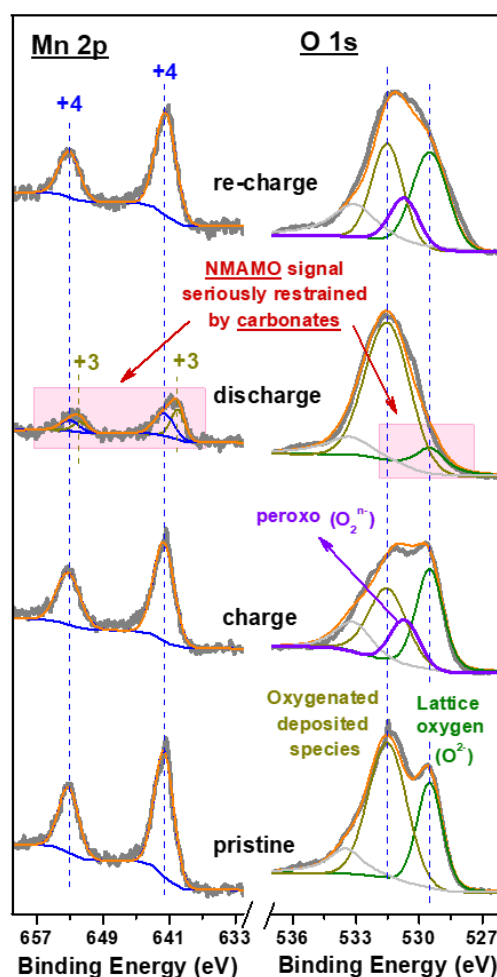


Figure 3. 11 Mn 2p and O 1s XPS spectra collected from NMAMO cathode at various states with: pristine, 1st charged, 1st discharged and 2nd charged states.

The presence of a novel signal around 530.7 eV appears during the initial charging

as for the O1s spectra. This signal can be rationally ascribed to the depletion of charge from oxide ligands, which suggests that upon the initial charging the charge compensation is merely centered at oxygen. XPS spectra of NMAMO cathode electrode for re-charged state shows the reversible progression of both cationic ($\text{Mn}^{3+}/4+$) and anionic ($\text{O}^{2-}/\text{O}^{\text{n-}}$) redox. However, it is worth noting that a significant decrease of the NMAMO electrode signal is observed at the initial fully discharged state. This phenomenon implies that the NMAMO signal is likely to be covered by the formation of carbonate-related species. Besides, additional XPS evidence (Mg 1s and Al 2p spectra in **Figure 12**) further confirm that the charge compensation mechanism can rationally be assigned to the activity of O and Mn.

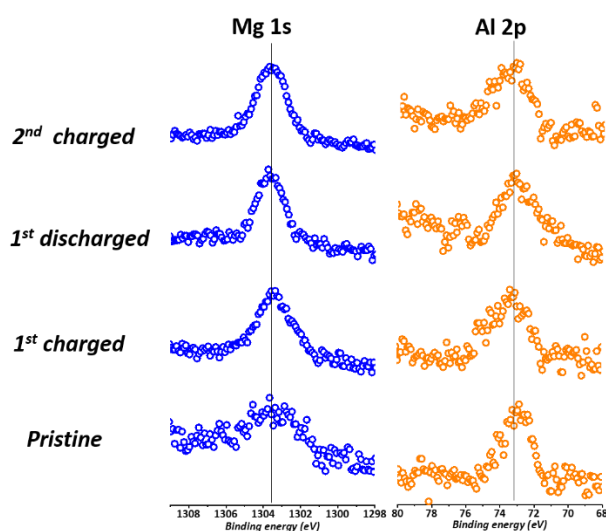


Figure 3. 12 Mg 1s and Al 2p spectrum collected from NMAMO cathode at various states with: pristine, 1st charged, 1st discharged and 2nd charged states.

Since XPS measurement is surface sensitive with the detection depth of 3-5 nm, we use O K-edge X-ray absorption spectroscopy (XAS) to further investigate the evolution of the O electronic structure concurrent accompanied with Na (de)intercalation mainly based on the total fluorescence yield (TFY) mode to study the specific reaction. The O K-edge XAS spectrum is used to probe the dipole-allowed transition from O 1s to empty O 2p states.¹³⁴ Generally, the spectrum can be divided into two regions. The pre-

edge, at ≤ 535 eV, represents the transition to unoccupied states of O $2p$ -Mn $3d$ hybridized orbitals. And the broad band above 535 eV, can be rationally corresponding to the excitation to empty states of O $2p$ orbitals mixed with Mn $4s$ and $4p$ orbitals, followed by higher states and multiple scattering events of the ejected electrons. The position of the pre-edge peak is affected by the change in the effective nuclear charge Z_{eff} of the ligand and the distribution of d states due to ligand field effects determined by the strength of the covalent Mn-O bonds. The intensity of these peaks reflects both the number of unoccupied hybridized states and the contribution of O to their wave function. Therefore, the measurements offer insight into the role of O states and any changes in covalency. It is worth noting that the XAS spectra were measured simultaneously under both TEY and TFY modes. The TEY mode with a probing depth around 10 nm only provides surface information similar to XPS, whereas the TFY mode could penetrate 100-nm into the electrode. Therefore, herein the focus was placed on TFY O K-edge XAS.

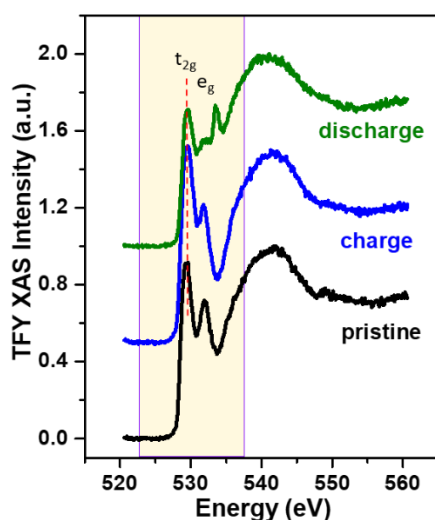


Figure 3. 13 O K-edge XAS spectra for NMAMO cathode using TFY mode at pristine, 1st charged, 1st discharged state respectively.

The TFY O K-edge spectrum shown in the **Figure 3.13** of the pristine state exhibits

two distinct pre-edge peaks centered at 529.4, and 532.0 eV, respectively, which is corresponding to the transition to unoccupied t_{2g} and e_g orbitals of O $2p$ -Mn $3d$ hybridization similar to the spectrum of MnO_2 .¹³⁵

After charge to 4.5 V, the t_{2g} feature experienced a prominent increase in the intensity with little change in energy, and the e_g feature slightly moved to lower energy while remaining constant in the intensity (**Figure 3.14**). This behavior reflects the increase of the unoccupied states predominately in t_{2g} orbitals, which can be ascribed to the new unoccupied states centered at the O given the lack of visible change in the oxidation state of Mn based on both the XPS results above and corresponding spectra at the Mn L_2 -edge (**Figure 3.15**).

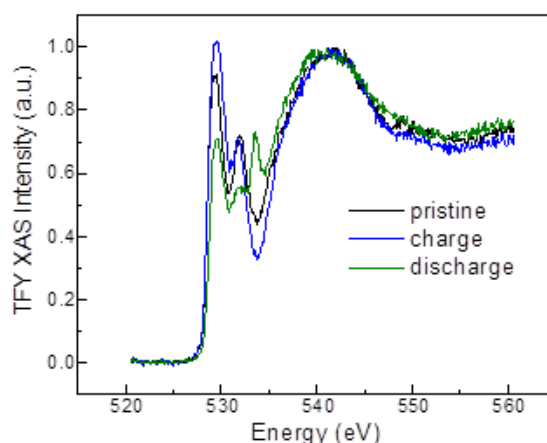


Figure 3. 14 Ex situ O K-edge XAS spectra of NMAMO electrode at different states: pristine, 1st charged, 1st discharged state respectively.

Upon discharge to 2 V, both t_{2g} and e_g peaks underwent a dramatic decrease in the intensity and a small energy shift to higher energy relative to the previous state (**Figure 3.16**). It is reflecting a significant reduction of the unoccupied states of O $2p$ -Mn $3d$ mixed bonds attributed to the conventional Mn^{4+}/Mn^{3+} redox reactions, which is again consistent with XPS results and Mn L_2 -edge XAS spectra.¹³⁶ In addition, the intensity of both peaks was even smaller than the pristine state after the discharge

process, which suggests that less unoccupied states was obtained after discharge, which is congruous with additional Na intercation beyond the starting composition. Besides, the discharging process contributed to the formation of a new sharp peak at ~ 533.6 eV, which can be assigned to C=O bonds, such as in carbonates, mainly at the surface.¹³⁷

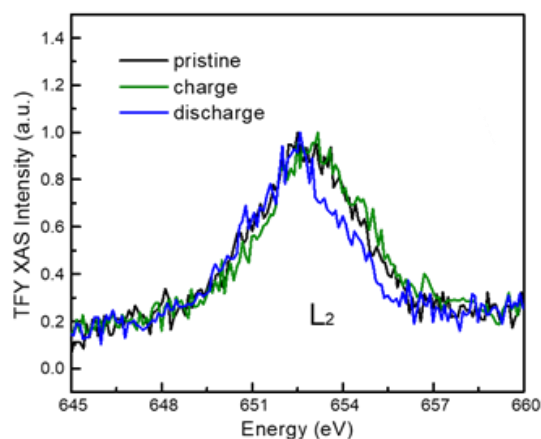


Figure 3. 15 Ex situ Mn L-edge XAS spectra of NMAMO electrode at different states of charge. For L2-edge, the peak position remained constant upon charge and shifted to lower energy in the subsequent discharge, suggesting the preservation of Mn^{4+} upon charge and the reduction of Mn upon discharge.

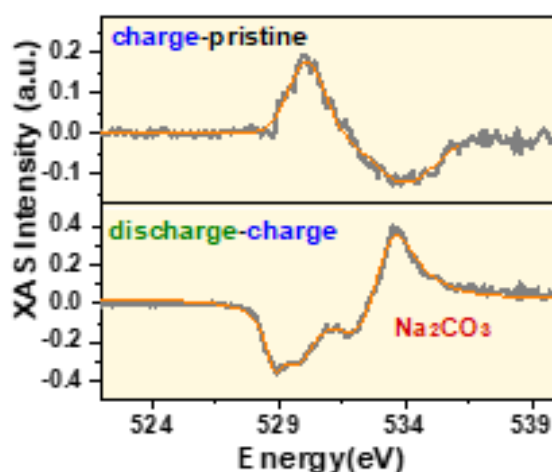


Figure 3. 16 The difference spectra of O K-edge XAS results (c) between that of 1st charged state and that of pristine state; between that of 1st discharged state and that of 1st charged state.

This peak is, accordingly, dominant in the TEY O K-edge spectrum of this state as

shown in the **Figure 3.17**. Based on all these ex-situ spectroscopies results, the states containing oxygen at the surface are quite different from the bulk after the 1st discharge, which is again consistent with the XPS data. To get further insights into the charge compensation process, we embarked on a systematic analysis of in-situ Raman and Differential Electrochemical Mass Spectrometry (DEMS).

As shown in **Figure 3.18**, upon initial charging, pronounced peaks arise at 825 cm⁻¹, which can be ascribed to the peroxo-related O-O stretching mode.¹³⁰ In addition, this species was highly reversible during cycling during de-/sodiation (see the green bars in Figure 4b). After charging to 3.8 V, a new peak is observed at 1105 cm⁻¹, which can be assigned to the formation of superoxo-related species.

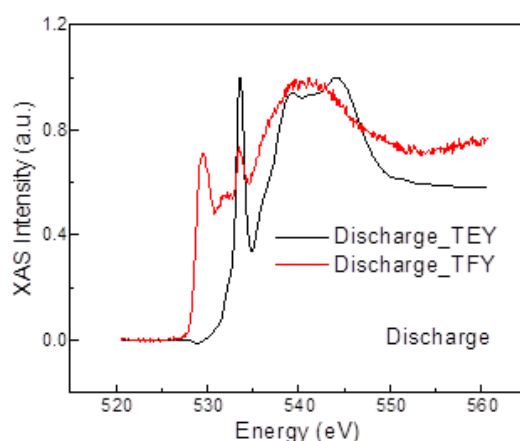


Figure 3. 17 Ex situ O K-edge XAS spectra of NMAMO electrode after fully discharged to 2 V.

The charge depletion centered at O that is required for these species to form could be related to the increase in intensity of the pre-edge peaks in the O XAS spectrum, since non-bonding states are predicted to be located near Mn-O hybridized states. It is anticipated that the superoxo-related species will attack the propylene carbonate (PC) in the electrolyte, resulting in a series of parasitic products derived from decomposition of the solvent with peaks at 982-1013 cm⁻¹. This is also consistent with the signal detected at 1083 cm⁻¹, which is the typical peak of carbonates, and further confirms the existence of parasitic products.^{124, 138}

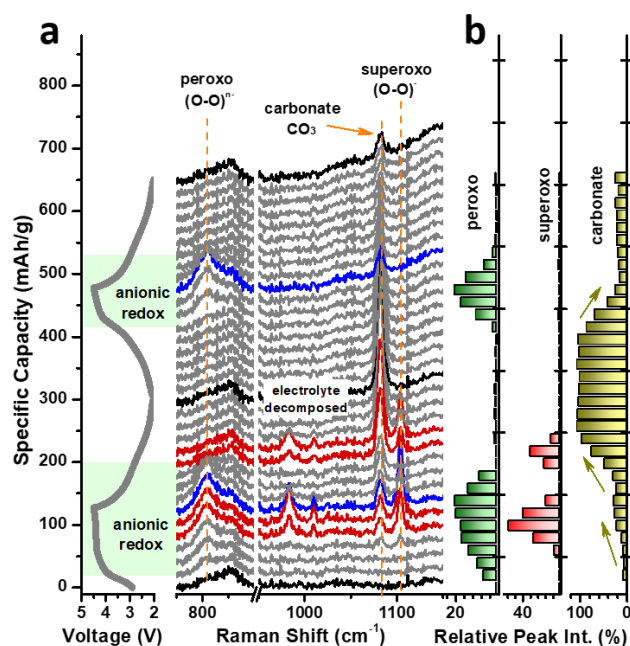


Figure 3. 18 (a) Capacity-dependent In-situ Raman spectra collected on NMAMO cathode recorded during initial cycle. (b) Raman peak intensities are demonstrated within the corresponding voltage profiles: peroxy-species (green blocks), superoxy-species (red blocks) and carbonate species (yellow blocks).

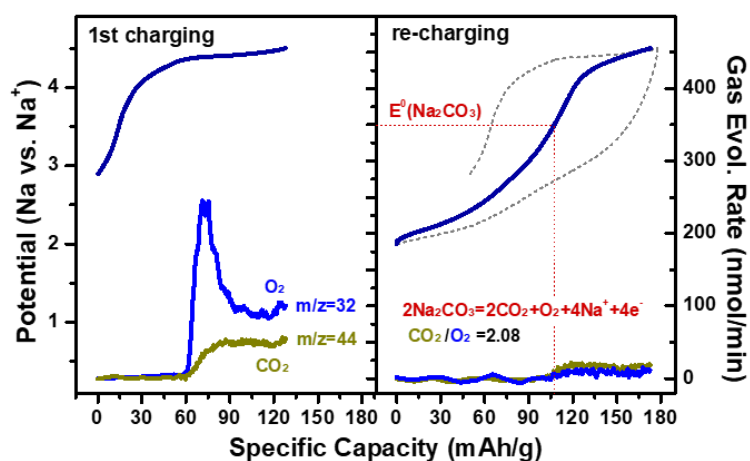


Figure 3. 19 In-situ DEMS results of gas evolution rates for O₂ and CO₂ collected during the first and second charging process.

More specifically, the nucleophilic attack from superoxo radical against PC molecule

has been clearly demonstrated and assigned in our previous work. The observations from corresponding *operando* DEMS upon initial charging are consistent with the Raman spectra, as shown in **Figure 3.19**. CO_2 is emitted from the decomposition of Na_2CO_3 or electrolyte and presents increase tendency in the superoxo-related range. The evolution of O_2 reveals the responsible reason for the irreversible capacity decay. It is unusual that the intensity of Na_2CO_3 Raman signal basically remained unchanged even at the end of the initial charging and it can be rationally assigned to the equivalent rate for formation and decomposition of Na_2CO_3 .

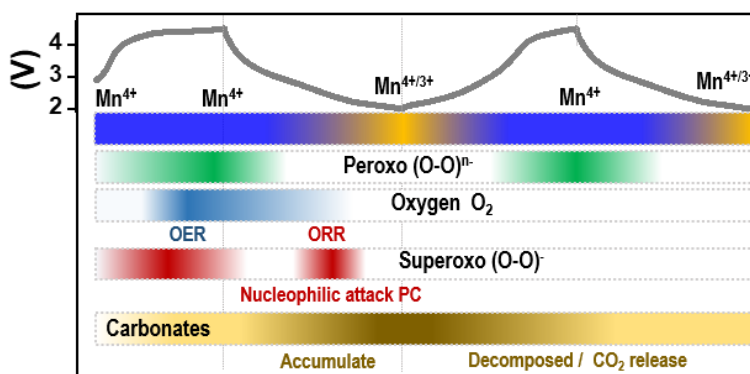


Figure 3. 20 Unified picture of cationic and anionic redox in related P3-NMAMO during the first two galvanostatic cycles.

Moreover, it is worth noting that the superoxo-related signal is re-observed during the 1st discharging, which is presumably due to the oxygen reduction reaction (ORR) with the released oxygen trapped inside the sealed coin cell. However, neither superoxo-related species nor oxygen can be detected in the second cycle, which is claimed as the pre-activation process of anionic redox reactivity as for the Li-rich materials. Knowing this, the corresponding unified picture of charge compensation process in P3-NMAMO cathode is shown in **Figure 3.20**. In this case, for the initial charging, the overall electrochemical activity can be rationally ascribed to the role of oxygen ligands. Upon the subsequent discharging, conventional $\text{Mn}^{4+}/\text{Mn}^{3+}$ redox as

proxy for states with participation of both metal and O due to the covalency takes part in the charge compensation process. In addition, at the end of the first discharging, the carbonates related species is accumulated most prominently.

3.4 Summary

We have reported a newly Na-deficient layered P3-type $\text{Na}_{0.5}\text{Mg}_{0.15}\text{Al}_{0.2}\text{Mn}_{0.65}\text{O}_2$ material by a simple solid-state reaction. The experimental evidence for the structural stability of this cathode upon desodiation/sodiation was demonstrated via *operando* and *ex situ* XRD. It has been confirmed that activity involving the oxide anions is presented within P3-NMAMO cathode material by our detailed spectroscopic investigation not only at surface (by XPS) but also in the bulk (by XAS). Meanwhile, irreversible oxygen release is quantitative tracked from the DEMS spectroscopy during the first cycle. Moreover, the formation of reversible peroxo-related species or superoxo-related species can be detected during the dynamic process combined with the *operando* Raman. Based on the evidence collected, charge compensation during the initial charging is achieved via oxygen-related oxidation process. The superoxo-related species gradually increase along with the peroxo-related species range, it is rationally ascribed to the ORR process. It can be attributed to the trapped molecular oxygen which can supply the amount of superoxo. The accumulation of the carbonate-related species upon the initial discharging is resulted from the irreversible oxygen release within the initial charging. Fortunately, neither superoxo nor oxygen can be detected during the second cycle, suggesting a reversible state has been achieved. These findings will provide deeper insights and new ideas to design new cathode materials for Na batteries with high energy density, in which the ligands redox play a crucial role.

Chapter 4. Identifying anionic redox activity within the related P2 type cathode

4.1 Introduction

Rechargeable Li-ion batteries have been considered as the potential alternatives for commercial portable electronic devices and large-scale energy storage technologies.¹³⁹⁻¹⁴⁰ However, the further application of the Li-ion batteries is limited, which is due to the unevenly geographical distribution and expensive price of the lithium resource.¹⁴¹⁻¹⁴² The Na-ion batteries have been regarded as the promising candidates based on the high abundance and low cost of the sodium resource. In addition, the intercalation compounds have been focused intensively among the various electrode materials for sodium ion batteries.^{79, 92}

Currently, layered oxide compounds are considered as the most competitive cathodes among the numerous investigated intercalation cathodes and the general formula of the layered oxide compounds is Na_xTMO_2 (TM: transition metal).^{79, 143} Advantage of the layered oxide compounds is simple to be synthesized and feasible potential to obtain the higher theoretical capacities. O3 type and P2 type layered structure have become the powerful contenders as the most general ones among the layered oxide materials. “P” and “O” represents the corresponding environment of Na^+ site between TMO_2 layers within the different layered structure.⁹⁶ And P corresponds to the prismatic site while is corresponding to the octahedral site. The numbers signify the repeat number of the TMO_2 layers within the unit cell: the stacking sequence within the P2 type layered structure is following the ABBA patterns while the O3 type layered structure designate stacking following the ABCABC sequence.

Though extensive reports have been published within the Na-ion layered oxide cathodes based on the traditional cation related redox reaction, oxygen related anionic

redox based layered oxide cathodes have been widely studied simultaneously. Furthermore, the significant advantage of the anionic redox behavior is the higher oxygen related potential and increased capacity.¹⁴⁴⁻¹⁴⁵ The layered oxide cathodes based on both cationic redox and anionic redox process are identified as the promising paradigms for improving the energy density of sodium ion batteries, within which the charge compensation process can be satisfied not only with transition metal ions but also with the oxygen ions. Intermediate honeycomb ordered O3 layered oxide Na_2RuO_3 is studied by Yamada and his colleagues, which delivers a large capacity based on the oxygen redox induced by a spontaneously ordered intermediate Na_1RuO_3 .¹⁰⁹ Similarity, simultaneous cationic and anionic redox process is generated within the O3 type layered oxide Na_2IrO_3 with excess sodium ions located in the TM layer, which is confirmed by a series of complementary characteristic measurements by Tarascon's group.¹⁴⁶ P2 type layered oxide $\text{Na}_{0.72}[\text{Li}_{0.24}\text{Mn}_{0.76}]\text{O}_2$ within lithium ion substituted in the transition layer is investigated by Hu's group and the exceptionally high charge capacity of 210 mAh g^{-1} can be obtained during the initial cycle. It is worth noting that the charge capacity during the first charging is rationally attributed to the pure oxygen oxidation reaction process.¹⁰⁸ Bruce et al have investigated the $\text{Na}_{2/3}[\text{Mg}_{0.28}\text{Mn}_{0.72}]\text{O}_2$ with P2 type layered structure and demonstrated the excellent electrochemical performance of large capacity which is ascribed to the oxygen related anionic redox reaction triggered by the Mg^{2+} residing in the TM layers.⁹⁹ The presentation of the corresponding oxygen redox process is particularly related the different structure, O3 or P2 type layered structure. Herein, the related oxygen related anionic redox process is identified by the P2 type layered oxide P2- $\text{Na}_{0.6}\text{Li}_{0.35}\text{Fe}_{0.1}\text{Ru}_{0.55}\text{O}_2$ (P2-NLFR) compound. Moreover, the corresponding oxygen behaviors are investigated by comprehensive spectroscopic characterizations. In specific, the oxygen related anionic redox activity is easy to be triggered within cut off voltage of 4 V within the P2 type NLFR cathode. It reveals a

larger capacity, stable cycling performance as well as the excellent rate performance. Our finding paves the new way for a rational design point of view of higher energy density cathode for practical NIBs.

4.2 Experiment and characterization

4.2.1 Preparation of P2 $\text{Na}_{0.6}\text{Li}_{0.35}\text{Fe}_{0.1}\text{Ru}_{0.55}\text{O}_2$ (P2-NLFR) material

P2- $\text{Na}_{0.6}\text{Li}_{0.35}\text{Fe}_{0.1}\text{Ru}_{0.55}\text{O}_2$ (P2-NLFR) material was synthesized by solid state reaction from stoichiometric amounts of Na_2CO_3 , Li_2CO_3 , Fe_2O_3 and RuO_2 , and amount of Na_2CO_3 was added with 2 wt% excess. The starting stoichiometric mixture was initially ground together and then held at 600 °C for 10 h under air atmosphere. After re-grinding, the powder was heated to 900 °C for another 15 h, again under air atmosphere. The resulting black powder was reground and carefully checked for impurity phases using x-ray diffraction.

4.2.2 Characterization

The structure of P2- $\text{Na}_{0.6}\text{Li}_{0.35}\text{Fe}_{0.1}\text{Ru}_{0.55}\text{O}_2$ (P2-NLFR) cathode material was identified by powder XRD (Ultima III, Rigaku Corporation) radiation from Cu $K\alpha$ ($\lambda = 1.5406 \text{ \AA}$). The data were collected between diffraction angles (2θ) from 10° to 80° at a scan rate of 2° per min. Rietveld refinements of the XRD pattern obtained by GSAS + EXPGUI suite. The morphologies of the materials were procured by SEM (JSM-7000F). TEM and HRTEM were performed on a JEOL JEM-2100 electron microscope equipped with an X-ray EDS. In-situ Raman spectra of the materials were obtained using a homemade mould and JASCO microscope spectrometer (NRS-1000DT). XPS was characterized by a Thermo Fisher Scientific Model $K\alpha$ spectrometer equipped with Al $K\alpha$ radiation (1486.6 eV). Before XPS test, the sample was transferred into an Ar glove box and sealed in an airtight container to avoid the exposure with the humidity.

4.2.3 Electrochemical tests

2032 coin-type cells were used for electrochemical measurements. The electrodes consisted of active material, acetylene black, and polytetrafluoroethene (PTFE, 12 wt.%) binder with the weight ratio of 80:10:10. 1 M NaClO₄ in propylene carbonate (PC) was prepared as the electrolyte. Battery tester system HJ1001 SD8 (Hokuto Denko) were employed for galvanostatic testing.

4.3 Results and discussion

4.3.1 Crystal structure of P2 type layered oxide NLFR

The X-ray diffraction pattern of the obtained P2-NLFR is revealed in the **Figure 4.1** and the major diffraction peaks can be indexed to the P2 type layered structure with the space group P6₃/mmc. The other minor phase can be rationally ascribed to RuO₂. And the peak located at around 18 degree can be rationally attributed to the superlattice peak, which can be assigned to Li₂RuO₃ compound.

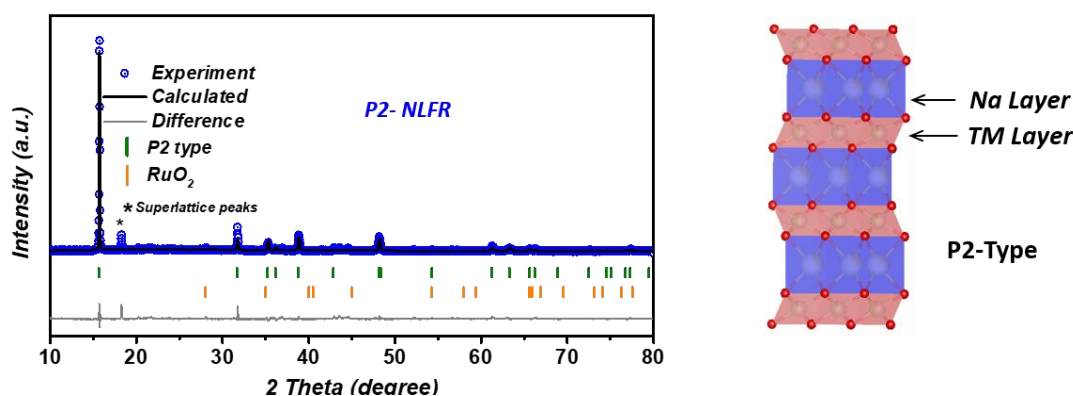


Figure 4. 1 Rietveld refinement XRD patterns of P2-NLFR cathode.

The Rietveld refinement of XRD pattern within the P2 type layered oxide NLFR is carried out by GSAS + EXPGUI suite and the result confirms that the dominate phase of the obtained material is P2 type layered structure. The specific results of the refinement are presented in the **Table 4.1** and the weight fraction of the major P2 type

structure within the obtained material is 97.6%. It is worth noting that the minor phase RuO₂ performs no electrochemical activity and makes no contribution to the corresponding electrochemical performance. Furthermore, the specific inductively coupled plasma spectroscopy is further employed to confirm the related component, which is shown in the **Table 4.2**.

Table 4. 1 Refinement results of P2-NLFR sample.

Space group <i>P63/mmc</i>			a=2.9352	c=11.2699	Vol=84.084	
P2 phase~97.6%			RuO ₂ ~2.4%			
Atom	site	x	y	z	Occ.	
Na1	4e	0	0	0.25	0.15	
Na2	2c	0.33	0.67	0.25	0.35	
Na3	2b	0	0	0.239	0.10	
Fe1	2a	2	0	0	0.1	
Ru1	2a	2	0	0	0.55	
Li1	2a	2	0	0	0.35	
O1	4f	0.33	0.67	0.11	1	
	Rwp(%)	15.6				
Agreement factors	χ^2	2.72				

Table 4. 2 Stoichiometry from ICP analysis of the P2-NLFR pristine material.

		Na	Li	Fe	Ru
P2-NLFR	Conc.	5.9	1.0	2.4	22.6
Stoichiometric ration		0.256	0.142	0.042	0.223

4.3.2 Morphology of P2 type layered oxide NLFR

Extra TEM images of the obtained P2-NLFR material are shown in the **Figure 4.2**. The pristine sample performs the micro size with the irregular dimensions from the **Figure 4.2a**. The lattice fringes obtained from the P2-NLFR layered material shows the

spacing of 0.54 nm, which is rationally assigned to the 002 plane of P2 layered structure.

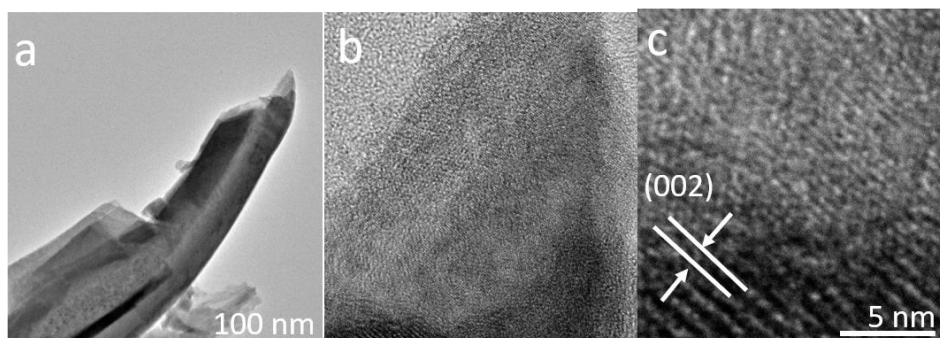


Figure 4. 2 Morphology characterization of prepared P2-NLFR a, b) TEM images, and c) HRTEM images.

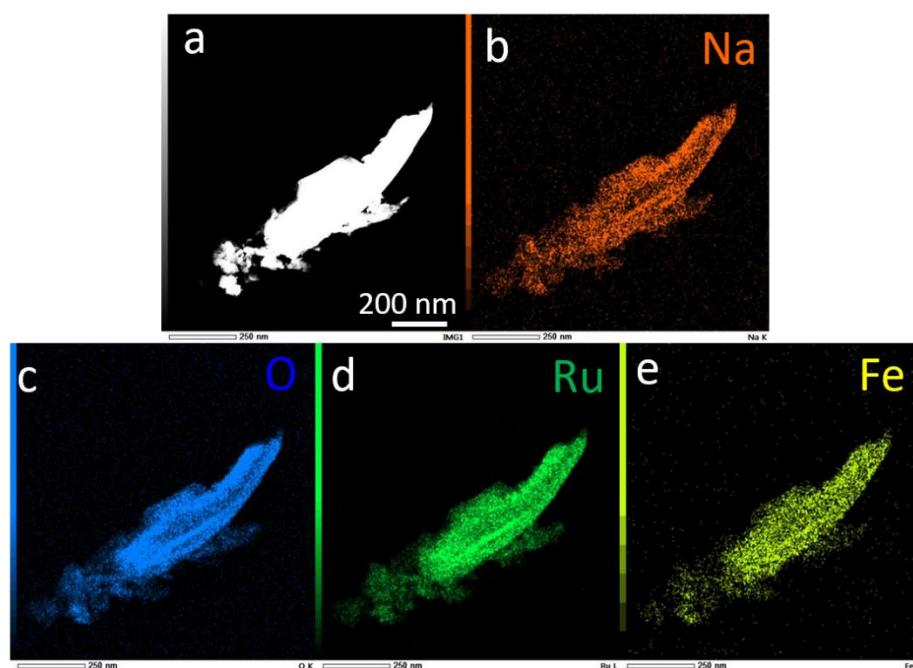


Figure 4. 3 TEM image of P2-NLFR material with the corresponding elemental maps of Na, Fe, Ru and O.

The EDX elemental mapping within the P2 type layered oxide NLFR is effectively identified in the **Figure 4.3**, which suggests that the elements are distributed homogeneously. Due to the low characteristic spectral energy of lithium, the EDX element mapping of Li cannot be detected.

4.3.3 Electrochemical performance of P2 type layered oxide NLFR

The galvanostatic charge discharge profiles within the P2 type NLFR are revealed in the **Figure 4.4**. Charge/discharge curves of the initial three cycles at 10 mA g^{-1} is shown in the **Figure 4.4a**. During the initial sodium deintercalation process, the actual charge capacity is 126 mAh g^{-1} corresponding to deintercalation of 0.46 Na^+ , which is far more than the specific capacity 27 mAh g^{-1} based on the cationic redox process. As a matter of fact, it is noteworthy that the major part of the charge capacity for first cycle is out of the consideration of cation based redox reaction.

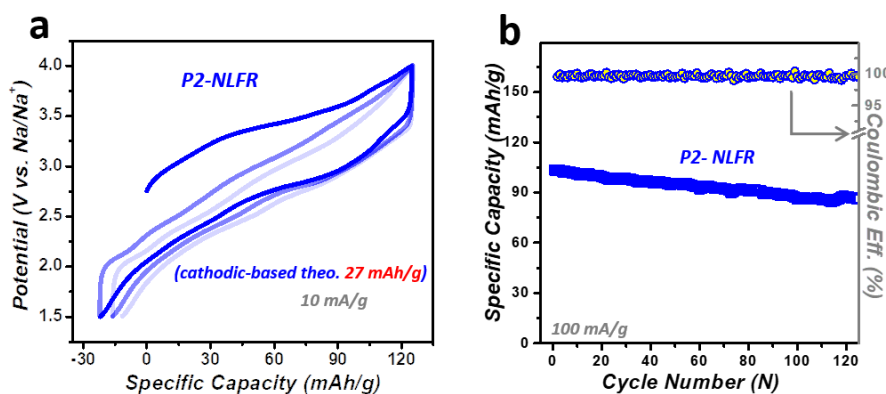


Figure 4. 4 (a) The voltage profiles collected between 1.5 to 4.0 V vs. Na/Na^+ at a rate of 10 mA g^{-1} of P2-NLFR. (b) Cycling performance of P2 type NLFR as a function of cycle number at 100 mA g^{-1} .

Thus, it is suggesting that the major of the initial charge capacity is rationally attributed to the oxygen related anionic redox reaction, which can satisfy the charge compensation during the charge and discharge process. In addition, cycling performance of P2-NLFR layered oxide at 100 mA g^{-1} is revealed in the **Figure 4.4b** and nearly 80 mAh g^{-1} capacity can be maintained after 123 cycles. It presents good cycling performance within the P2 type layered oxide NLFR. Also, the cycling performance of the P2 NLFR at 20 mA g^{-1} is performed in the **Figure 4.5**. From the figure, the capacity for the initial cycle is nearly 130 mAh g^{-1} . After 35 cycles, the

capacity can maintain with 110 mAh g^{-1} , which suggests the relative good cyclability.

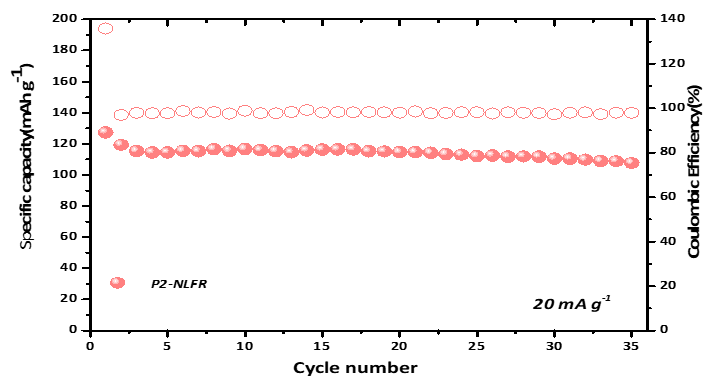


Figure 4. 5 Cycling performance of P2 type NLFR as a function of cycle number at 20 mA g^{-1} .

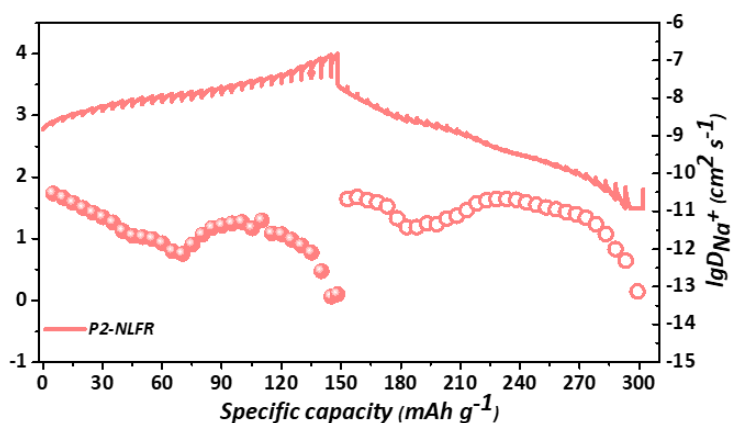


Figure 4. 6 GITT results of P2-NLFR for the first cycle with the variation of quasi-equilibrium potentials and the calculated Na^+ diffusion coefficient.

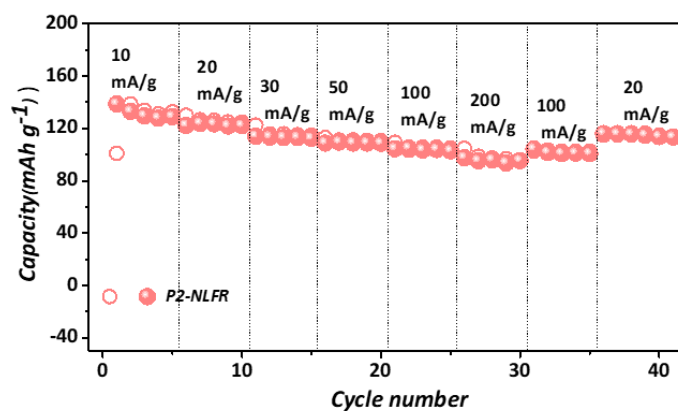


Figure 4. 7 Rate performance of P2-NLFR electrode with the current density of 10, 20, 30, 50, 100

and 200 mA g⁻¹, respectively.

Additionally, the calculated sodium ion diffusion coefficient within the P2 type layered oxide NLFR to the equation is shown in the **Figure 4.6** and the diffusion coefficient is from 10⁻¹³ to 10⁻¹¹ cm² s⁻¹. It is indicating that the faster diffusion coefficient of sodium ions could be revealed during cycling performance at larger current density. As shown in the **Figure 4.7**, rate performance within the P2 type cathode reveals that nearly 100 mAh g⁻¹ capacity can be achieved even at a larger current density of 200 mA g⁻¹. When the current density decreases from 200 mA g⁻¹ to 20 mA g⁻¹, the reversible capacity of about 120 mAh g⁻¹ can still be retained after 40 cycles at 20 mA g⁻¹, which suggests the excellent rate performance within the P2 type cathode.

4.3.4 Phase transition process within the P2 type layered oxide

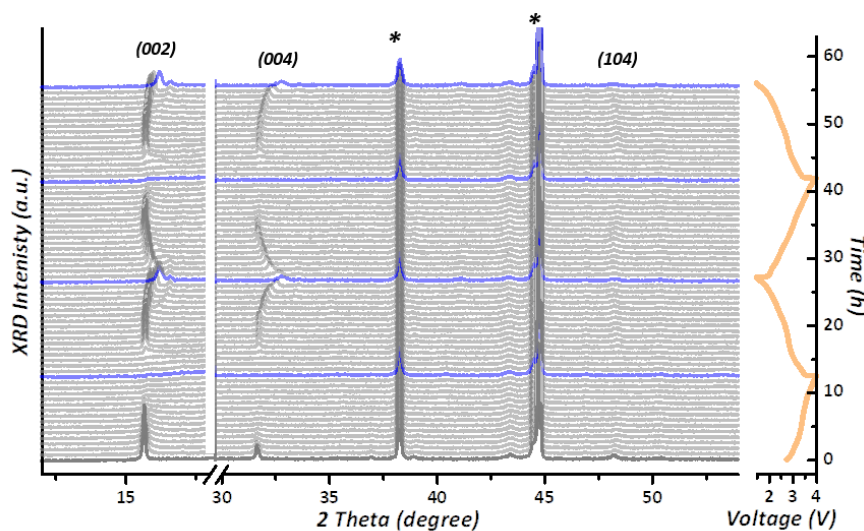


Figure 4. 8 Crystal structural evolution analysis by in-situ XRD. The collected XRD patterns of P2-NLFR cathodes over the initial two cycles at a rate of C/10.

To unravel the intercalation/deintercalation mechanism of sodium ion during the cycling process within the P2 type layered oxide NLFR, in-situ XRD is employed to

investigate the related phase transition process during the initial two cycles as shown in the **Figure 4.8**. In-situ XRD curves are collected with the corresponding voltage profile within the voltage range from 1.5 to 4V.

Upon the initial charging process, the 002 peak firstly shifts to the lower angle and it suggests that the interlayer distance increase.¹⁴⁷ Along with the desodiation process, the related 002 reflection shifts to the higher angle accompanied by the h00 and h0l peaks shift to higher angles continuously. Along with the subsequent charging, it could be observed that Z phase occurs as a single phase which is highly broadened of the high voltage range based on the previous reports.¹⁴³ During the subsequent discharging for the initial cycle, Z phase is well maintained at the beginning stage. Then single Z phase transforms to single P2 phase without appearance of other notable new phases. =

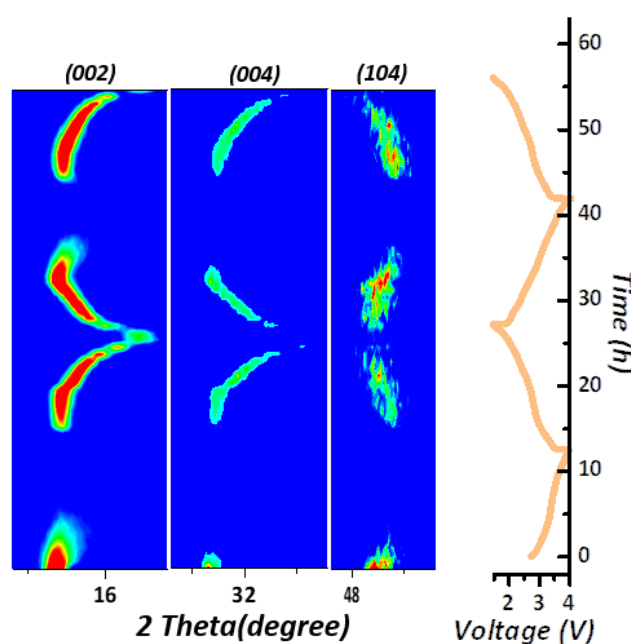


Figure 4. 9 The structure evolution of P2-NLFR and related color graph for (002) (004) and (104) reflections during first two cycles.

However, at the latter stage of the first discharging process, a small new peak appears with splitting of the 002 peak. And the small new peak can be rationally attributed to the P'2 phase belonging to space group of Cmcm based on the previous papers. During

the second cycle, the P2 type layered oxide NLFR undergoes the similar phase transition process with the first cycle. The corresponding color graph of the structure evolution of 002, 004 and 104 reflections are shown in the **Figure 4.9**. It is worth noting that the similar variation tendency is presented for the shift of the characteristic peaks within the P2 type layered oxide NLFR.

4.3.5 Oxygen related anionic redox chemistry within the P2 type NLFR

In order to unravel the oxygen related anionic redox chemistry within the P2 type layered oxide NLFR, in-situ Raman is employed to detect the oxygen behaviors, which is regarded as the powerful tool. The detail analysis results has been provided in the **Figure 4.10**. During the first charging process, the novel peaks located at 825 cm^{-1} are rationally ascribed to the peroxo-related O-O stretch.¹⁴⁸ In addition, the specific peak shifts to the positive wavenumber at the end of the charging process, which is attributed to the gradual shortened O-O bond length of peroxo-related species. It is noteworthy that the specific peak turns back reversibly with shifting to the negative wavenumber during the subsequent discharging process.

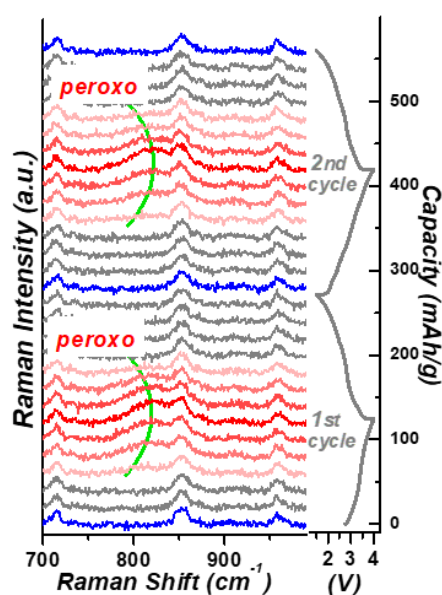


Figure 4. 10 The recorded capacity-dependent operando Raman patterns of P2-NLFR during first two

galvanostatic cycles at 0.1 C.

Furthermore, a similar evolution of the peroxo-related species can be observed upon the second galvanostatic charge discharge process within the P2 type layered oxide NLFR.

In order to further illustrate the charge compensation process of the P2 NLFR, XPS analysis is performed at various states of the electrode material. XPS spectra of Fe 2p and Ru 3d are presented in the **Figure 4.11**. It can be observed that the valence state of Fe, Ru are +3, +5 respectively within the pristine state of the P2 type layered oxide NLFR, according to the XPS spectra of Fe 2p and Ru 3d. During the first charging, Fe 2p spectra is observed with the positive shifting 0.35 eV of the binding energy, which is corresponding to the oxidation process from Fe^{3+} to Fe^{4+} . Meanwhile, the binding energy of Ru 3d spectra is observed without significant shift compared to the pristine state. It suggests that Ru makes no contribution to the charge compensation process during the first charging.

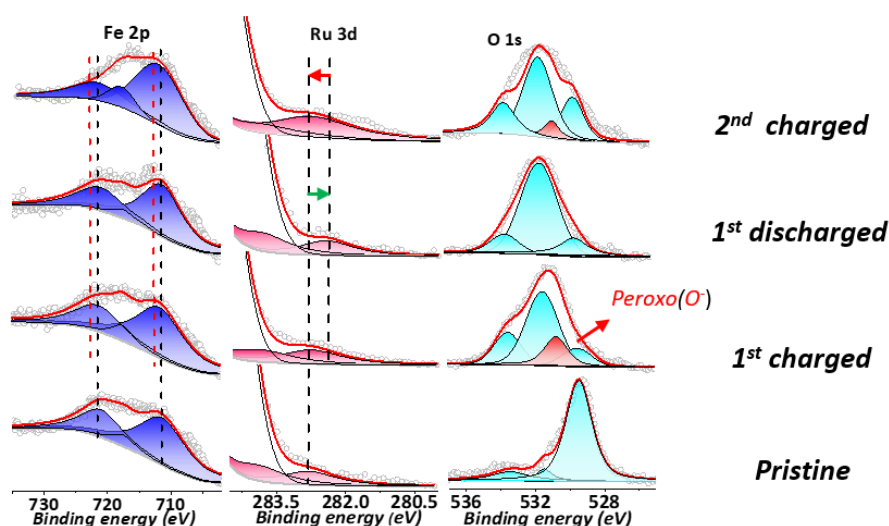


Figure 4. 11 XPS spectra of Fe 2p, Ru 3d and O 1s for P2-NLFR with the pristine state, the samples charged to 4 V, discharged to 1.5 V and 2nd charged to 4 V from bottom to top.

Furthermore, a novel peak is observed from the O 1s spectra at 530.7 eV, which can be rationally ascribed to the existence of the peroxo-related species. Fully discharged

state of the Fe 2p and Ru 3d spectra are performed in the figure and the both shift to the negative binding energy, which are corresponding to the reduction process of Fe^{3+} and Ru^{5+} respectively. In addition, the O 1s spectra show that the negative shift within the XPS spectra, demonstrating the reversible redox activity of oxygen from O^- to O^{2-} . More importantly, the reversible oxygen related anionic redox activity shows good consistent with the in-situ Raman results above. In another word, not only the cationic redox activity but also the anionic redox activity has been confirmed within the P2 type layered oxide NLFR.

The related operando DEMS has been employed to further confirm the corresponding anionic redox chemistry within the P2 type layered oxide NLFR, which is shown in the **Figure 4.12**. The oxygen related anionic redox chemistry has been confirmed by the in-situ Raman results combined with the XPS data within the P2 type layered oxide NLFR. Moreover, the anionic redox activity could be triggered within 4V cut-off voltage. It is worth noting that scarcely any O_2 or CO_2 could be detected as expected from the gas evolution information based on the DEMS results. It shows the good consistent with the peroxo-related stretching mode from the in-situ Raman spectra, which could further confirm the reversible oxygen related anionic redox behavior. Simultaneously, the reversible O^{2-}/O^- oxygen behavior is the dominated part within the electrochemical performance process based on the solid evidence from operando characterization techniques.

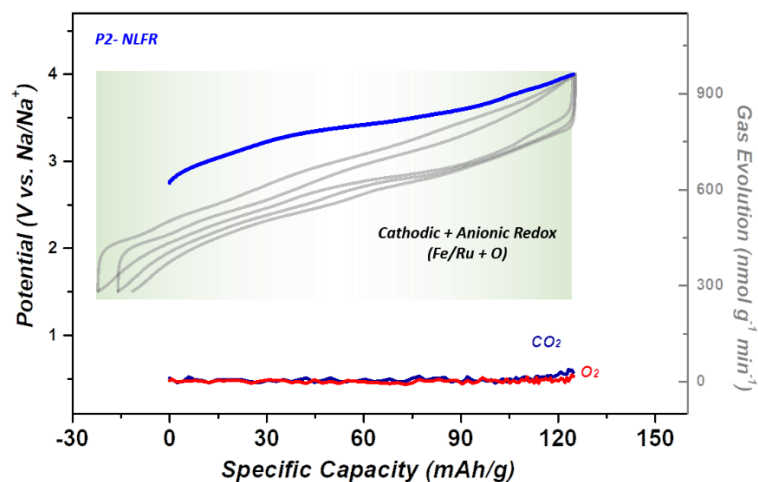


Figure 4. 12 Analysis on oxygen behaviors. In-situ DEMS results of gas evolution rates for CO₂ and O₂ on P2-NLFR cathode over the initial cycle at a rate of 0.1 C.

4.4 Summary

The corresponding charge compensation process within the P2 type layered oxide NLFR has been exhibited by the systematic characterization analysis. The electrochemical activity of cationic redox and anionic redox has been verified by the XPS spectra and in-situ Raman technique. In this case, the reversible oxygen related anionic redox activity is easy to be triggered within the conducting cut-off voltage 4V. Our findings provide new insights into underlying structural impact on oxygen related anionic redox chemistry and trigger a rational design perspective to develop advanced high energy density cathodes.

Chapter 5. General Conclusion and perspective

5.1 General conclusion

The layered oxide compounds are considered as the promising candidates among numerous cathode materials for sodium ion batteries due to the simple structure and ease of synthesis. Moreover, the emergence of oxygen related anionic redox chemistry has been recently considered as a transformative approach for designing cathode materials due to the increasing specific energy capacities of cathodes. In this research work, we have investigated the anionic redox chemistry of three layered oxide cathodes based on the different layered structure and analyzed the related feasibility and corresponding electrochemical performance. The main conclusions are shown as follows:

In chapter 2, layered oxide $\text{NaMg}_{0.67}\text{Ru}_{0.33}\text{O}_2$ with O3 layered structure is synthesized and oxygen related anionic redox activity has been investigated. Oxygen related anionic redox chemistry has contributed to the charge compensation process within the O3-NMRO during the initial cycle. And the direct observation of the peroxo-related species from in-situ Raman is the solid confirmation for the oxygen behavior. In addition, the lattice oxygen evolution upon the first charging would facilitate the relative positive structural transformation and even cycle stability during long-term cycling. This discovery may stimulate us to keep the reversible anionic redox based on peroxo-related species probably.

In chapter 3, layered oxide $\text{Na}_{0.5}\text{Mg}_{0.15}\text{Al}_{0.2}\text{Mn}_{0.65}\text{O}_2$ with P3 layered structure is synthesized and anionic redox chemistry has been fundamentally unraveled. Here we prove an excellent structural stability via the operando/ex-situ structural evolution within this cathode, and further elucidate the complete anionic/cationic redox activity via both surface-sensitive (XPS) and bulk-sensitive (XAS) spectroscopies. Moreover,

based on the characterization of ex-situ state to the operando evolution for the whole anionic redox process by Raman and DEMS, the nature of the reversible oxygen redox chemistry is clarified. Meanwhile, the origin of a small portion irreversible oxygen release generated upon the first charging and its resulting impact on subsequent processes are also fully illuminated. These insights provide guidelines for future designing anionic redox-based high-energy-density cathodes in Lithium/Sodium-ion batteries.

In chapter 4, layered oxide $\text{Na}_{0.6}\text{Li}_{0.35}\text{Fe}_{0.1}\text{Ru}_{0.55}\text{O}_2$ with P2 layered structure is synthesized and related anionic redox chemistry has been identified. The anionic redox reaction induced oxygen behavior within the P2-NLFR is systematically investigated by various ex/in-situ spectroscopic characterizations. And the reversible oxygen behavior is easy to be triggered with the conducted cut-off voltage 4V. Moreover, the larger capacity and better cycling performance can be obtained attributed to the reversible oxygen behaviors.

5.2 Perspective

Oxygen related anionic redox chemistry within the layered oxide cathodes for sodium ion batteries has attracted intense interest due to the extra capacity and higher potential. Oxygen related anionic redox could be triggered by the special Na-O-TM (Li, Mg) configuration, and the concept can be adopted within the sodium rich materials due to the similar structure. The Na-O-Na configuration has been reported in the sodium rich materials as shown in the **Figure 5.1a-b**.^{109, 111} Furthermore, the similar feature has been revealed within the sodium rich materials and excess capacity has been exhibited due to activity of anionic redox reaction process. Thus, oxygen related anionic redox chemistry paves the novel avenue to develop high power density for sodium ion battery technology.

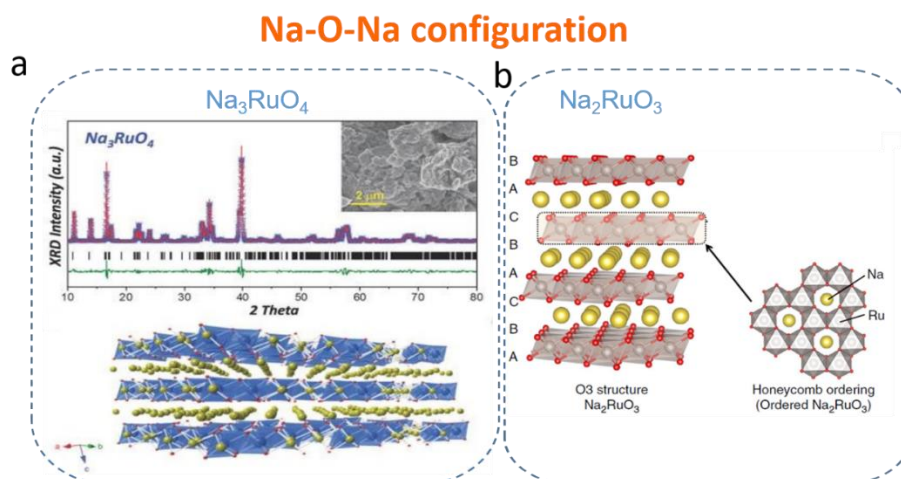


Figure 5. 1 Oxygen activation within sodium rich material due to Na-O-Na configuration: (a) Na_3RuO_4 .¹¹¹ (b) Na_2RuO_3 .¹⁰⁹ Copyright © 2018 ROYAL SOCIETY OF CHEMISTRY. Copyright © 2016, Springer Nature.

List of Publications

First author:

- (1) **Jia Min**, Qiao Yu, Li Xiang, Jiang Kezhu, and Zhou Haoshen*, Unraveling the anionic oxygen loss and related structural evolution within O3-type Na layered oxide cathodes. *J. Mater. Chem. A*, 2019, 7, 20405-20413.
- (2) **Jia Min**, Qiao Yu, Li Xiang, Qiu Feilong, Cao Xin, He Ping, Zhou Haoshen*, Identifying anionic redox activity within the related O3 and P2 type cathodes for sodium-ion battery, *ACS Applied Materials & Interfaces*, 2020, 12, 1, 851-857.
- (3) **Jia Min**, Li Haifeng, Qiao Yu, Wang Linlin, Cao Xin, Cabana Jordi and Zhou Haoshen*, Elucidating Anionic Redox Chemistry in P3-layered Cathode for Na-ion Batteries, *ACS Applied Materials & Interfaces*, *Accepted*.
(The first three papers are related to this Ph.D. thesis.)
- (4) **Jia Min**, Li Haifeng, Qiao Yu, Cao Xin, Cabana Jordi and Zhou Haoshen*, Reversible Anionic and cationic redox activity in compound: P2 type layered materials for sodium-ion batteries, **In preparation**.

Acknowledgements

This thesis not only represents the work at the keyboard, but also represents the three years of my research work. Since the first day I came to the city of Tsukuba, a new time period has been opened. Three years of study reveals the true meaning of research and I have benefited a lot. The completion of this thesis would not been possible without the support and encouragement of those who helped me, thus I would like to express my sincere gratitude towards them.

First and foremost, I would like to gratefully acknowledge the help of my doctoral supervisor Prof. Haoshen Zhou (a professor of University of Tsukuba and a principle investigator of National Institute of Advanced Industrial Science and Technology (AIST)) for his instructive advice and patient guidance. He would offer the insightful ideas and meaningful inspiration while I was confused during the research period. Without his dedicated assistance and expect guidance, my thesis could not be presented the current form. His conscientious academic spirit inspires me not only in the research study, but also for the daily life and he gives me much help during the whole research study of my doctoral period.

Secondly, I also deeply appreciate to my sub-supervisors at University of Tsukuba, Prof. Masayoshi Ishida and associate Prof. Hirohisa Aki. They always offer the selfless assistance and give me a hand when I need help. Moreover, very thanks to the valuable suggestions from Prof. Masayoshi Ishida, Associate Prof. Hirohisa Aki, Associate Prof. Takayasu Fujino and Dr. Hirokazu Kitaura in my presentation of graduation thesis, which makes the presentation improved significantly.

Thirdly, I would express the appreciation to all my group members: Dr. Yarong Wang, Dr. Qi Li, Dr. Shichao Wu, Dr. Yu Qiao, Dr. Xiang Li, Dr. Yibo He, Dr. Feilong Qiu, Dr. Linlin Wang, Prof. Jianan Zhang, Prof. Anqiang Pan, Mr. Han Deng, Mr. Zhi Chang, Mr. Xin Cao, Mr. Huijun Yang and Mr Xingyu Zhu. They gave me much help in study

and life. Particularly, I want to appreciate Dr. Qi Li, Dr. Yu Qiao and Dr. Xiang Li, since they gave me lots of valuable suggestions and kind help within my research work. I also want to thank Dr. Yarong Wang, she always wakes me up when I am confused and would encourage me when frustrated. Furthermore, many thanks to the help from my classmates: Mr. Zhi Chang and Mr. Han Deng. We entered the University of Tsukuba together and they helped me a lot during my study and daily life.

My appreciation also goes to the group members in Energy Interface Technology Group of National Institute of Advanced Industrial Science and Technology: Dr Hirofumi Matsuda, Dr. Eunjoo Yoo, Dr. Hirokazu Kitaura, Mr. Jun Okagaki and Okita-san. They always offer me help when I have difficulty in my research work and take care of me for the daily life.

Then, I'm extremely grateful for the financial support provided by the China Scholarship Council, which could make me focus on my research work.

Besides, I would like to express my thanks to the friends who have been helping me for my life: Xingxing Zhou, Maolin Wang, Debei Liu, Bolei Shen, Huan Wei, Kewei Sun, Wei Gao, Wenjun Li, Fenxing Hou, Ting Liu, Xiaoying Si and so on. When I need help, they are always there.

I would like to express my special thanks to my beloved parents, Bucheng Jia and Cuihua Chai, for their continuous support and loving considerations, which make me have the courage to keep moving on the path of life. Thanks to my sister Li Jia, my brother Quan Jia, who always support me and stay with me all the time.

Lastly, I want to say thanks to myself. Thank you for being on the way, not giving up. Heart's desire, omnipotent.

Reference

1. Armand, M.; Tarascon, J. M., Building better batteries. *Nature* **2008**, *451* (7179), 652-657.
2. Arico, A. S.; Bruce, P.; Scrosati, B.; Tarascon, J. M.; Van Schalkwijk, W., Nanostructured materials for advanced energy conversion and storage devices. *Nature Materials* **2005**, *4* (5), 366-377.
3. Liu, C.; Li, F.; Ma, L. P.; Cheng, H. M., Advanced Materials for Energy Storage. *Advanced materials* **2010**, *22* (8), E28-E62.
4. Dunn, B.; Kamath, H.; Tarascon, J. M., Electrical Energy Storage for the Grid: A Battery of Choices. *Science* **2011**, *334* (6058), 928-935.
5. Scrosati, B.; Garche, J., Lithium batteries: Status, prospects and future. *Journal of Power Sources* **2010**, *195* (9), 2419-2430.
6. Jiang, J.; Li, Y. Y.; Liu, J. P.; Huang, X. T.; Yuan, C. Z.; Lou, X. W., Recent Advances in Metal Oxide-based Electrode Architecture Design for Electrochemical Energy Storage. *Advanced materials* **2012**, *24* (38), 5166-5180.
7. Valtchev, V.; Van den Bossche, A.; Ghijselen, J.; Melkebeek, J., Autonomous renewable energy conversion system. *Renewable Energy* **2000**, *19* (1-2), 259-275.
8. Spee, R.; Bhowmik, S.; Enslin, J. H. R., Novel control strategies for variable-speed doubly fed wind power generation systems. *Renewable Energy* **1995**, *6* (8), 907-915.
9. Mohamed, A. Z.; Eskander, M. N.; Ghali, F. A., Fuzzy logic control based maximum power tracking of a wind energy system. *Renewable Energy* **2001**, *23* (2), 235-245.
10. De Broe, A. M.; Drouilhet, S.; Gevorgian, V., A peak power tracker for small wind turbines in battery charging applications. *Ieee Transactions on Energy Conversion* **1999**, *14* (4), 1630-1635.
11. Koutroulis, E.; Kalaitzakis, K., Design of a maximum power tracking system for

wind-energy-conversion applications. *IEEE Trans. Ind. Electron.* **2006**, 53 (2), 486-494.

12. Laks, J. H.; Pao, L. Y.; Wright, A. D.; Ieee, Control of Wind Turbines: Past, Present, and Future. In *2009 American Control Conference, Vols 1-9*, Ieee: New York, 2009; pp 2096-2103.

13. Kazmi, S. M. R.; Goto, H.; Guo, H. J.; Ichinokura, O., A Novel Algorithm for Fast and Efficient Speed-Sensorless Maximum Power Point Tracking in Wind Energy Conversion Systems. *IEEE Trans. Ind. Electron.* **2011**, 58 (1), 29-36.

14. Dasgupta, S.; Sahoo, S. K.; Panda, S. K., Single-Phase Inverter Control Techniques for Interfacing Renewable Energy Sources With Microgrid-Part I: Parallel-Connected Inverter Topology With Active and Reactive Power Flow Control Along With Grid Current Shaping. *IEEE Trans. Power Electron.* **2011**, 26 (3), 717-731.

15. Yaramasu, V.; Wu, B.; Sen, P. C.; Kouro, S.; Narimani, M., High-Power Wind Energy Conversion Systems: State-of-the-Art and Emerging Technologies. *Proc. IEEE* **2015**, 103 (5), 740-788.

16. Frackowiak, E.; Beguin, F., Carbon materials for the electrochemical storage of energy in capacitors. *Carbon* **2001**, 39 (6), 937-950.

17. Bonnefoi, L.; Simon, P.; Fauvarque, J. F.; Sarrazin, C.; Dugast, A., Electrode optimisation for carbon power supercapacitors. *Journal of Power Sources* **1999**, 79 (1), 37-42.

18. Bonnefoi, L.; Simon, P.; Fauvarque, J. F.; Sarrazin, C.; Sarrau, J. F.; Dugast, A., Electrode compositions for carbon power supercapacitors. *Journal of Power Sources* **1999**, 80 (1-2), 149-155.

19. Conway, B. E., TRANSITION FROM SUPERCAPACITOR TO BATTERY BEHAVIOR IN ELECTROCHEMICAL ENERGY-STORAGE. *Journal of the Electrochemical Society* **1991**, 138 (6), 1539-1548.

20. Kim, S. W.; Seo, D. H.; Ma, X. H.; Ceder, G.; Kang, K., Electrode Materials for

Rechargeable Sodium-Ion Batteries: Potential Alternatives to Current Lithium-Ion Batteries. *Advanced Energy Materials* **2012**, 2 (7), 710-721.

21. Cabana, J.; Monconduit, L.; Larcher, D.; Palacin, M. R., Beyond Intercalation-Based Li-Ion Batteries: The State of the Art and Challenges of Electrode Materials Reacting Through Conversion Reactions. *Advanced materials* **2010**, 22 (35), E170-E192.

22. Suo, L. M.; Hu, Y. S.; Li, H.; Armand, M.; Chen, L. Q., A new class of Solvent-in-Salt electrolyte for high-energy rechargeable metallic lithium batteries. *Nature Communications* **2013**, 4, 1481.

23. Wu, H.; Cui, Y., Designing nanostructured Si anodes for high energy lithium ion batteries. *Nano Today* **2012**, 7 (5), 414-429.

24. Liu, N.; Wu, H.; McDowell, M. T.; Yao, Y.; Wang, C. M.; Cui, Y., A Yolk-Shell Design for Stabilized and Scalable Li-Ion Battery Alloy Anodes. *Nano letters* **2012**, 12 (6), 3315-3321.

25. Stevens, D. A.; Dahn, J. R., The mechanisms of lithium and sodium insertion in carbon materials. *Journal of the Electrochemical Society* **2001**, 148 (8), A803-A811.

26. Stevens, D. A.; Dahn, J. R., High capacity anode materials for rechargeable sodium-ion batteries. *Journal of the Electrochemical Society* **2000**, 147 (4), 1271-1273.

27. David, L.; Bhandavat, R.; Singh, G., MoS₂/Graphene Composite Paper for Sodium-Ion Battery Electrodes. *ACS Nano* **2014**, 8 (2), 1759-1770.

28. Kundu, D.; Talaie, E.; Duffort, V.; Nazar, L. F., The Emerging Chemistry of Sodium Ion Batteries for Electrochemical Energy Storage. *Angewandte Chemie International Edition* **2015**, 54 (11), 3431-3448.

29. Yabuuchi, N.; Kubota, K.; Dahbi, M.; Komaba, S., Research Development on Sodium-Ion Batteries. *Chem Rev* **2014**, 114 (23), 11636-11682.

30. Slater, M. D.; Kim, D.; Lee, E.; Johnson, C. S., Sodium-Ion Batteries. *Advanced*

Functional Materials **2013**, 23 (8), 947-958.

31. Cheng, F. Y.; Liang, J.; Tao, Z. L.; Chen, J., Functional Materials for Rechargeable Batteries. *Advanced materials* **2011**, 23 (15), 1695-1715.

32. Hwang, J. Y.; Myung, S. T.; Sun, Y. K., Sodium-ion batteries: present and future. *Chemical Society reviews* **2017**, 46 (12), 3529-3614.

33. Ellis, B. L.; Nazar, L. F., Sodium and sodium-ion energy storage batteries. *Curr. Opin. Solid State Mat. Sci.* **2012**, 16 (4), 168-177.

34. Ong, S. P.; Chevrier, V. L.; Hautier, G.; Jain, A.; Moore, C.; Kim, S.; Ma, X. H.; Ceder, G., Voltage, stability and diffusion barrier differences between sodium-ion and lithium-ion intercalation materials. *Energy & Environmental Science* **2011**, 4 (9), 3680-3688.

35. Palomares, V.; Casas-Cabanas, M.; Castillo-Martinez, E.; Han, M. H.; Rojo, T., Update on Na-based battery materials. A growing research path. *Energy & Environmental Science* **2013**, 6 (8), 2312-2337.

36. Palomares, V.; Serras, P.; Villaluenga, I.; Hueso, K. B.; Carretero-Gonzalez, J.; Rojo, T., Na-ion batteries, recent advances and present challenges to become low cost energy storage systems. *Energy & Environmental Science* **2012**, 5 (3), 5884-5901.

37. Pan, H. L.; Hu, Y. S.; Chen, L. Q., Room-temperature stationary sodium-ion batteries for large-scale electric energy storage. *Energy & Environmental Science* **2013**, 6 (8), 2338-2360.

38. Cao, Y. L.; Xiao, L. F.; Sushko, M. L.; Wang, W.; Schwenzer, B.; Xiao, J.; Nie, Z. M.; Saraf, L. V.; Yang, Z. G.; Liu, J., Sodium Ion Insertion in Hollow Carbon Nanowires for Battery Applications. *Nano letters* **2012**, 12 (7), 3783-3787.

39. Chen, C. J.; Wen, Y. W.; Hu, X. L.; Ji, X. L.; Yan, M. Y.; Mai, L. Q.; Hu, P.; Shan, B.; Huang, Y. H., Na⁺ intercalation pseudocapacitance in graphene-coupled titanium oxide enabling ultra-fast sodium storage and long-term cycling. *Nature*

Communications **2015**, *6*, 6929.

40. Wen, Y.; He, K.; Zhu, Y. J.; Han, F. D.; Xu, Y. H.; Matsuda, I.; Ishii, Y.; Cumings, J.; Wang, C. S., Expanded graphite as superior anode for sodium-ion batteries. *Nature Communications* **2014**, *5*, 4033.

41. Sun, J.; Lee, H. W.; Pasta, M.; Yuan, H. T.; Zheng, G. Y.; Sun, Y. M.; Li, Y. Z.; Cui, Y., A phosphorene-graphene hybrid material as a high-capacity anode for sodium-ion batteries. *Nat. Nanotechnol.* **2015**, *10* (11), 980-U184.

42. Luo, W.; Shen, F.; Bommier, C.; Zhu, H. L.; Ji, X. L.; Hu, L. B., Na-Ion Battery Anodes: Materials and Electrochemistry. *Accounts of Chemical Research* **2016**, *49* (2), 231-240.

43. Komaba, S.; Takei, C.; Nakayama, T.; Ogata, A.; Yabuuchi, N., Electrochemical intercalation activity of layered NaCrO₂ vs. LiCrO₂. *Electrochemistry Communications* **2010**, *12* (3), 355-358.

44. Xiang, X. D.; Zhang, K.; Chen, J., Recent Advances and Prospects of Cathode Materials for Sodium-Ion Batteries. *Advanced materials* **2015**, *27* (36), 5343-5364.

45. Komaba, S.; Yabuuchi, N.; Nakayama, T.; Ogata, A.; Ishikawa, T.; Nakai, I., Study on the Reversible Electrode Reaction of Na_{1-x}Ni_{0.5}Mn_{0.5}O₂ for a Rechargeable Sodium-Ion Battery. *Inorganic Chemistry* **2012**, *51* (11), 6211-6220.

46. Wang, Y. S.; Yu, X. Q.; Xu, S. Y.; Bai, J. M.; Xiao, R. J.; Hu, Y. S.; Li, H.; Yang, X. Q.; Chen, L. Q.; Huang, X. J., A zero-strain layered metal oxide as the negative electrode for long-life sodium-ion batteries. *Nature Communications* **2013**, *4*, 7.

47. Yi, H. M.; Lin, L.; Ling, M. X.; Lv, Z. Q.; Li, R.; Fu, Q.; Zhang, H. M.; Zheng, Q.; Li, X. F., Scalable and Economic Synthesis of High-Performance Na₃V₂(PO₄)₂F₃ by a Solvothermal-Ball-Milling Method. *Acs Energy Letters* **2019**, *4* (7), 1565-1571.

48. Song, T. Y.; Yao, W. J.; Kiadkhunthod, P.; Zheng, Y. P.; Wu, N. Z.; Zhou, X. L.; Tunmee, S.; Sattayaporn, S.; Tang, Y. B., A Low-Cost and Environmentally Friendly

Mixed Polyanionic Cathode for Sodium-Ion Storage. *Angew. Chem.-Int. Edit.* **2020**, *59* (2), 740-745.

49. Zhu, C. B.; Wu, C.; Chen, C. C.; Kopold, P.; van Aken, P. A.; Maier, J.; Yu, Y., A High Power-High Energy $\text{Na}_3\text{V}_2(\text{PO}_4)_2\text{F}_3$ Sodium Cathode: Investigation of Transport Parameters, Rational Design and Realization. *Chemistry of Materials* **2017**, *29* (12), 5207-5215.

50. Deng, L.; Sun, G.; Goh, K.; Zheng, L. L.; Yu, F. D.; Sui, X. L.; Zhao, L.; Wang, Z. B., Facile one-step carbothermal reduction synthesis of $\text{Na}_3\text{V}_2(\text{PO}_4)_2\text{F}_3/\text{C}$ serving as cathode for sodium ion batteries. *Electrochimica Acta* **2019**, *298*, 459-467.

51. Kovrugin, V. M.; David, R.; Chotard, J. N.; Recham, N.; Masquelier, C., A High Voltage Cathode Material for Sodium Batteries: $\text{Na}_3\text{V}(\text{PO}_4)_2$. *Inorganic Chemistry* **2018**, *57* (15), 8760-8768.

52. Ding, J.; Wang, H. L.; Li, Z.; Kohandehghan, A.; Cui, K.; Xu, Z. W.; Zehri, B.; Tan, X. H.; Lotfabad, E. M.; Olsen, B. C.; Mitlin, D., Carbon Nanosheet Frameworks Derived from Peat Moss as High Performance Sodium Ion Battery Anodes. *ACS Nano* **2013**, *7* (12), 11004-11015.

53. Hou, H. S.; Banks, C. E.; Jing, M. J.; Zhang, Y.; Ji, X. B., Carbon Quantum Dots and Their Derivative 3D Porous Carbon Frameworks for Sodium-Ion Batteries with Ultralong Cycle Life. *Advanced materials* **2015**, *27* (47), 7861-7866.

54. Xu, J. T.; Wang, M.; Wickramaratne, N. P.; Jaroniec, M.; Dou, S. X.; Dai, L. M., High-Performance Sodium Ion Batteries Based on a 3D Anode from Nitrogen-Doped Graphene Foams. *Advanced materials* **2015**, *27* (12), 2042-2048.

55. Fu, S. D.; Ni, J. F.; Xu, Y.; Zhang, Q.; Li, L., Hydrogenation Driven Conductive $\text{Na}_2\text{Ti}_3\text{O}_7$ Nanoarrays as Robust Binder-Free Anodes for Sodium-Ion Batteries. *Nano letters* **2016**, *16* (7), 4544-4551.

56. Dong, S. Y.; Shen, L. F.; Li, H. S.; Pang, G.; Dou, H.; Zhang, X. G., Flexible

Sodium-Ion Pseudocapacitors Based on 3D Na₂Ti₃O₇ Nanosheet Arrays/Carbon Textiles Anodes. *Advanced Functional Materials* **2016**, 26 (21), 3703-3710.

57. Senguttuvan, P.; Rousse, G.; Seznec, V.; Tarascon, J. M.; Palacin, M. R., Na₂Ti₃O₇: Lowest Voltage Ever Reported Oxide Insertion Electrode for Sodium Ion Batteries. *Chemistry of Materials* **2011**, 23 (18), 4109-4111.

58. Pan, H. L.; Lu, X.; Yu, X. Q.; Hu, Y. S.; Li, H.; Yang, X. Q.; Chen, L. Q., Sodium Storage and Transport Properties in Layered Na₂Ti₃O₇ for Room-Temperature Sodium-Ion Batteries. *Advanced Energy Materials* **2013**, 3 (9), 1186-1194.

59. Rudola, A.; Saravanan, K.; Mason, C. W.; Balaya, P., Na₂Ti₃O₇: an intercalation based anode for sodium-ion battery applications. *Journal of Materials Chemistry A* **2013**, 1 (7), 2653-2662.

60. Irisarri, E.; Ponrouch, A.; Palacin, M. R., Review-Hard Carbon Negative Electrode Materials for Sodium-Ion Batteries. *Journal of the Electrochemical Society* **2015**, 162 (14), A2476-A2482.

61. Chevrier, V. L.; Ceder, G., Challenges for Na-ion Negative Electrodes. *Journal of the Electrochemical Society* **2011**, 158 (9), A1011-A1014.

62. Komaba, S.; Murata, W.; Ishikawa, T.; Yabuuchi, N.; Ozeki, T.; Nakayama, T.; Ogata, A.; Gotoh, K.; Fujiwara, K., Electrochemical Na Insertion and Solid Electrolyte Interphase for Hard-Carbon Electrodes and Application to Na-Ion Batteries. *Advanced Functional Materials* **2011**, 21 (20), 3859-3867.

63. Jian, Z. L.; Xing, Z. Y.; Bommier, C.; Li, Z. F.; Ji, X. L., Hard Carbon Microspheres: Potassium-Ion Anode Versus Sodium-Ion Anode. *Advanced Energy Materials* **2016**, 6 (3), 5.

64. Bommier, C.; Ji, X. L., Electrolytes, SEI Formation, and Binders: A Review of Nonelectrode Factors for Sodium-Ion Battery Anodes. *Small* **2018**, 14 (16), 20.

65. Munoz-Marquez, M. A.; Saurel, D.; Gomez-Camer, J. L.; Casas-Cabanas, M.;

Castillo-Martinez, E.; Rojo, T., Na-Ion Batteries for Large Scale Applications: A Review on Anode Materials and Solid Electrolyte Interphase Formation. *Advanced Energy Materials* **2017**, 7 (20), 31.

66. Wang, M.; Tang, Y. B., A Review on the Features and Progress of Dual-Ion Batteries. *Advanced Energy Materials* **2018**, 8 (19), 20.

67. Yabuuchi, N.; Komaba, S., Recent research progress on iron- and manganese-based positive electrode materials for rechargeable sodium batteries. *Sci. Technol. Adv. Mater.* **2014**, 15 (4), 29.

68. Skundin, A. M.; Kulova, T. L.; Yaroslavtsev, A. B., Sodium-Ion Batteries (a Review). *Russ. J. Electrochem.* **2018**, 54 (2), 113-152.

69. Cao, C. Y.; Liu, W. W.; Tan, L.; Liao, X. Z.; Li, L., Sodium-ion batteries using ion exchange membranes as electrolytes and separators. *Chemical Communications* **2013**, 49 (100), 11740-11742.

70. Jang, J. Y.; Kim, H.; Lee, Y.; Lee, K. T.; Kang, K.; Choi, N. S., Cyclic carbonate based-electrolytes enhancing the electrochemical performance of $\text{Na}_4\text{Fe}_3(\text{PO}_4)_2(\text{P}_2\text{O}_7)$ cathodes for sodium-ion batteries. *Electrochemistry Communications* **2014**, 44, 74-77.

71. Che, H. Y.; Chen, S. L.; Xie, Y. Y.; Wang, H.; Amine, K.; Liao, X. Z.; Ma, Z. F., Electrolyte design strategies and research progress for room-temperature sodium-ion batteries. *Energy & Environmental Science* **2017**, 10 (5), 1075-1101.

72. Vignarooban, K.; Kushagra, R.; Elango, A.; Badami, P.; Mellander, B. E.; Xu, X.; Tucker, T. G.; Nam, C.; Kannan, A. M., Current trends and future challenges of electrolytes for sodium-ion batteries. *Int. J. Hydrog. Energy* **2016**, 41 (4), 2829-2846.

73. Zhang, J. Y.; Yao, X. H.; Misra, R. K.; Cai, Q.; Zhao, Y. L., Progress in electrolytes for beyond-lithium-ion batteries. *J. Mater. Sci. Technol.* **2020**, 44, 237-257.

74. Pan, H.; Hu, Y.-S.; Chen, L., Room-temperature stationary sodium-ion batteries for

large-scale electric energy storage. *Energy & Environmental Science* **2013**, 6 (8), 2338-2360.

75. Xie, M.; Luo, R.; Lu, J.; Chen, R. J.; Wu, F.; Wang, X. M.; Zhan, C.; Wu, H. M.; Albishri, H. M.; Al-Bogami, A. S.; Abd El-Hady, D.; Amine, K., Synthesis-Microstructure-Performance Relationship of Layered Transition Metal Oxides as Cathode for Rechargeable Sodium Batteries Prepared by High-Temperature Calcination. *ACS applied materials & interfaces* **2014**, 6 (19), 17176-17183.

76. Kubota, K.; Kumakura, S.; Yoda, Y.; Kuroki, K.; Komaba, S., Electrochemistry and Solid-State Chemistry of NaMeO₂ (Me=3d Transition Metals). *Advanced Energy Materials* **2018**, 8 (17), 40.

77. Wang, P. F.; You, Y.; Yin, Y. X.; Guo, Y. G., Layered Oxide Cathodes for Sodium-Ion Batteries: Phase Transition, Air Stability, and Performance. *Advanced Energy Materials* **2018**, 8 (8), 23.

78. Guo, S. H.; Zhou, H. S., High-energy Mn-based layered cathodes for sodium-ion batteries. *Sci. Bull.* **2019**, 64 (3), 149-150.

79. Han, M. H.; Gonzalo, E.; Singh, G.; Rojo, T., A comprehensive review of sodium layered oxides: powerful cathodes for Na-ion batteries. *Energy & Environmental Science* **2015**, 8 (1), 81-102.

80. Mo, Y. F.; Ong, S. P.; Ceder, G., Insights into Diffusion Mechanisms in P2 Layered Oxide Materials by First-Principles Calculations. *Chemistry of Materials* **2014**, 26 (18), 5208-5214.

81. Lee, D. H.; Xu, J.; Meng, Y. S., An advanced cathode for Na-ion batteries with high rate and excellent structural stability. *Phys. Chem. Chem. Phys.* **2013**, 15 (9), 3304-3312.

82. Okoshi, M.; Yamada, Y.; Yamada, A.; Nakai, H., Theoretical Analysis on De-Solvation of Lithium, Sodium, and Magnesium Cations to Organic Electrolyte Solvents.

Journal of the Electrochemical Society **2013**, *160* (11), A2160-A2165.

83. Delmas, C.; Maazaz, A.; Fouassier, C.; Réau, J.-M.; Hagenmuller, P., Influence de l'environnement de l'ion alcalin sur sa mobilité dans les structures à feuillets $Ax(LxM_{1-x})O_2$. *Materials Research Bulletin* **1979**, *14* (3), 329-335.

84. Yoshida, H.; Yabuuchi, N.; Komaba, S., $NaFe_{0.5}Co_{0.5}O_2$ as high energy and power positive electrode for Na-ion batteries. *Electrochemistry Communications* **2013**, *34*, 60-63.

85. Shacklette, L. W., Rechargeable Electrodes from Sodium Cobalt Bronzes. *Journal of The Electrochemical Society* **1988**, *135* (11), 2669.

86. Kim, D. K.; Muralidharan, P.; Lee, H.-W.; Ruffo, R.; Yang, Y.; Chan, C. K.; Peng, H.; Huggins, R. A.; Cui, Y., Spinel $LiMn_2O_4$ Nanorods as Lithium Ion Battery Cathodes. *Nano letters* **2008**, *8* (11), 3948-3952.

87. Rouxel, J., Anion–Cation Redox Competition and the Formation of New Compounds in Highly Covalent Systems. *Chemistry – A European Journal* **1996**, *2* (9), 1053-1059.

88. Bichat, M. P.; Gillot, F.; Monconduit, L.; Favier, F.; Morcrette, M.; Lemoigno, F.; Doublet, M. L., Redox-Induced Structural Change in Anode Materials Based on Tetrahedral $(MPn_4)_x$ - Transition Metal Pnictides. *Chemistry of Materials* **2004**, *16* (6), 1002-1013.

89. Amatucci, G. G., $CoO_{[sub 2]}$, The End Member of the $Li_{[sub x]}CoO_{[sub 2]}$ Solid Solution. *Journal of The Electrochemical Society* **1996**, *143* (3), 1114.

90. Tarascon, J. M.; Vaughan, G.; Chabre, Y.; Seguin, L.; Anne, M.; Strobel, P.; Amatucci, G., In Situ Structural and Electrochemical Study of $Ni_{1-x}Co_xO_2$ Metastable Oxides Prepared by Soft Chemistry. *Journal of Solid State Chemistry* **1999**, *147* (1), 410-420.

91. Aydinol, M. K.; Kohan, A. F.; Ceder, G.; Cho, K.; Joannopoulos, J., Ab initio study

of lithium intercalation in metal oxides and metal dichalcogenides. *Physical Review B* **1997**, *56* (3), 1354-1365.

92. Ceder, G.; Chiang, Y. M.; Sadoway, D. R.; Aydinol, M. K.; Jang, Y. I.; Huang, B., Identification of cathode materials for lithium batteries guided by first-principles calculations. *Nature* **1998**, *392* (6677), 694-696.

93. Kalyani, P.; Chitra, S.; Mohan, T.; Gopukumar, S., Lithium metal rechargeable cells using Li_2MnO_3 as the positive electrode. *Journal of Power Sources* **1999**, *80* (1), 103-106.

94. Robertson, A. D.; Bruce, P. G., Mechanism of Electrochemical Activity in Li_2MnO_3 . *Chemistry of Materials* **2003**, *15* (10), 1984-1992.

95. Sathiya, M.; Ramesha, K.; Rousse, G.; Foix, D.; Gonbeau, D.; Prakash, A. S.; Doublet, M. L.; Hemalatha, K.; Tarascon, J. M., High Performance $\text{Li}_2\text{Ru}_{1-y}\text{Mn}_y\text{O}_3$ ($0.2 \leq y \leq 0.8$) Cathode Materials for Rechargeable Lithium-Ion Batteries: Their Understanding. *Chemistry of Materials* **2013**, *25* (7), 1121-1131.

96. Sathiya, M.; Rousse, G.; Ramesha, K.; Laisa, C. P.; Vezin, H.; Sougrati, M. T.; Doublet, M. L.; Foix, D.; Gonbeau, D.; Walker, W.; Prakash, A. S.; Ben Hassine, M.; Dupont, L.; Tarascon, J. M., Reversible anionic redox chemistry in high-capacity layered-oxide electrodes. *Nature Materials* **2013**, *12* (9), 827-835.

97. McCalla, E.; Abakumov, A. M.; Saubanère, M.; Foix, D.; Berg, E. J.; Rousse, G.; Doublet, M.-L.; Gonbeau, D.; Novák, P.; Van Tendeloo, G.; Dominko, R.; Tarascon, J.-M., Visualization of O-O peroxo-like dimers in high-capacity layered oxides for Li-ion batteries. *Science* **2015**, *350* (6267), 1516.

98. Maitra, U.; House, R. A.; Somerville, J. W.; Tapia-Ruiz, N.; Lozano, J. G.; Guerrini, N.; Hao, R.; Luo, K.; Jin, L.; Pérez-Osorio, M. A.; Massel, F.; Pickup, D. M.; Ramos, S.; Lu, X.; McNally, D. E.; Chadwick, A. V.; Giustino, F.; Schmitt, T.; Duda, L. C.; Roberts, M. R.; Bruce, P. G., Oxygen redox chemistry without excess alkali-metal ions

- in $\text{Na}_{2/3}[\text{Mg}_{0.28}\text{Mn}_{0.72}]\text{O}_2$. *Nature Chemistry* **2018**, *10* (3), 288-295.
99. Maitra, U.; House, R. A.; Somerville, J.; Tapia-Ruiz, N.; Lozano, J. G.; Guerrini, N.; Hao, R.; Luo, K.; Jin, L.; Perez-Osorio, M. A.; Massel, F.; Pickup, D. M.; Ramos, S.; Lu, X.; McNally, D. E.; Chadwick, A. V.; Giustino, F.; Schmitt, T.; Duda, L. C.; Roberts, M. R.; Bruce, P. G., Oxygen redox chemistry without excess alkali-metal ions in $\text{Na}_{2/3}\text{Mg}_{0.28}\text{Mn}_{0.72}\text{O}_2$. *Nature Chemistry* **2018**, *10* (3), 288-295.
100. Perez, A. J.; Jacquet, Q.; Batuk, D.; Iadecola, A.; Saubanère, M.; Rousse, G.; Larcher, D.; Vezin, H.; Doublet, M.-L.; Tarascon, J.-M., Approaching the limits of cationic and anionic electrochemical activity with the Li-rich layered rocksalt Li_3IrO_4 . *Nature Energy* **2017**, *2* (12), 954-962.
101. Hu, E.; Yu, X.; Lin, R.; Bi, X.; Lu, J.; Bak, S.; Nam, K.-W.; Xin, H. L.; Jaye, C.; Fischer, D. A.; Amine, K.; Yang, X.-Q., Evolution of redox couples in Li- and Mn-rich cathode materials and mitigation of voltage fade by reducing oxygen release. *Nature Energy* **2018**, *3* (8), 690-698.
102. Grimaud, A.; Hong, W. T.; Shao-Horn, Y.; Tarascon, J. M., Anionic redox processes for electrochemical devices. *Nature Materials* **2016**, *15* (2), 121-126.
103. Kim, S.-W.; Seo, D.-H.; Ma, X.; Ceder, G.; Kang, K., Electrode Materials for Rechargeable Sodium-Ion Batteries: Potential Alternatives to Current Lithium-Ion Batteries. *Advanced Energy Materials* **2012**, *2* (7), 710-721.
104. Ma, C.; Alvarado, J.; Xu, J.; Clement, R. J.; Kodur, M.; Tong, W.; Grey, C. P.; Meng, Y. S., Exploring Oxygen Activity in the High Energy P2-Type $\text{Na}_{0.78}\text{Ni}_{0.23}\text{Mn}_{0.69}\text{O}_2$ Cathode Material for Na-Ion Batteries. *Journal of the American Chemical Society* **2017**, *139* (13), 4835-4845.
105. Kan, W. H.; Chen, D.; Papp, J. K.; Shukla, A. K.; Huq, A.; Brown, C. M.; McCloskey, B. D.; Chen, G., Unravelling Solid-State Redox Chemistry in $\text{Li}_{1.3}\text{Nb}_{0.3}\text{Mn}_{0.4}\text{O}_2$ Single-Crystal Cathode Material. *Chemistry of Materials* **2018**,

30 (5), 1655-1666.

106. McCalla, E.; Abakumov, A. M.; Saubanere, M.; Foix, D.; Berg, E. J.; Rousse, G.; Doublet, M.-L.; Gonbeau, D.; Novak, P.; Van Tendeloo, G.; Dominko, R.; Tarascon, J.-M., Visualization of O-O peroxo-like dimers in high-capacity layered oxides for Li-ion batteries. *Science* **2015**, *350* (6267), 1516-1521.

107. Teufl, T.; Strehle, B.; Mueller, P.; Gasteiger, H. A.; Mendez, M. A., Oxygen Release and Surface Degradation of Li- and Mn-Rich Layered Oxides in Variation of the Li_2MnO_3 Content. *Journal of the Electrochemical Society* **2018**, *165* (11), A2718-A2731.

108. Rong, X.; Hu, E.; Lu, Y.; Meng, F.; Zhao, C.; Wang, X.; Zhang, Q.; Yu, X.; Gu, L.; Hu, Y.-S.; Li, H.; Huang, X.; Yang, X.-Q.; Delmas, C.; Chen, L., Anionic Redox Reaction-Induced High-Capacity and Low-Strain Cathode with Suppressed Phase Transition. *Joule* **2019**, *3* (2), 503-517.

109. de Boisse, B. M.; Liu, G.; Ma, J.; Nishimura, S.-i.; Chung, S.-C.; Kiuchi, H.; Harada, Y.; Kikkawa, J.; Kobayashi, Y.; Okubo, M.; Yamada, A., Intermediate honeycomb ordering to trigger oxygen redox chemistry in layered battery electrode. *Nature Communications* **2016**, *7*, 11397.

110. Sathiyaraj, M.; Ramesha, K.; Rousse, G.; Foix, D.; Gonbeau, D.; Prakash, A. S.; Doublet, M. L.; Hemalatha, K.; Tarascon, J. M., High Performance $\text{Li}_2\text{Ru}_{1-y}\text{Mn}_y\text{O}_3$ ($0.2 \leq y \leq 0.8$) Cathode Materials for Rechargeable Lithium-Ion Batteries: Their Understanding. *Chemistry of Materials* **2013**, *25* (7), 1121-1131.

111. Qiao, Y.; Guo, S.; Zhu, K.; Liu, P.; Li, X.; Jiang, K.; Sun, C.-J.; Chen, M.; Zhou, H., Reversible anionic redox activity in Na_3RuO_4 cathodes: a prototype Na-rich layered oxide. *Energy & Environmental Science* **2018**, *11* (2), 299-305.

112. Peng, Z.; Freunberger, S. A.; Hardwick, L. J.; Chen, Y.; Giordani, V.; Barde, F.; Novak, P.; Graham, D.; Tarascon, J.-M.; Bruce, P. G., Oxygen Reactions in a Non-

Aqueous Li⁺ Electrolyte. *Angew. Chem.-Int. Edit.* **2011**, *50* (28), 6351-6355.

113.Freunberger, S. A.; Chen, Y.; Peng, Z.; Griffin, J. M.; Hardwick, L. J.; Barde, F.; Novak, P.; Bruce, P. G., Reactions in the Rechargeable Lithium-O₂ Battery with Alkyl Carbonate Electrolytes. *Journal of the American Chemical Society* **2011**, *133* (20), 8040-8047.

114.Gent, W. E.; Lim, K.; Liang, Y.; Li, Q.; Barnes, T.; Ahn, S.-J.; Stone, K. H.; McIntire, M.; Hong, J.; Song, J. H.; Li, Y.; Mehta, A.; Ermon, S.; Tyliszczak, T.; Kilcoyne, D.; Vine, D.; Park, J.-H.; Doo, S.-K.; Toney, M. F.; Yang, W.; Prendergast, D.; Chueh, W. C., Coupling between oxygen redox and cation migration explains unusual electrochemistry in lithium-rich layered oxides. *Nature Communications* **2017**, *8*, 2091.

115.Xu, J.; Sun, M.; Qiao, R.; Renfrew, S. E.; Ma, L.; Wu, T.; Hwang, S.; Nordlund, D.; Su, D.; Amine, K.; Lu, J.; McCloskey, B. D.; Yang, W.; Tong, W., Elucidating anionic oxygen activity in lithium-rich layered oxides. *Nature Communications* **2018**, *9*, 947.

116.Jung, S.-K.; Hwang, I.; Chang, D.; Park, K.-Y.; Kim, S. J.; Seong, W. M.; Eum, D.; Park, J.; Kim, B.; Kim, J.; Heo, J. H.; Kang, K., Nanoscale Phenomena in Lithium-Ion Batteries. *Chem Rev*, **2020**, *120*, 14, 6684–6737.

117.Yabuuchi, N.; Kubota, K.; Dahbi, M.; Komaba, S., Research Development on Sodium-Ion Batteries. *Chem Rev* **2014**, *114* (23), 11636-11682.

118.Peng, Z.; Freunberger, S. A.; Hardwick, L. J.; Chen, Y.; Giordani, V.; Bardé, F.; Novák, P.; Graham, D.; Tarascon, J.-M.; Bruce, P. G., Oxygen Reactions in a Non-Aqueous Li⁺ Electrolyte. *Angewandte Chemie International Edition* **2011**, *50* (28), 6351-6355.

119.Hwang, J.-Y.; Myung, S.-T.; Sun, Y.-K., Sodium-ion batteries: present and future. *Chemical Society reviews* **2017**, *46* (12), 3529-3614.

120. Bai, X.; Sathiya, M.; Mendoza - S á nchez, B.; Iadecola, A.; Vergnet, J.; Dedryvère, R.; Saubanière, M.; Abakumov, A. M.; Rozier, P.; Tarascon, J.-M., Anionic Redox Activity in a Newly Zn-Doped Sodium Layered Oxide $\text{P2-Na}_{2/3}\text{Mn}_{1-y}\text{Zn}_y\text{O}_2$ ($0 < y < 0.23$). *Advanced Energy Materials* **2018**, 8 (32), 1802379.
121. Cambaz, M. A.; Vinayan, B. P.; Geßwein, H.; Schiele, A.; Sarapulova, A.; Diemant, T.; Mazilkin, A.; Brezesinski, T.; Behm, R. J.; Ehrenberg, H.; Fichtner, M., Oxygen activity in Li-rich disordered rock-salt oxide and influence of LiNbO_3 surface modification on the electrochemical performance. *Chemistry of Materials* **2019**, 31, 12, 4330–4340.
122. de la Llave, E.; Talaie, E.; Levi, E.; Nayak, P. K.; Dixit, M.; Rao, P. T.; Hartmann, P.; Chesneau, F.; Major, D. T.; Greenstein, M.; Aurbach, D.; Nazar, L. F., Improving Energy Density and Structural Stability of Manganese Oxide Cathodes for Na-Ion Batteries by Structural Lithium Substitution. *Chemistry of Materials* **2016**, 28 (24), 9064-9076.
123. Sato, K.; Nakayama, M.; Glushenkov, A. M.; Mukai, T.; Hashimoto, Y.; Yamanaka, K.; Yoshimura, M.; Ohta, T.; Yabuuchi, N., Na-Excess Cation-Disordered Rocksalt Oxide: $\text{Na}_{1.3}\text{Nb}_{0.3}\text{Mn}_{0.4}\text{O}_2$. *Chemistry of Materials* **2017**, 29 (12), 5043-5047.
124. Qiao, Y.; Guo, S.; Zhu, K.; Liu, P.; Li, X.; Jiang, K.; Sun, C.-J.; Chen, M.; Zhou, H., Reversible anionic redox activity in Na_3RuO_4 cathodes: a prototype Na-rich layered oxide. *Energy & Environmental Science* **2018**, 11 (2), 299-305.
125. Rong, X.; Hu, E.; Lu, Y.; Meng, F.; Zhao, C.; Wang, X.; Zhang, Q.; Yu, X.; Gu, L.; Hu, Y.-S.; Li, H.; Huang, X.; Yang, X.-Q.; Delmas, C.; Chen, L., Anionic Redox Reaction-Induced High-Capacity and Low-Strain Cathode with Suppressed Phase Transition. *Joule* **2019**, 3 (2), 503-517.
126. Rong, X.; Liu, J.; Hu, E.; Liu, Y.; Wang, Y.; Wu, J.; Yu, X.; Page, K.; Hu, Y.-

- S.; Yang, W.; Li, H.; Yang, X.-Q.; Chen, L.; Huang, X., Structure-Induced Reversible Anionic Redox Activity in Na Layered Oxide Cathode. *Joule* **2018**, 2 (1), 125-140.
127. Maitra, U.; House, R. A.; Somerville, J. W.; Tapia-Ruiz, N.; Lozano, J. G.; Guerrini, N.; Hao, R.; Luo, K.; Jin, L.; Pérez-Osorio, M. A.; Massel, F.; Pickup, D. M.; Ramos, S.; Lu, X.; McNally, D. E.; Chadwick, A. V.; Giustino, F.; Schmitt, T.; Duda, L. C.; Roberts, M. R.; Bruce, P. G., Oxygen redox chemistry without excess alkali-metal ions in $\text{Na}_{2/3}[\text{Mg}_{0.28}\text{Mn}_{0.72}]\text{O}_2$. *Nature Chemistry* **2018**, 10 (3), 288-295.
128. Koga, H.; Croguennec, L.; Mannessiez, P.; Ménétrier, M.; Weill, F.; Bourgeois, L.; Duttine, M.; Suard, E.; Delmas, C., $\text{Li}_{1.20}\text{Mn}_{0.54}\text{Co}_{0.13}\text{Ni}_{0.13}\text{O}_2$ with Different Particle Sizes as Attractive Positive Electrode Materials for Lithium-Ion Batteries: Insights into Their Structure. *The Journal of Physical Chemistry C* **2012**, 116 (25), 13497-13506.
129. Armstrong, A. R.; Holzapfel, M.; Novák, P.; Johnson, C. S.; Kang, S.-H.; Thackeray, M. M.; Bruce, P. G., Demonstrating Oxygen Loss and Associated Structural Reorganization in the Lithium Battery Cathode $\text{Li}[\text{Ni}_{0.2}\text{Li}_{0.2}\text{Mn}_{0.6}]\text{O}_2$. *Journal of the American Chemical Society* **2006**, 128 (26), 8694-8698.
130. Chen, Z.; Li, J.; Zeng, X. C., Unraveling Oxygen Evolution in Li-Rich Oxides: A Unified Modeling of the Intermediate Peroxo/Superoxo-like Dimers. *Journal of the American Chemical Society* **2019**, 141, 27, 10751–10759.
131. Xu, J.; Lee, D. H.; Clément, R. J.; Yu, X.; Leskes, M.; Pell, A. J.; Pintacuda, G.; Yang, X.-Q.; Grey, C. P.; Meng, Y. S., Identifying the Critical Role of Li Substitution in $\text{P2-Na}_x[\text{Li}_y\text{Ni}_z\text{Mn}_{1-y-z}]\text{O}_2$ ($0 < x, y, z < 1$) Intercalation Cathode Materials for High-Energy Na-Ion Batteries. *Chemistry of Materials* **2014**, 26 (2), 1260-1269.
132. Foix, D.; Sathiya, M.; McCalla, E.; Tarascon, J.-M.; Gonbeau, D., X-ray Photoemission Spectroscopy Study of Cationic and Anionic Redox Processes in High-Capacity Li-Ion Battery Layered-Oxide Electrodes. *The Journal of Physical Chemistry*

C **2016**, 120 (2), 862-874.

133. Oishi, M.; Yamanaka, K.; Watanabe, I.; Shimoda, K.; Matsunaga, T.; Arai, H.; Ukyo, Y.; Uchimoto, Y.; Ogumi, Z.; Ohta, T., Direct observation of reversible oxygen anion redox reaction in Li-rich manganese oxide, Li_2MnO_3 , studied by soft X-ray absorption spectroscopy. *Journal of Materials Chemistry A* **2016**, 4 (23), 9293-9302.

134. Assat, G.; Iadecola, A.; Delacourt, C.; Dedryvère, R.; Tarascon, J.-M., Decoupling Cationic–Anionic Redox Processes in a Model Li-Rich Cathode via Operando X-ray Absorption Spectroscopy. *Chem. Mater.* **2017**, 29, 22, 9714–9724.

135. Luo, K.; Roberts, M. R.; Hao, R.; Guerrini, N.; Pickup, D. M.; Liu, Y.-S.; Edström, K.; Guo, J.; Chadwick, A. V.; Duda, L. C.; Bruce, P. G., - Charge-compensation in 3d-transition-metal-oxide intercalation cathodes through the generation of localized electron holes on oxygen. *Nature Chemistry*, **2016**, 8, 684-691.

136. Yoon, W.-S.; Balasubramanian, M.; Chung, K. Y.; Yang, X.-Q.; McBreen, J.; Grey, C. P.; Fischer, D. A., Investigation of the Charge Compensation Mechanism on the Electrochemically Li-Ion Deintercalated $\text{Li}_{1-x}\text{Co}_{1/3}\text{Ni}_{1/3}\text{Mn}_{1/3}\text{O}_2$ Electrode System by Combination of Soft and Hard X-ray Absorption Spectroscopy. *Journal of the American Chemical Society* **2005**, 127 (49), 17479-17487.

137. Oishi, M.; Yamanaka, K.; Watanabe, I.; Shimoda, K.; Matsunaga, T.; Arai, H.; Ukyo, Y.; Uchimoto, Y.; Ogumi, Z.; Ohta, T., Direct observation of reversible oxygen anion redox reaction in Li-rich manganese oxide, Li_2MnO_3 , studied by soft X-ray absorption spectroscopy. *Journal of Materials Chemistry A* **2016**, 4 (23), 9293-9302.

138. Johnson, L.; Li, C.; Liu, Z.; Chen, Y.; Freunberger, S. A.; Ashok, P. C.; Praveen, B. B.; Dholakia, K.; Tarascon, J.-M.; Bruce, P. G., The role of Li_2O solubility in O_2 reduction in aprotic solvents and its consequences for $\text{Li}-\text{O}_2$ batteries. *Nature Chemistry* **2014**, 6 (12), 1091-1099.

139. Nayak, P. K.; Yang, L.; Brehm, W.; Adelhelm, P., From Lithium-Ion to

Sodium-Ion Batteries: Advantages, Challenges, and Surprises. *Angew. Chem.-Int. Edit.* **2018**, *57* (1), 102-120.

140. Yang, Y.; Liu, X.; Dai, Z.; Yuan, F.; Bando, Y.; Golberg, D.; Wang, X., In Situ Electrochemistry of Rechargeable Battery Materials: Status Report and Perspectives. *Advanced materials* **2017**, *29* (31), 1606922.

141. Delmas, C., Sodium and Sodium-Ion Batteries: 50 Years of Research. *Advanced Energy Materials* **2018**, *8* (17), 1703137.

142. Hwang, J.-Y.; Myung, S.-T.; Sun, Y.-K., Sodium-ion batteries: present and future. *Chemical Society reviews* **2017**, *46* (12), 3529-3614.

143. Liu, L.; Li, X.; Bo, S.-H.; Wang, Y.; Chen, H.; Twu, N.; Wu, D.; Ceder, G., High-Performance P2-Type $\text{Na}_{2/3}(\text{Mn}_{1/2}\text{Fe}_{1/4}\text{Co}_{1/4})\text{O}_2$ Cathode Material with Superior Rate Capability for Na-Ion Batteries. *Advanced Energy Materials* **2015**, *5* (22).

144. Ben Yahia, M.; Vergnet, J.; Saubanere, M.; Doublet, M.-L., Unified picture of anionic redox in Li/Na-ion batteries. *Nature Materials* **2019**, *18* (5), 496–502.

145. Assat, G.; Tarascon, J.-M., Fundamental understanding and practical challenges of anionic redox activity in Li-ion batteries. *Nature Energy* **2018**, *3* (5), 373-386.

146. Perez, A. J.; Batuk, D.; Saubanere, M.; Rousse, G.; Foix, D.; McCalla, E.; Berg, E. J.; Dugas, R.; van den Bos, K. H. W.; Doublet, M.-L.; Gonbeau, D.; Abakumov, A. M.; Van Tendeloo, G.; Tarascon, J.-M., Strong Oxygen Participation in the Redox Governing the Structural and Electrochemical Properties of Na-Rich Layered Oxide Na_2IrO_3 . *Chemistry of Materials* **2016**, *28* (22), 8278-8288.

147. Li, Y.; Yang, Z.; Xu, S.; Mu, L.; Gu, L.; Hu, Y.-S.; Li, H.; Chen, L., Air-Stable Copper-Based P2- $\text{Na}_{7/9}\text{Cu}_{2/9}\text{Fe}_{1/9}\text{Mn}_{2/3}\text{O}_2$ as a New Positive Electrode Material for Sodium-Ion Batteries. *Advanced Science* **2015**, *2* (6), 1500031.

148. Johnson, L.; Li, C.; Liu, Z.; Chen, Y.; Freunberger, S. A.; Ashok, P. C.; Praveen,

B. B.; Dholakia, K.; Tarascon, J.-M.; Bruce, P. G., The role of LiO₂ solubility in O₂ reduction in aprotic solvents and its consequences for Li-O₂ batteries. *Nature Chemistry* **2014**, 6 (12), 1091-1099.